# MATERIAL CHARACTERIZATION OF AORTIC TISSUE FOR TRAUMATIC INJURY AND BUCKLING

---

A Dissertation
Submitted to
the Temple University Graduate Board

---

In Partial Fulfillment
of the Requirements for the Degree
DOCTOR OF PHILOSOPHY

---

by
Mobin Rastgar Agah
May 2015

Examining Committee Members:

| | |
|---|---|
| Kurosh Darvish, Adviser | Department of Mechanical Engineering |
| Mohammad Kiani, | Department of Mechanical Engineering |
| Dmitri Vainchtein, | Department of Mechanical Engineering |
| Alexander Rachev, | Bulgarian Institute of Biomechanics |
| Andrew Spence, Reader | Department of Bioengineering |

©
Copyright
2015

by

Mobin Rastgar Agah

All Rights Reserved

# ABSTRACT

While traumatic aortic injury (TAI) and rupture (TAR) continue to be a major cause of morbidity and mortality in motor vehicle accidents, its underlying mechanisms are still not well understood. Different mechanisms such as increase in intraluminal pressure, relative movement of aorta with respect to mediastinal structures, direct impact to bony structures have been proposed as contributing factors to TAI/TAR. At the tissue level, TAI is assumed to be the result of a complex state of supra-physiological, high rate, and multi-axial loading. A major step to gain insight into the mechanisms of TAI is a characterization of the aortic tissue mechanical and failure properties under loading conditions that resemble traumatic events. While the mechanical behavior of arteries in physiological conditions have been investigated by many researchers, this dissertation was motivated by the scarcity of reported data on supra-physiological and high rate loading conditions of aorta.

Material properties of the porcine aortic tissue were characterized and a Fung-type constitutive model was developed based on *ex-vivo* inflation-extension of aortic segments with intraluminal pressures covering a range from physiological to supra-physiological (70 kPa). The convexity of the material constitutive model was preserved to ensure numerical stability. The increase in $\lambda_\theta$ from physiological pressure (13 kPa) to 70 kPa was 13% at the outer wall and 22% at the inner wall while in this pressure range, the longitudinal stretch ratio $\lambda_z$ increased 20%. A significant nonlinearity in the material behavior was observed as in the same pressure range, the circumferential and longitudinal Cauchy stresses at the inner wall were increased 16 and 18 times respectively. The effect of strain-rate on the mechanical behavior and failure properties of the tissue was characterized using uniaxial extension experiments in circumferential and longitudinal directions at nominal strain rates of 0.3, 3, 30 and 400 $s^{-1}$. Two distinct states of failure initiation (FI) and ultimate tensile strength (UTS) were identified at both directions. Explicit direct relationships were derived between FI and UTS stresses and strain rate. On the other hand, FI and UTS strains were rate independent and therefore strain was proposed as the main mechanism of failure. On average, engineering strain at FI was 0.85±0.03 for circumferential direction and 0.58±0.02 for longitudinal direction. The engineering strain at UTS was not different between the two directions and reached 0.89±0.03 on average. Tissue pre-failure linear moduli showed an average of 60% increase over the range of strain rates. Using the developed material model, mechanical stability of aorta was studied by varying the loading parameters for two boundary conditions, namely pinned-pinned boundary condition (PPBC) and clamped-clamped boundary condition (CCBC). The critical pressure for CCBC was three times higher than PPBC. It was shown that the relatively free segment of aorta at the isthmus region may become unstable before reaching the peak intraluminal pressures that occur during a trauma. The mechanical instability mechanism was proposed as a contributing factor to TAI, where elevations in tissue stresses and strains due to buckling may increase the risk of injury.

*to Maryam*

*who taught me the true meaning of friendship*

# ACKNOWLEDGMENTS

I am indebted to my advisor Dr. Kurosh Darvish for his support and guidance throughout my Ph.D. program. His mentorship was beyond my formal education and research training, and I am deeply grateful for that.

I would like to thank my dissertation committee members, Dr. Mohammad Kiani, Dr. Alexander Rachev, Dr. Andrew Spence, and Dr. Dmitri Vainchtein for their comments and advice that improved the quality of this dissertation.

Thanks to the College of Engineering and the Department of Mechanical Engineering for supporting me during my Ph.D. program. Many thanks to my colleagues at Temple Biomechanics Laboratory for all the exciting and constructive moments we had together.

I am thankful to my parents, Ferdows and Ali, whose encouragement was the footstone of my achievement, and to my brother, Mohammad, whose insights has always been the most valuable to me. I am sincerely grateful to my parents in law, Masoumeh, and Mohammad, and to my brother in law, Mohsen, for their never-ending support.

Thanks to Ryan for the joy he brought into my life. My endless love and appreciation to Maryam, whose unconditional support throughout these years made this possible. Nothing can be said to express my deepest admiration of her for the liveliness she bring to our home. I dedicate this dissertation to her.

Mobin Rastgar Agah

April 2015

# TABLE OF CONTENTS

ABSTRACT .......... iii

DEDICATION .......... v

ACKNOWLEDGMENTS .......... vi

LIST OF TABLES .......... x

LIST OF FIGURES .......... xi

1. INTRODUCTION .......... 1

2. MECHANICAL BEHAVIOR OF AORTA IN SUPRA-PHYSIOLOGICAL INTRALUMINAL PRESSURES .......... 5

    Introduction .......... 5

    Materials and Methods .......... 8

        Experimental Setup .......... 8

        Stress-Free Configuration .......... 10

        Deformed Configuration .......... 10

        Homogeneity of deformation .......... 13

        Calculation of Wall Stresses .......... 14

        Optimization of Material Properties .......... 15

    Results .......... 16

    Discussion .......... 24

3. MULTIRATE MECHANICAL BEHAVIOR AND FAILURE PROPERTIES OF AORTIC TISSUE .......... 33

    Introduction .......... 33

Materials and Methods....37
Test Setup....37
Sample Preparation....40
Calculation of Strain and Stress....42
Measures of Material Behavior....44
Statistical Analysis....46
Results....47
Failure Strains....47
Failure Stresses....50
Pre-Failure Linear Modulus....52
Discussion....54
4. MECHANICAL INSTABILITY OF AORTA DUE TO INTRALUMINAL PRESSURE....57
Introduction....57
Methods....61
Case of pinned-pinned boundary condition (PPBC)....62
Case of clamped-clamped boundary condition (CCBC)....63
Stability Analysis....65
Results....68
Discussion....71
5. CONCLUDING REMARKS....76
Suggestions for future research projects....79

BIBLIOGRAPHY ....................................................................................................81

APPENDIX A. DERIVATION OF INFLATION-EXTENSION EQUATIONS .............92

APPENDIX B. DERIVATION OF UNIAXIAL EXTENSION EQUATIONS ...............95

APPENDIX C. UNIAXIAL EXPERIMENTAL DATA ...................................................97

# LIST OF TABLES

Table 1 - Stress-free and load-free parameters of porcine aorta samples .................. 17

Table 2- Parameters of the overall model for porcine aorta, $R^2$ of surface fit is 0.88 and the condition number of the matrix of material parameters is 3. ............................... 21

Table 3–Regression results for failure stress measures versus strain rate in both *C* and *L* directions in the form of $T = a + b \log\varepsilon$ .................................................................. 52

Table 4– Average geometry, material parameters and physiological reference point used in this study for stability analysis. The physiological reference point is based on average *in vivo* values in human aorta. . The initial length represents a segment of descending aorta between the arch and the first intercostal artery. .............................................. 67

# LIST OF FIGURES

Figure 1- Schematic of inflation-extension test setup................................................ 9

Figure 2– Load-free and stress-free configurations: Schematic (top) and images of load-free and stress-free cross sections at the two ends of the samples (bottom)............. 11

Figure 3–Measurement of aortic segment deformation a) two snapshots of a sample at intraluminal pressures of 0 (top) and 70 kPa (bottom). b) Corresponding virtual cylinders obtained from image processing. The positions of the front and back photo targets relative to the fitted cylinder are shown by blue dots and black stars respectively. .. 12

Figure 4– Verification of homogeneity of deformation: Changes in the radial and circumferential positions of the photo targets at three sections (distal, middle, and proximal) of a representative aorta segment from 0 (dashed line) to 70 kPa (solid line) intraluminal pressure. Representative angles of circular sectors at 0 and 70 kPa are denoted by $\alpha 0i$ and $\alpha 70i$ ......................................................................... 14

Figure 5– Summary of experimental stretch ratios at the outer surface: a) Circumferential and b) Longitud inal stretch ratios vs internal pressure, and c) Circumferential vs longitudinal stretch ratio. The mean values and 95% confidence interval is shown for three levels of pressure, namely 13, 40 and 70 kPa. ................................................ 18

Figure 6– Changes of a) radial and b) circumferential stretch ratios across the thickness of aortic wall at three different internal pressures. Longitudinal stretch ratio across the thickness is assumed to be constant. Solid lines and dashed lines represent mean and standard error of the mean respectively .................................................................. 20

Figure 7– Curve fit results for material characterization of a representative sample. Experimental data were simultaneously fitted to Equations 2.5-a (a) and 2.5-b (b). For both curves $R^2$ = 0.999. ............................................................................ 22

Figure 8– Results of inflation-extension simulations based on obtained material properties for P ranging from 0 to 70 kPa. The response of the overall model (solid line) passes through the 95% confidence interval corridor (error bars) and near the average of indi individual samples responses............................................................................ 23

Figure 9– Characterization region and verification paths: The $\lambda z - \lambda \theta$ space for samples used in this study to characterize the constitutive model (shaded gray area). Verification paths based on reported uniaxial extension tests in circumferential and longitudinal directions as well as inflation-extension tests in the physiological range are shown. 25

Figure 10– Prediction of the overall model compared to previously published data on porcine aorta. a) Circumferential stretch vs intraluminal pressure at two different longitudinal stretch ratios for inflation tests in the range of physiological pressures, b) Longitudinal Cauchy stress vs longitudinal stretch ratio for uniaxial extension in the longitudinal direction, and c) Tangent elastic modulus vs stress in uniaxial extension in the circumferential direction. .......................................................................... 26

Figure 11– Distribution of a) radial, b) circumferential and c) longitudinal Cauchy stresses across the aorta wall from overall model at physiological (13 kPa) midrange (40 kPa) and maximum (70 kPa) pressures. .................................................................... 29

Figure 12– The custom-made multirate uniaxial test system. The sample extension is caused by pushing the dynamic crosshead by the passive carriage. More explanation is given in the text. ............................................................................................. 38

Figure 13– Verification of constant extension speed at the time of failure: The Figure shows the side view videos and the measured horizontal speed of the dynamic crosshead from the time of impact until the end of the course. For 10 m/s constant speed was reached before 2 ms. ....................................................................................... 40

Figure 14- Sample Preparation a) Samples were cutout from aortic istmuth. The arrow shows the longitudinal direction and pointing to the proximal side. b) The sample deformation was analyzed by tracking ink dots as photo targets. The scale grid is 5 mm. ................................................................................................................... 41

Figure 15– Representative results of image analysis and strain calculations. The color bar shows the stretch ratio in the direction of extension ($\lambda 1$). The failure initiation (tear in the intimal side) was determined by examining the images. .......................................... 44

Figure 16– A typical stress-strain curve: Three regions and two transition points were observed before failure: a linear toe region, a nonlinear transition region, and a linear pre-failure region. The failure initiation state (FI), based on the first intimal tear in video images, and the ultimate tensile strength (UTS) were defined based on the peak stress, ................................................................................................................... 46

Figure 17– Strain at FI and UTS in $C$ and $L$ directions a) for fours loading rates and b) on average for all rates. The only significant rate dependence was observed in $\varepsilon UTS$ in the longitudinal direction between Rate 2 and Rate 4 (p=0.007). It was concluded that failure strains are not in general rate dependent. The FI state was significantly different in $C$ and $L$ directions and it took more strain in $L$ direction to reach UTS after FI................. 49

Figure 18– Typical failure process observed in $L$ (left) and $C$ (right) directions. Failure in $L$ direction occurred gradually over a wide range of strains. The failure in $C$ direction was abrupt. ........ 50

Figure 19– Change of failure stresses with strain rate. Cauchy stress at a) FI in $C$, b) FI in $L$, c) UTS in $C$, and d) UTS in $L$ direction versus strain rate. The increasing trend of failure stresses with strain rates were found to be significant. Relatively low $R^2$ values showed that the overall variation in stresses could not be explained only by strain rate ........ 51

Figure 20- Rate dependence of modulus $M$ in a) $C$, and b) $L$ directions, Both directions showed an increasing trend with strain rate. The differences were found to be significant when comparing Rate 1 and Rate 2 with Rate 3 and Rate 4 in $C$ direction (p=0.009). The results in $L$ direction were comparable (p=0.4) with Stemper et al. (2007) results... 53

Figure 21– Schematic diagram of aorta before (left) and after (right) mechanical instability. Approximately 100 mm of descending aorta (shaded) is shown with 10 mm deflection at the midsection. ........ 59

Figure 22– a) free body diagram of aortic segment. The aortic wall and intraluminal fluid is considered a composite beam. b) Configuration before and the first mode after loss of stability for pinned-pinned boundary condition. c) Three first mode shapes of clamped-clamped boundary condition used in this study. ........ 64

Figure 23 – Strutt diagram: Change of $\delta$ and $\varepsilon$ with mean blood pressure $P$, pressure amplitude$Pa$, pulsation frequency $f$, initial length $L$ and axial stretch ratio $\lambda$......... 69

Figure 24– Stability region (gray area) for PPBC (left column) and CCBC (right column) plotted with mean pressure as the horizontal axis. The vertical axes are: a & b) pressure amplitude, c & d) blood pulsation frequency, e & f) initial segment length, and g & h) axial stretch ratio. The physiological reference point, as explained in the text, is shown with the red cross. ........ 70

Figure 25 – Change in axial stretch ratio and average axial stress in a 100 mm segment of aorta after deflection. Pinned-pinned and clamped-clamped cases were studied at their corresponding static buckling pressure of 18 and 47 kPa respectively. ........ 74

Figure 26 - Cauchy stress vs stretch ratio in C direction at Rate 1 ........ 99

Figure 27 - Cauchy stress vs stretch ratio in L direction at Rate 1 ........ 99

Figure 28 - Cauchy stress vs stretch ratio in C direction at Rate 2 ........ 100

Figure 29 - Cauchy stress vs stretch ratio in L direction at Rate 2 ........ 100

Figure 30 - Cauchy stress vs stretch ratio in C direction at Rate 3 .......................... 101

Figure 31 - Cauchy stress vs stretch ratio in L direction at Rate 3 .......................... 101

Figure 32 - Cauchy stress vs stretch ratio in C direction at Rate 4 .......................... 102

Figure 33 - Cauchy stress vs stretch ratio in L direction at Rate 4 .......................... 102

# CHAPTER 1

# INTRODUCTION

Traumatic Aortic Rupture (TAR) is one of the leading causes of fatality in motor vehicle accidents. The most recent study on car crash accidents shows that although TAR takes place in a fairly small percentage of the automotive accidents (1.2%), it accounts for more than 20% of the total fatalities. Fatality rate in passengers who experience aortic injury in an accident ranges from 91% to 100% depending on relative side of the impact with more than 85% of the fatalities occurring at the scene. Many of the patient who do not have a full rupture and arrive at a care center, die within the first 24 hours due to injuries and complications in aorta that here are referred to as Traumatic Aortic Injury (TAI) (Lee et al., 2011).

While TAI and TAR continue to be major causes of morbidity and mortality in motor vehicle accidents, their underlying mechanisms are still not well understood. It has been nevertheless agreed upon that a single factor cannot lead to TAI or TAR and a combination of different factors generates stresses and strains in the tissue that exceed the injury and failure levels. These factors include direct impact to the chest, relative movement of aorta with respect to mediastinal structures, and blood pressure increase in aorta during an accident among others (Neschis, Scalea, Flinn, & Griffith, 2008).

A major step to gain an insight into the mechanisms of TAI and TAR is to understand the mechanical behavior of aortic tissue under loading conditions that lead to the injury and failure. Although the mechanical properties of blood vessels under physiological conditions have been investigated and modeled by many researchers, due to material nonlinearity and rate dependence, these models cannot be applied to supra-physiological pressures and high rate deformations that occur in automotive crashes.

It has been shown recently that a pressure increase in aorta would not only increase the strains and stresses in the tissue due to inflation, but also will cause the artery to deviate from its original configuration into a buckled form at the arch and proximal descending aorta (Han, 2009b; Rachev, 2009). This type of mechanical instability would ultimately increase the level of strains and stresses in the tissue and can be a contributing factor in the mechanisms of TAI and TAR, and one that has not been investigated before.

The objective of this dissertation was to advance our understanding of the mechanisms of TAI/TAR. This was accomplished by characterizing the mechanical behavior and failure properties of the aortic tissue under the supra-physiological intraluminal pressures and multirate deformations that may cause TAI/TAR. Additionally, the mechanical instability of aorta as a contributing factor in increasing tissue strains and stresses was investigated. The content of the manuscript is structured as follows:

**Chapter 2: Mechanical behavior of aorta in supra-physiological intraluminal pressures.** This chapter reports the mechanical behavior of the porcine aortic tissue under intraluminal pressures up to 5 times higher than the physiological range. A custom-made inflation-extension test setup used in this study and the testing procedure is explained. Mechanical behavior of the tissue is reported through experimental stress-strain curves and a Fung-type constitutive model. The material model was verified against previously published data on porcine aorta.

**Chapter 3: Multirate mechanical behavior and failure properties of aortic tissue.** The results of multirate uniaxial tests on strips of porcine aorta are reported in this chapter. First, a multirate uniaxial test system that was designed and made specifically for this study is described. Small coupon samples were cut in both circumferential and longitudinal directions near the aortic arch. Failure initiation stresses, ultimate tensile strengths and their corresponding strains are identified and compared at different strain rates. Additionally, the rate dependence of the pre-failure linear moduli is explained. The range of strain rates in this study is significantly increased compared to previous studies.

**Chapter 4: Mechanical instability of aorta due to intraluminal pressure.** In this chapter, the results of numerical studies on the mechanical instability of aorta are reported. The analytical procedure is explained and the effects of boundary conditions, as well as geometry and loading parameters, are investigated. The increase in tissue stresses and strains due to buckling are estimated and discussed as contributing factors in the mechanism of TAI/TAR.

**Chapter 5** summarizes the results and proposes some directions for future research projects

**Appendix A** presents the mathematical formulations of the inflation-extension experiments. The theory of deriving the uniaxial response from a three-dimensional hyperelastic constitutive model is presented in **Appendix B**. **Appendix C** includes all experimental data from uniaxial experiments.

Chapters 2, 3, and 4 are written in the form of stand-alone journal papers. Chapters 2 and 4 have been already submitted and the other chapter will soon be submitted. The results discussed here have been presented at several national conferences in the past few years.

# CHAPTER 2

# MECHANICAL BEHAVIOR OF AORTA IN SUPRA-PHYSIOLOGICAL INTRALUMINAL PRESSURES

## Introduction

There is an increasing need for characterizing the mechanical behavior of arteries in supra-physiological pressures (Holzapfel & Gasser, 2007; Sommer, Regitnig, Költringer, & Holzapfel, 2010) due to its application in different scenarios such as chest trauma (Bass et al., 2001; Hardy et al., 2008), balloon angioplasty (Castaneda-zunlga et al., 1980; Holzapfel, Stadler, & Schulze-Bauer, 2002), and endovascular stenting (Holzapfel, Stadler, & Gasser, 2005; Rogers, Tseng, Squire, & Edelman, 1999). Accurate description of arteries' mechanical behavior is a crucial step in developing computational models that are used to predict their deformation in complex loading conditions. Conducting multi-axial experiments on arteries is not trivial. An example where experimental models are not conclusive is traumatic injury of aorta, which is a leading cause of accidental fatalities (Bass et al., 2001; Hardy et al., 2008; Pearson et al., 2008). In this case, more accurate constitutive models of aorta are necessary for determining the mechanisms of tissue deformations and injury.

Several experimental methods have been reported in the literature for characterizing the mechanical behavior of aorta. Indentation tests were used to describe the local tissue behavior and quantify its heterogeneity (Hemmasizadeh, Darvish, & Autieri, 2012b; Matsumoto, Goto, Furukawa, & Sato, 2004). However, these studies were limited to small deformations and their results, due to material nonlinearity, are not suitable for modeling tissue response under large deformations. Uniaxial tension and planar biaxial tests on excised tissue have been used extensively to characterize the mechanical properties of aortic wall in large deformations (Bass et al., 2001; Gundiah et al., 2008; Mohan & Melvin, 1982; Prendergast et al., 2003; Sokolis, 2007; Stemper, Yoganandan, & Pintar, 2007). Mechanical properties of human aorta from uniaxial experiments showed a significant anisotropy and dependence on loading rate and age (Mohan & Melvin, 1982). Similar tests were carried out on porcine aorta in which the failure initiation in the longitudinal direction, i.e., the first visible tear, and the corresponding stresses and strains were determined (Stemper et al., 2007). In experiments on excised tissue, the cylindrical microstructure of the aortic wall is altered, and the stress in the radial direction is assumed to be zero (two-dimensional models). Similarly, in membrane inflation experiments, tissue is considered as a thin layer and the distribution of stress within the thickness is ignored (Marra, Kennedy, Kinkaid, & Fillinger, 2006; Mohan & Melvin, 1983; Pearson et al., 2008). Therefore, such results cannot be used to investigate the stress distribution within the aortic wall which is essential for predicting the location of initiation of failure and its propagation across the wall thickness (Azizzadeh et al., 2011; Stemper et al., 2007).

In inflation-extension tests, the anatomical microstructure (e.g. elastic lamellae) and residual stresses of aorta are preserved and intraluminal pressure causes tissue deformation similar to *in vivo* conditions (Humphrey, Kang, Sakarda, & Anjanappa, 1993). Previously published studies on inflation-extension experiments on human and porcine aorta were focused on the tissue behavior in the physiological range (Kim & Baek, 2011; Labrosse, Beller, Mesana, & Veinot, 2009; Labrosse, Gerson, Veinot, & Beller, 2013; M A Lillie, Armstrong, Gérard, Shadwick, & Gosline, 2012; M.A. Lillie, Shadwick, & Gosline, 2010). Both fixed-fixed (Kim & Baek, 2011; M A Lillie et al., 2012; M.A. Lillie et al., 2010) and fixed-free (Labrosse et al., 2009, 2013) boundary conditions at the two ends of the specimen have been utilized previously. In this study, the fixed-free boundary condition was implemented in order to avoid buckling of the segment (Han, 2007; M Rastgar Agah, Laksari, Darvish, & Rachev, 2012) in supra-physiological pressures. This boundary condition was verified previously by Labrosse *et al.* (Labrosse et al., 2009, 2013) in the physiological range. They validated the experimental method against simulated data from previously published material models based on the fixed-fixed boundary condition and concluded that the identified material parameters from the two methods were the same.

Several investigators have reported constitutive modeling of arteries from inflation-extension experiments (Y. C. Fung, Fronek, & Patitucci, 1979; García et al., 2011; Labrosse et al., 2009, 2013; Schulze-Bauer, Mörth, & Holzapfel, 2003; Vorp, Rajagopal, Smolinski, & Borovetz, 1995). However, to the best of our knowledge, this study is the first to characterize the mechanical behavior of aorta in physiological and supra-physiological loading conditions using inflation-extension tests.

# Materials and Methods

## Experimental Setup

Six porcine descending thoracic aortas were acquired from a local slaughterhouse and transported in ice-cold Phosphate Buffered Saline (PBS) to the laboratory and stored at $4^{o}$C before experiments. Porcine aorta has been widely studied in the literature and it has been shown that it is similar to young and healthy human aorta in terms of mechanical behavior and geometry (Bass et al., 2001; García et al., 2011; Pearson et al., 2008). All tests were conducted within 16 hours post-mortem. Adipose and connective tissues were removed, and approximately 200 mm length straight samples were excised between the arch and the 6th intercostal arteries. Two 3-mm-thick rings from the two ends of the samples were cut with a scalpel for measuring the stress-free geometry and the opening angle. Two miniature fiber optic pressure sensors (FOP-MIV-R1, FISO, Quebec, Canada) were inserted into two intercostal arteries close to the middle of the sample, and all branches were ligated at the base using surgical sutures. A 6×6 array of black beads, as photo targets, with the resolution of approximately 12 mm × $50^{o}$ in longitudinal and circumferential directions was attached to the external surface using a minimal amount of cyanoacrylate glue. The distal end was blocked by a slider that could move freely in a low-friction self-aligning linear bearing and allowed free axial movement. The proximal end was attached to a fixed brass pipe fitting through which the sample was pressurized with PBS at room temperature. The gauge pressure of the fluid, just before entering the sample, was measured by an analog pressure sensor (PX303, Omega Engineering, Stamford, CT), and inside the sample, with the fiber optic sensors. The absence of leakage in the specimen was verified by assuring that the three pressure measurements were equal. The sample with the attached supports and transducers was encased in a clear container that was filled with PBS (Figure 1). Fluid pressurization was accomplished using a diaphragm accumulator (30573, Jabsco, Basingtoke, UK) which was controlled by a proportional pressure regulator (550X, Control Air, Amherst, NH) connected to a 6 bar air supply. Samples were preconditioned by applying five pressurization cycles at 1 Hz in the physiological range (0-20 kPa). The intraluminal pressure was then increased from 0 to 70 kPa (525 mmHg) at a rate of 1 kPa/s, and the data were recorded. Sample deformation was measured by tracking the three-dimensional motion of the photo targets captured by two cameras (FASTCAM SA3, Photron, San Diego, CA) that acquired two direct images and two reflection images from a front-facing mirror at 60 frames per second.

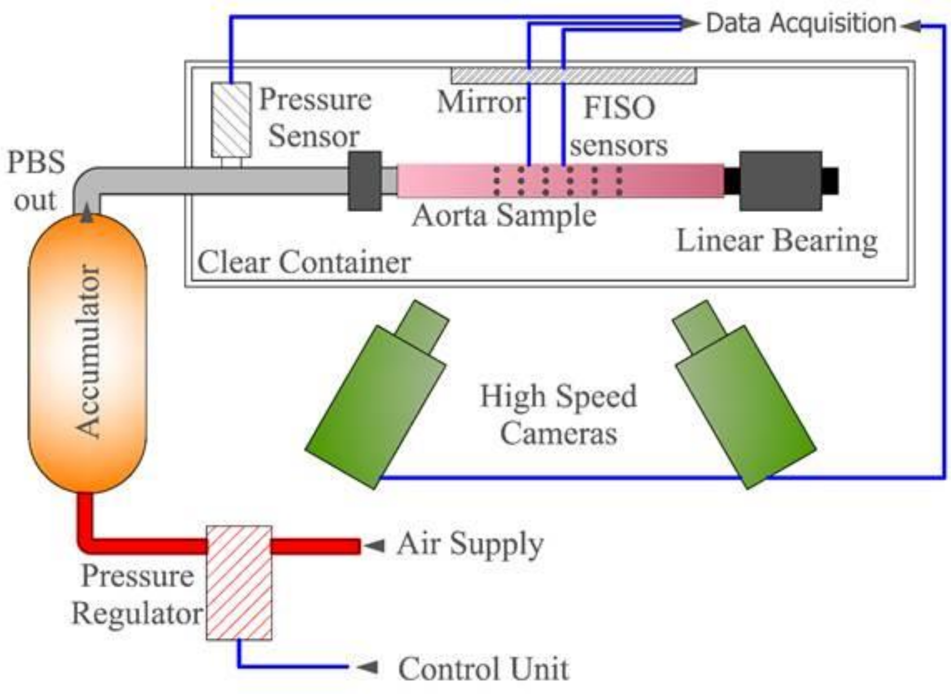
Data Acquisition
Pressure Sensor
Mirror
FISO sensors
PBS out
Aorta Sample
Linear Bearing
Clear Container
Accumulator
High Speed Cameras
Air Supply
Pressure Regulator
Control Unit

Figure 1- Schematic of inflation-extension test setup.

## Stress-Free Configuration

The two rings obtained from proximal and distal ends of each sample were cut in the axial direction while floated in PBS and allowed to reach the stress-free geometry in about 20 minutes (Rachev & Greenwald, 2003). The closed and open rings were photographed, and the outer and inner perimeters in stress-free and load-free configurations were measured using MATLAB image processing toolbox. The stress-free parameters (outer radius $R_o$, thickness $D$, and opening angle $\Theta_0$), and load-free parameters (outer radius $r_o$ and thickness $d$), as shown in Figure 2, were calculated following the method explained in (Chuong & Fung, 1986).

## Deformed Configuration

The three-dimensional motion of the photo targets was calculated using an open-source MATLAB code (Hedrick, 2008). Approximately 35 mm segments in the middle of the samples were used for further analysis (Figure 3-a). It was assumed that this segment length was small enough that would undergo a homogenous deformation. Segments consisted of three transverse sections of photo targets, namely proximal, middle, and distal sections. A cylinder was fit to the photo targets of the three sections (Figure 3-b). It was assumed that the principal axes of the cylinder were aligned with the material principal axes (Holzapfel & Ogden, 2010, 2008). This assumption was verified by observing no twist about the longitudinal axis during inflation.

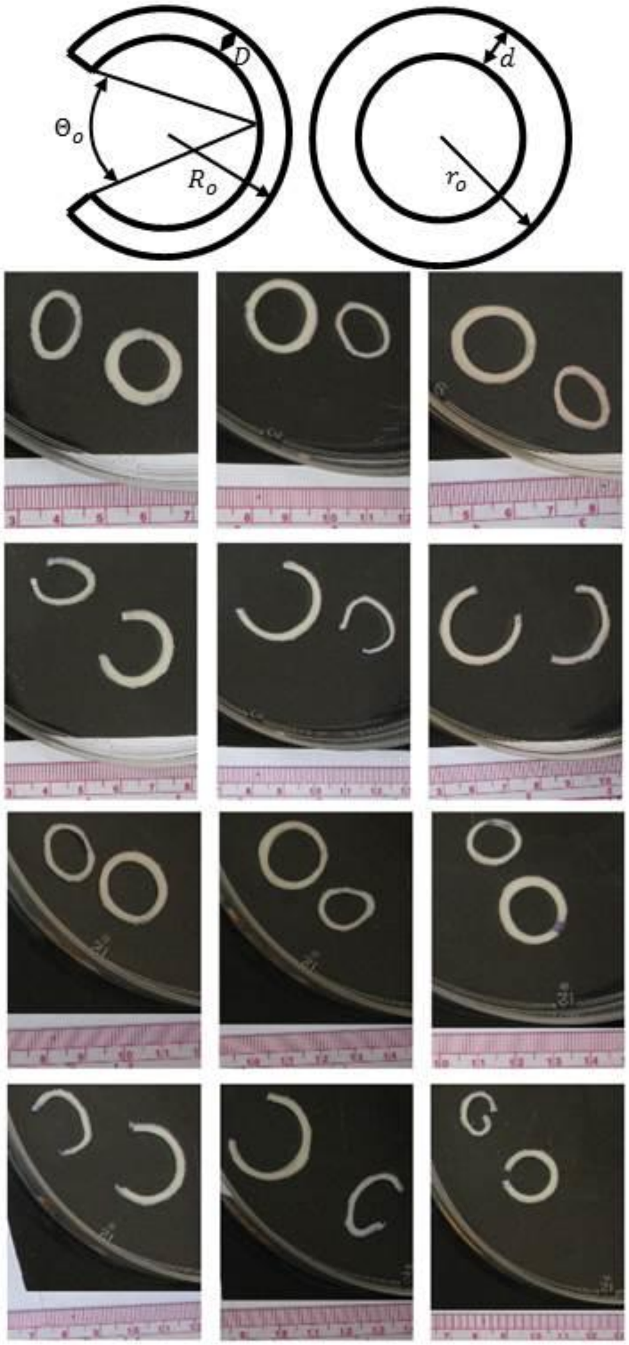

Figure 2– Load-free and stress-free configurations: Schematic (top) and images of load-free and stress-free cross sections at the two ends of the samples (bottom)

The principal stretch ratios in the circumferential and longitudinal directions ($\lambda_\theta$, $\lambda_z$) were determined by mapping the stress-free configuration ($R, \Theta,$ and $Z$) to the current configuration ($r, \theta,$ and $z$) (Holzapfel, Gasser, & Ogden, 2000) :

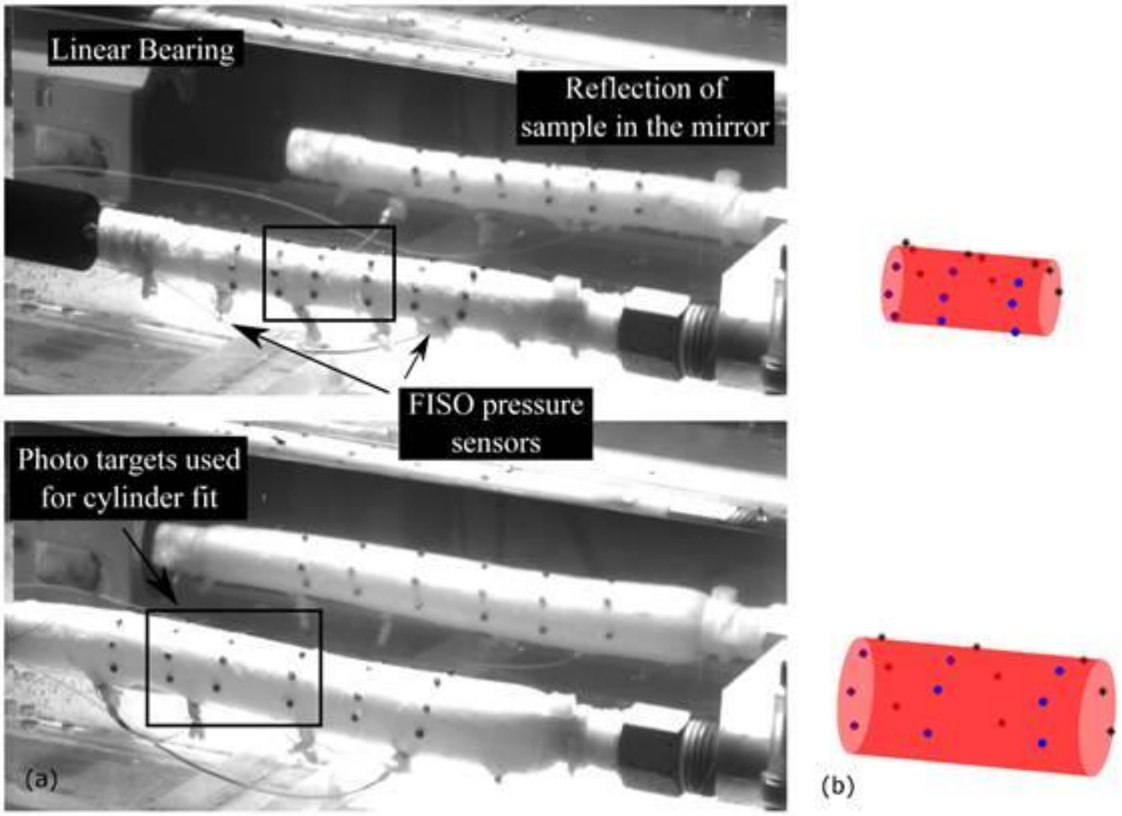
Linear Bearing
Reflection of sample in the mirror
FISO pressure sensors
Photo targets used for cylinder fit
(a)
(b)

Figure 3–Measurement of aortic segment deformation a) two snapshots of a sample at intraluminal pressures of 0 (top) and 70 kPa (bottom). b) Corresponding virtual cylinders obtained from image processing. The positions of the front and back photo targets relative to the fitted cylinder are shown by blue dots and black stars respectively.

$$\lambda_\theta = \frac{\pi}{(\pi - \Theta_0)} \frac{r}{R}, \qquad \lambda_z = \frac{z}{Z} \tag{2.1-a}$$

in which $z(p = 0) = Z$ was considered as the stress-free length. The radial stretch ratio ($\lambda_r$) was determined based on the incompressibility assumption:

$$\lambda_r = \frac{\partial r}{\partial R} = \frac{1}{\lambda_\theta \lambda_z} \tag{2.1-b}$$

Based on the measured outer radius $r_o$ and length z, the radial coordinate $r$ for a reference radius $R$ was obtained by integrating Equation (2.1-b):

$$r = \sqrt{r_o^2 - \frac{1}{\lambda_z}\frac{(\pi - \Theta_0)}{\pi}(R_o^2 - R^2)} \tag{2.2}$$

The nonzero components of the Lagrangian strain tensor in $r, \theta,$ and $z$ directions were calculated as $E_r = \frac{1}{2}({\lambda_r}^2 - 1)$, $E_\theta = \frac{1}{2}({\lambda_\theta}^2 - 1)$ and $E_z = \frac{1}{2}({\lambda_z}^2 - 1)$.

## Homogeneity of deformation

Homogeneity of the deformation of segments in $\theta$ and $z$ directions was verified by comparing the positions of the photo targets at 0 and 70 kPa pressures (Figure 4) in the following three steps: a) At each section, the angles of 5 circular sectors at the two pressures ($\alpha_0^i$ and $\alpha_{70}^i$) were compared using linear regression analysis to determine whether they were equal, i.e., $\lambda_\theta$ stayed uniform in the $\theta$ direction, b) $\lambda_\theta$ at the proximal, middle, and distal sections were compared using ANOVA to determine whether $\lambda_\theta$ was uniform in the $z$ direction, and c) $\lambda_z$ at the proximal and distal halves were compared using student's t-test to verify its uniformity in the $z$ direction.

### Calculation of Wall Stresses

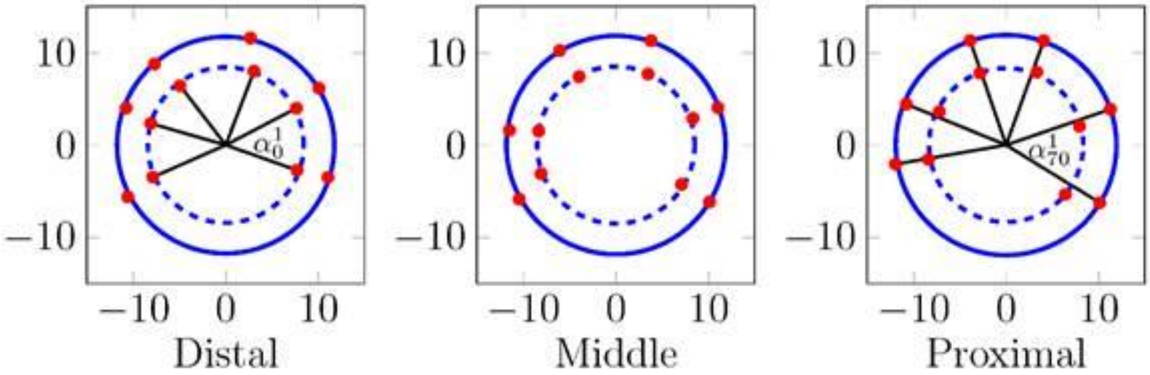

Figure 4– Verification of homogeneity of deformation: Changes in the radial and circumferential positions of the photo targets at three sections (distal, middle, and proximal) of a representative aorta segment from 0 (dashed line) to 70 kPa (solid line) intraluminal pressure. Representative angles of circular sectors at 0 and 70 kPa are denoted by $\alpha_0^i$ and $\alpha_{70}^i$

In order to calculate the stress tensor, an incompressible Fung-type strain energy density function (SEDF) (Y. C. Fung et al., 1979) was considered in the following form:

$$W = \frac{1}{2}c[\exp(\boldsymbol{E}^T\boldsymbol{C}\boldsymbol{E}) - 1] - H(J - 1) \tag{2.3-a}$$

in which

$$\boldsymbol{E} = \begin{bmatrix} E_r \\ E_\theta \\ E_z \end{bmatrix}, \qquad \boldsymbol{C} = \begin{bmatrix} c_1 & c_4 & c_5 \\ c_4 & c_2 & c_6 \\ c_5 & c_6 & c_3 \end{bmatrix} \tag{2.3-b}$$

Here, $\boldsymbol{E}$ is the vector of normal Lagrangian strain components, $\boldsymbol{C}$ is the matrix of material parameters $c_1$ to $c_6$ which together with the scaling factor $c$ should be determined based on experimental data. $J$ is the change in volume and $H$ is a Lagrange multiplier that is determined from the boundary conditions.

The nonzero (principal) components of the Cauchy stress tensor were determined from equilibrium equations (Chuong & Fung, 1983):

$$T_r = \int_{r_i}^{r} \left( {\lambda_\theta}^2 \frac{\partial W}{\partial E_\theta} - {\lambda_r}^2 \frac{\partial W}{\partial E_r} \right) \frac{dr}{r} - p \tag{2.4-a}$$

$$T_\theta = T_r + {\lambda_\theta}^2 \frac{\partial W}{\partial \theta} - {\lambda_r}^2 \frac{\partial W}{\partial r} \tag{2.4-b}$$

$$T_z = T_r + {\lambda_z}^2 \frac{\partial W}{\partial z} - {\lambda_r}^2 \frac{\partial W}{\partial r} \tag{2.4-c}$$

Two independent equations were used for material parameter identification. The first equation was derived from applying the boundary condition in the $r$ direction ($T_r(r = ro) = 0$) to Equation (2.4-a):

$$p = \int_{r_i}^{r_o} \left( {\lambda_\theta}^2 \frac{\partial W}{\partial E_\theta} - {\lambda_r}^2 \frac{\partial W}{\partial E_r} \right) \frac{dr}{r} \tag{2.5-a}$$

The second equation was the equilibrium in the $z$ direction:

$$F_z = p\, A_{lum} = 2\pi \int_{r_i}^{r_o} T_z\, r\, dr \tag{2.5-b}$$

in which $F_z$ is the axial force and $\mathrm{A_{lum}}$ is the current lumen cross-sectional area. Details of the derivations of the equations given in this section are provided in Appendix A.

### Optimization of Material Properties

Based on the experimentally measured pressure $p$ and stretch ratios at the outer wall $\lambda_\theta(r_o)$ and $\lambda_z$, the material parameters given in Equations (2.3-a) and (2.3-b) were determined by optimizing equations (2.5-a) and (2.5-b) using MATLAB *lsqcurvefit* function. To ensure the convexity of $W$, matrix $\boldsymbol{C}$ should be positive definite (Federico, Grillo, Giaquinta, & Herzog, 2007). To obtain a positive definite $\boldsymbol{C}$ without additional constraints in the optimization, the Cholesky factorization was used to replace the 6 components of $\boldsymbol{C}$ with 6 components of the corresponding lower triangular matrix $\boldsymbol{L}$ as given below (Trefethen & David B, 1997)

$$\boldsymbol{C} = \begin{bmatrix} c_1 & c_4 & c_5 \\ c_4 & c_2 & c_6 \\ c_5 & c_6 & c_3 \end{bmatrix} = \boldsymbol{L}\,\boldsymbol{L}^T = \begin{bmatrix} l_1^2 & l_1 l_4 & l_1 l_5 \\ l_1 l_4 & l_2^2 + l_4^2 & l_2 l_6 + l_4 l_5 \\ l_1 l_5 & l_2 l_6 + l_4 l_5 & l_3^2 + l_5^2 + l_6^2 \end{bmatrix} \tag{2.6}$$

After determining the material parameters for each sample, the material parameters of an overall SEDF were obtained by fitting a surface for $W$ in $\lambda_z - \lambda_\theta$ domain ($\lambda_z \geq 1$, $\lambda_\theta \geq 1$) to 6 surfaces obtained for the samples using MATLAB surface fitting *sftool*.

## Results

Stress-free and load-free geometries of the samples are listed in Table 1. These values were used in equations (2.1-a) and (2.1-b) to calculate the stretch ratios. Variation of $\lambda_\theta(r_o)$ and $\lambda_z$ versus pressure are given in Figure 5-a and Figure 5-b. After about 20 kPa the slope of the stretch ratio versus pressure curves dramatically changed. Stretch ratios at the outer radius reached $\lambda_\theta(r_o) = 1.43 \pm 0.02$ and $\lambda_z = 1.46 \pm 0.06$ (mean ± 95% margin of error) at 70 kPa which were 13% and 20% higher than their values at physiological pressure of 13 kPa. ($\lambda_\theta(r_o) = 1.26 \pm 0.05$ and $\lambda_z = 1.22 \pm 0.03$).

Table 1 - Stress-free and load-free parameters of porcine aorta samples

| | Sample 1 | Sample 2 | Sample 3 | Sample 4 | Sample 5 | Sample 6 | average ± 95% margin of error |
|---|---|---|---|---|---|---|---|
| $\boldsymbol{R_o(mm)}$ | 9.71 | 12.77 | 11.60 | 12.47 | 11.81 | 8.68 | 11.17 ± 1.70 |
| $\boldsymbol{D(mm)}$ | 2.46 | 2.22 | 2.48 | 2.44 | 2.70 | 2.34 | 2.44 ± 0.17 |
| $\boldsymbol{\Theta_0(deg)}$ | 28.8 | 62.4 | 42.2 | 60.2 | 39.8 | 11.5 | 40.8 ± 20.2 |
| $\boldsymbol{r_o(mm)}$ | 8.64 | 8.84 | 9.79 | 10.09 | 10.09 | 8.28 | 9.29 ± 0.84 |
| $\boldsymbol{d(mm)}$ | 2.34 | 2.18 | 2.26 | 2.01 | 2.48 | 2.31 | 2.26 ± 0.17 |

Figure 5-c shows that $\lambda_\theta(r_o)$ was slightly smaller than $\lambda_z$ with fixed-free boundary condition ($\lambda_\theta(r_o) = 0.76\lambda_z + 0.32, R^2 = 0.86$). For an isotropic thin wall pressure vessel, the slope of the $\lambda_\theta$ vs $\lambda_z$ curve is 2. The observed difference in the slope is an indication of orthotropic material behavior and that the tissue was stiffer in the $\theta$ direction.

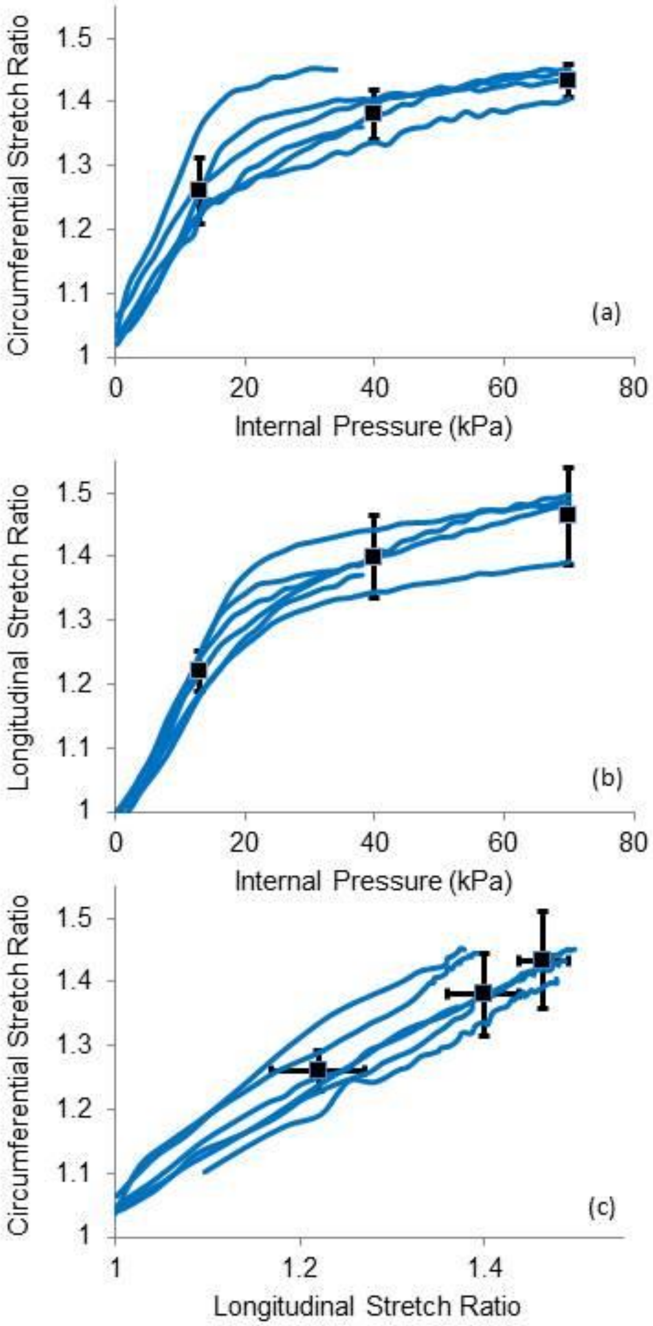

Figure 5– Summary of experimental stretch ratios at the outer surface: a) Circumferential and b) Longitud inal stretch ratios vs internal pressure, and c) Circumferential vs longitudinal stretch ratio. The mean values and 95% confidence interval is shown for three levels of pressure, namely 13, 40 and 70 kPa.

Three levels of applied pressure, namely the physiological (13 kPa), the maximum (70 kPa), and a mid-range pressure (40 kPa) were chosen to compare the distributions of calculated $\lambda_\theta$ and $\lambda_r$ across the aortic wall as shown in Figure 6-a and 2.6-b. The wall thickness was normalized with 0 and 1 corresponding to $r_i$ and $r_o$ respectively. The spatial variability (gradient) of $\lambda_\theta$increased significantly at higher pressures. The difference of 10% between the values at $r_i$ and $r_0$ at 13 kPa was raised to 19% and 21% at 40 and 70 kPa respectively. The maximum $\lambda_\theta(r_i)$ reached $1.71 \pm 0.15$ that was 23% higher than the corresponding value at 13 kPa. Since $\lambda_z$ was assumed to be constant at each pressure level, the increase in $\lambda_\theta$ was accompanied by a decrease in $\lambda_r$.

The three steps used to verify the homogeneity of the deformation of segments confirmed this assumption. Linear regression between the angles of circular sectors at 0 and 70 kPa showed that they were almost equal ($\alpha_{70}^{i} = 0.99\alpha_0^i$, $R^2 = 0.984$, $p < 0.001$). Change of $\lambda_\theta(r_o)$ from 0 to 70 kPa at the proximal, middle, and distal sections were $1.39 \pm 0.05$, $1.36 \pm 0.05$ and $1.34 \pm 0.06$ respectively and were not statistically different ($p = 0.12$). $\lambda_z$ at the proximal and distal halves were $1.46 \pm 0.10$ and $1.45 \pm 0.08$ respectively and their difference was not statistically significant ($p = 0.81$).

A representative result of material characterization is given in Figure 7. Measured $\lambda_\theta(r_o)$ and $\lambda_z$ at about 30 pressure levels between 0 and 70 kPa were used to simultaneously fit the corresponding values of $p$ and $F_z$ based on Equations (2.5-a) and (2.5-b). The goodness of fit for each sample, measured by $R^2$ for both $p$ and $F_z$, was higher than 0.98. The material parameters of the overall SEDF with 95% confidence interval are given in Table 2. It should be noted that the parameters of the model were statistically significant (nonzero) and showed statistically significant anisotropy ($c_2 > c_3 > c_1$ and $c_6 > c_4 > c_5$).

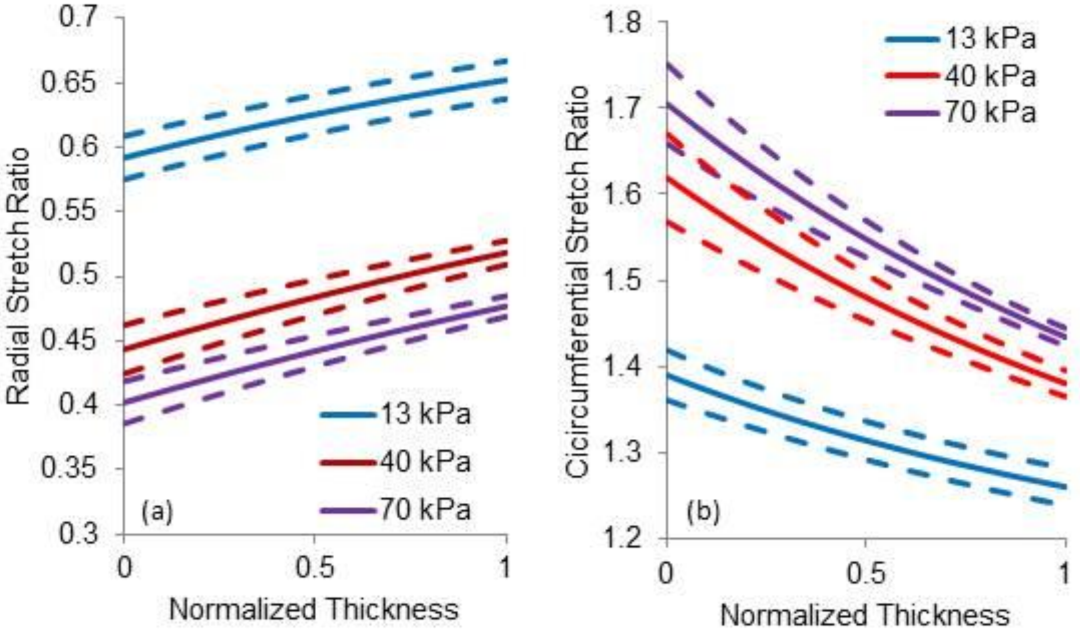

Figure 6– Changes of a) radial and b) circumferential stretch ratios across the thickness of aortic wall at three different internal pressures. Longitudinal stretch ratio across the thickness is assumed to be constant. Solid lines and dashed lines represent mean and standard error of the mean respectively

Calculated Cauchy stresses at the outer wall $T_\theta(r_o)$ and $T_z(r_o)$ versus corresponding stretch ratios $\lambda_\theta(r_o)$ and $\lambda_z$ are shown in Figure 8-a and b which demonstrate the extent of inter-specimen variability. This figure also shows that the response of the overall model is approximately the same as the average response of all samples.

Table 2- Parameters of the overall model for porcine aorta, $R^2$ of surface fit is 0.88 and the condition number of the matrix of material parameters is 3.

| Model parameters | Overall | 95% confidence interval |
|---|---|---|
| c (kPa) | 61.35 | 56.08-66.63 |
| $c_1$ | 0.6218 | 0.4243-0.8193 |
| $c_2$ | 1.5557 | 1.5277-1.5836 |
| $c_3$ | 1.0222 | 0.9812-1.0631 |
| $c_4$ | 0.2103 | 0.0467-0.3740 |
| $c_5$ | 0.1207 | 0.0202-0.2213 |
| $c_6$ | 0.2971 | 0.2413-0.3529 |

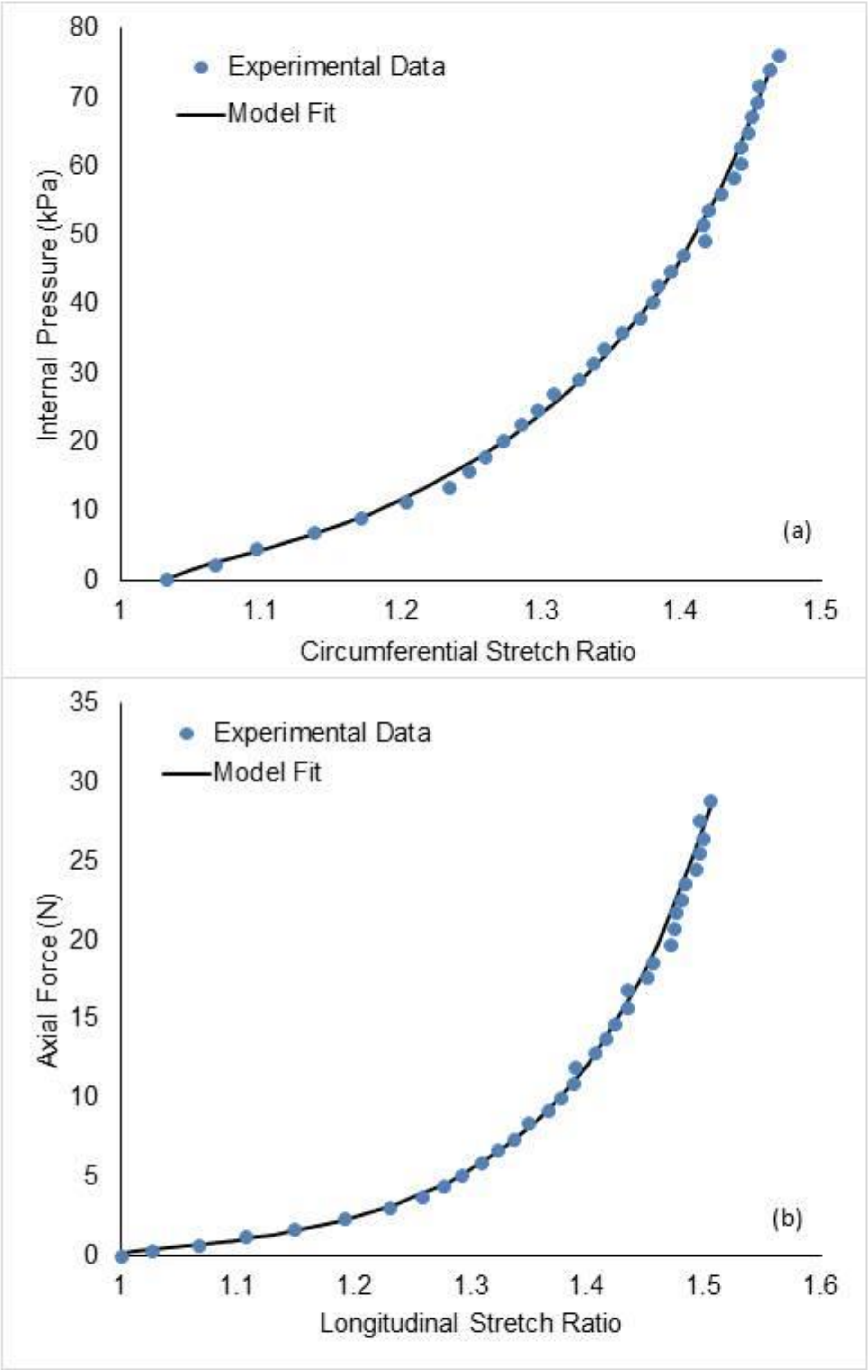

Figure 7– Curve fit results for material characterization of a representative sample. Experimental data were simultaneously fitted to Equations 2.5-a (a) and 2.5-b (b). For both curves $R^2 = 0.999$.

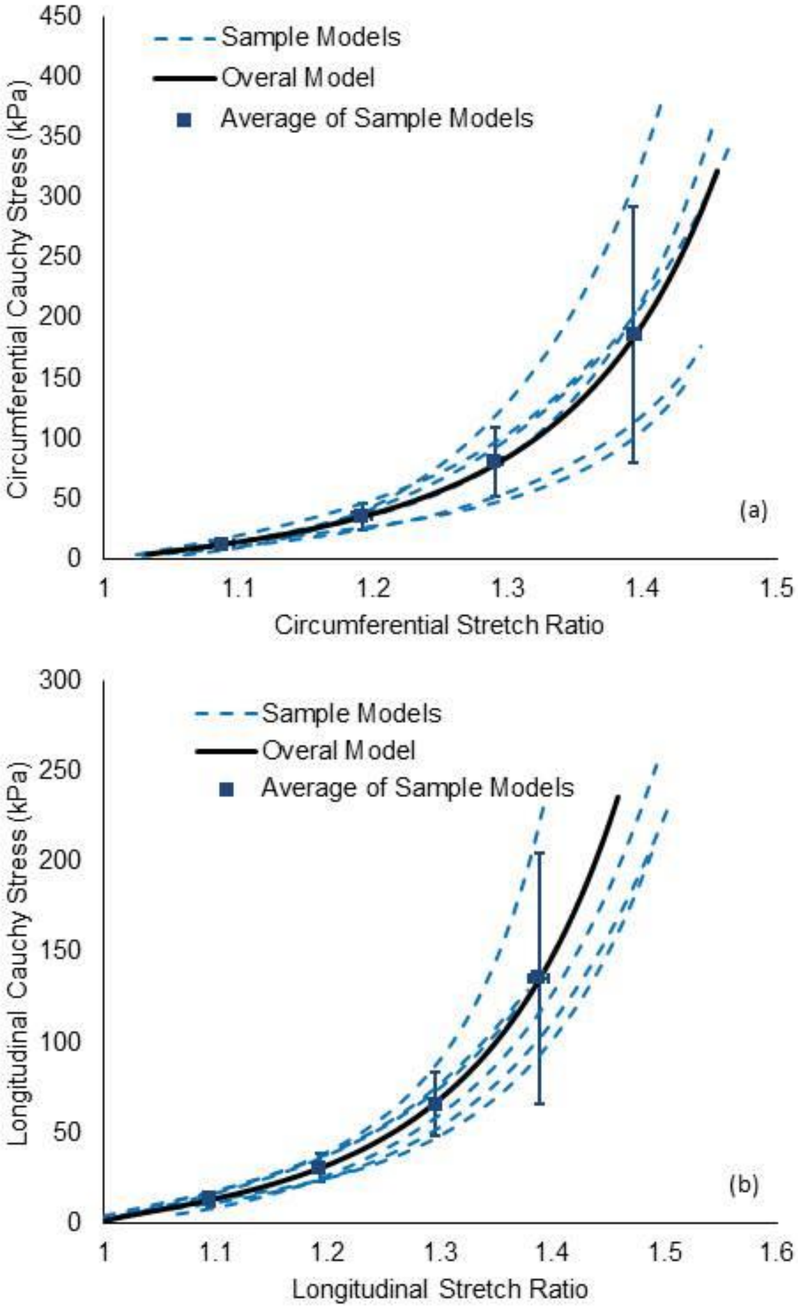

Figure 8– Results of inflation-extension simulations based on obtained material properties for P ranging from 0 to 70 kPa. The response of the overall model (solid line) passes through the 95% confidence interval corridor (error bars) and near the average of indi individual samples responses.

## Discussion

The material properties of aorta in supra-physiological loading have been characterized previously using excised tissues in uniaxial (Mohan & Melvin, 1982; Prendergast et al., 2003; Sokolis, 2007; Stemper et al., 2007) and biaxial (Bass et al., 2001; Gundiah et al., 2008; Prendergast et al., 2003) test protocols. This study, to the best of our knowledge, is the first that these properties were characterized using cylindrical segments in inflation-extension tests. This method maintained the tissue natural microstructural arrangement and the loading was applied superimposed on the circumferential residual stress. As a result, it was believed that this test protocol was a better representation of *in vivo* loadings that result in large tissue deformations. To the contrary of most inflation-extension tests that were reported in the literature (Y. C. Fung et al., 1979; Humphrey et al., 1993; Kim & Baek, 2011; M A Lillie et al., 2012; M.A. Lillie et al., 2010; Schulze-Bauer et al., 2003), one end of the specimen was kept free to extend to avoid buckling under high pressures (Han, 2007; M Rastgar Agah et al., 2012). While this boundary condition limited the $\lambda_z - \lambda_\theta$ space in which the material parameters were characterized, it was verified that the obtained SEDF could predict the behavior of porcine aorta in other loading paths that were available in the literature (M A Lillie et al., 2012; Prendergast et al., 2003; Sokolis, 2007). These loading paths are referred to as the "verification paths". Figure 9 shows the characterization space (shaded) that was used in this study together with the four verification paths.

The $\lambda_\theta$ versus pressure data, reported in (M A Lillie et al., 2012) for inflation-extension of intact specimens, was used as one of the verification paths. This data is limited to 20 kPa as the focus of the study was the tissue behavior under physiological pressures.

$\lambda_z$ was kept constant and the results for $\lambda_z = 1.24$ at the proximal region and $\lambda_z = 1.37$ at the distal region were reported. The segments analyzed in the present study were between 50 to 60 mm below the 1st intercostal arteries and were therefore closer to the distal segments in (M A Lillie et al., 2012). Comparison between $\lambda_\theta$, calculated based on the material properties reported in Table 2, and the experimental results of (M A Lillie et al., 2012) (Figure 10-a) showed good agreement particularly for the distal data ($R^2 = 0.70$ and 0.94 for proximal and distal data respectively).

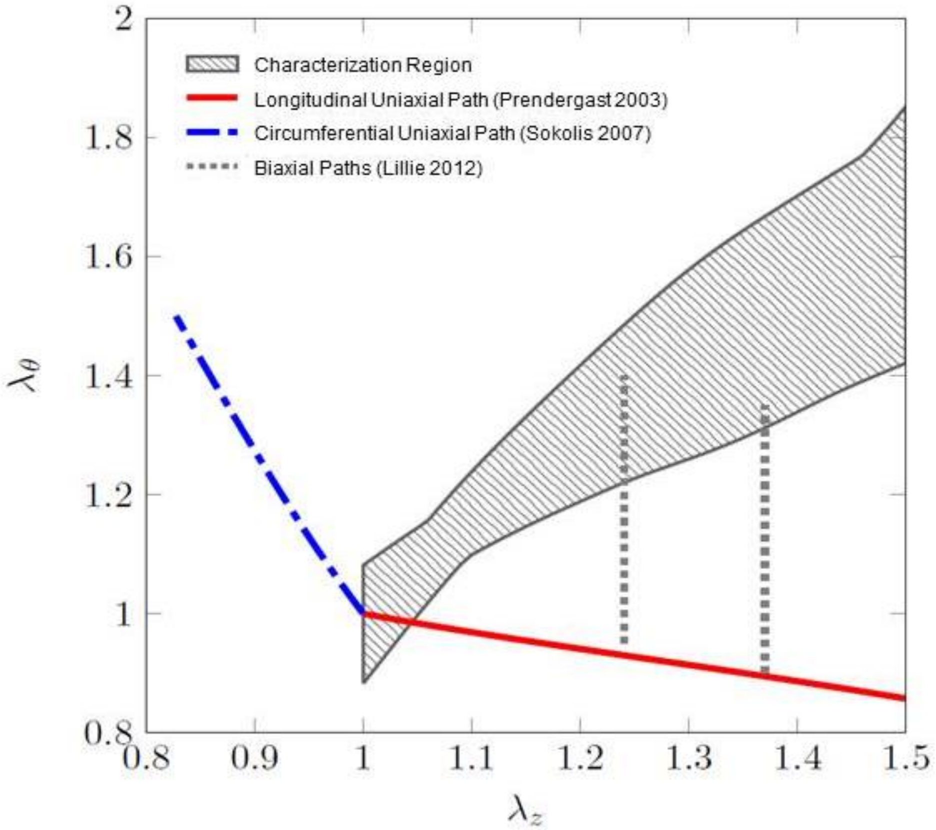

Figure 9– Characterization region and verification paths: The $\lambda_z - \lambda_\theta$ space for samples used in this study to characterize the constitutive model (shaded gray area). Verification paths based on reported uniaxial extension tests in circumferential and longitudinal directions as well as inflation-extension tests in the physiological range are shown.

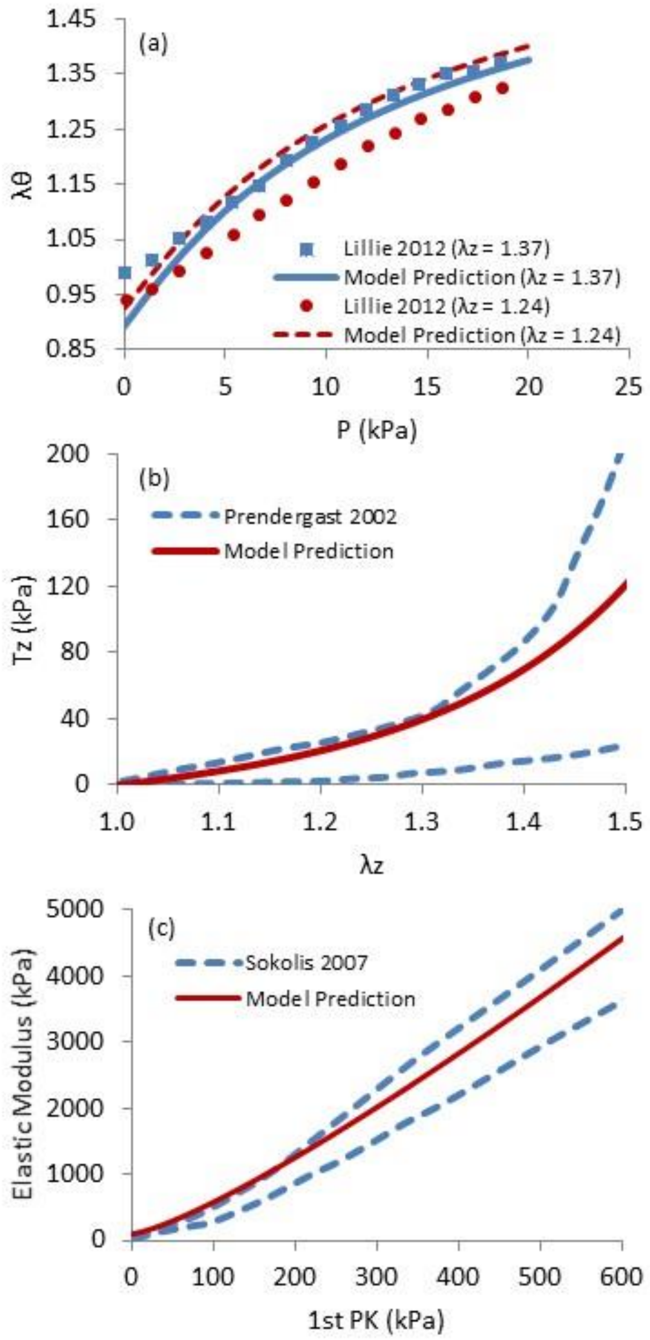

Figure 10– Prediction of the overall model compared to previously published data on porcine aorta. a) Circumferential stretch vs intraluminal pressure at two different longitudinal stretch ratios for inflation tests in the range of physiological pressures, b) Longitudinal Cauchy stress vs longitudinal stretch ratio for uniaxial extension in the longitudinal direction, and c) Tangent elastic modulus vs stress in uniaxial extension in the circumferential direction.

Two additional verification paths were previously reported uniaxial stretch data in $z$ and $\theta$ directions. In the $z$ direction, the calculated Cauchy stress vs. stretch ratio passes through the corridor of the experimental data given by (Prendergast et al., 2003) (Figure 10-b). In the $\theta$ direction, the prediction of the current model was in close agreement with the results of (Sokolis, 2007) in terms of the elastic modulus vs. first Piola-Kirchhoff stress (Figure 10-c). The elastic modulus was defined as the instantaneous slope $dP/d\varepsilon$, in which $P$ is the first Piola-Kirchhoff stress and $\varepsilon$ is the infinitesimal strain. Details of the formulations used to derive the uniaxial response are given in Appendix B. Based on the verifications explained above, it was concluded that the form of the SEDF given in Equation (2.3-a) together with the convexity condition imposed in Equation (6), and two characterization Equations (2.5-a) and (2.5-b), resulted in a sufficiently smooth and unique function that could satisfactorily describe other experimental results.

The maximum stretch ratios in this study ($\lambda_\theta(r_i) = 1.71 \pm 0.15, \lambda_z = 1.46 \pm 0.06$) were below the failure stretch ratios for young human aortas based on uniaxial extension tests in (Mohan & Melvin, 1982) ($\lambda_\theta = 1.89$ and $\lambda_z = 1.78$). The inflation-extension test is not a suitable method to study tissue failure because the sutures used to ligate the branches are typically the weak points in the experimental model. The maximum applied pressure (70 kPa) was close to the average peak pressures reported in chest impacts tests (68 kPa) (Hardy et al., 2008) and maximum peak pressures in sled tests (72 kPa) (Bass et al., 2001) using human cadavers. *In situ* measurement of the longitudinal deformation in chest impact tests (Hardy et al., 2008) revealed that on average, aorta experienced peak Lagrangian strain of $0.21$ in addition to the *in vivo* longitudinal pre-stretch (approximately

1.2 (Holzapfel, Sommer, Auer, Regitnig, & Ogden, 2007)). Consequently, an approximate estimate for the peak $\lambda_z$ in chest impact tests is 1.44 which is statistically equal to the peak $\lambda_z$ achieved in this study ($1.46 \pm 0.06, p = 0.39$). The stress distribution along the wall thickness, calculated from the overall model is shown in Figure 11. The predicted maximum wall longitudinal stress at the inner wall $T_z(r_i)$ (0.65 MPa) was below the failure initiation level reported in (Stemper et al., 2007) for porcine aorta (1.6 MPa). It was therefore concluded that the loading applied in this study represented large deformations that occur in automotive accidents and other chest trauma that involve significant chest compression but kept the samples well below the failure initiation level.

The stretch ratios measured at the physiological pressure were consistent with data reported for the human aorta. At 13 kPa, $\lambda_z = 1.22 \pm 0.03$ was similar to the *in-situ* measured values of 1.2 ± 0.06 (Holzapfel et al., 2007) ($p = 0.51$) and close to the *ex-vivo* values of 1.14 ± 0.05 for young samples in (Labrosse et al., 2013) ($p = 0.004$). At the same pressure, the *ex-vivo* $\lambda_\theta(r_i)$ for young human aorta (1.37 ± 0.05) is comparable to what was found in this study (1.39 ± 0.07, $p = 0.60$). It was concluded that the response of porcine and human aortas to intraluminal pressure are close to each other. An approximately 5-fold increase in pressure (from 13 to 70 kPa), resulted in 22% and 20% increase in of $\lambda_\theta(r_i)$ and $\lambda_z$ respectively. This effect was more pronounced in the $\theta$ and $z$ stresses at the inner wall. The same 5-fold increase in pressure resulted in approximately 16 and 18 folds increases in $T_\theta(r_i)$ and $T_z(r_i)$ respectively. This high sensitivity in stress can be explained by the nonlinear (stiffening) nature of the tissue.

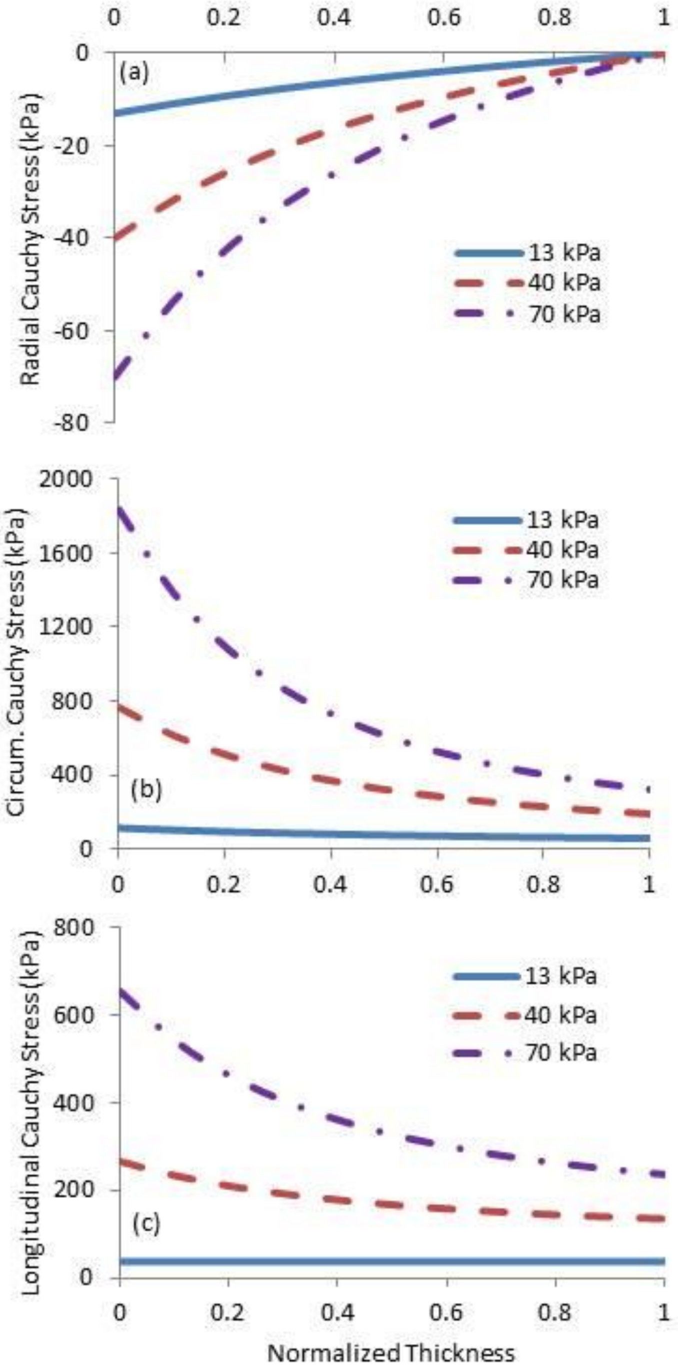

Figure 11– Distribution of a) radial, b) circumferential and c) longitudinal Cauchy stresses across the aorta wall from overall model at physiological (13 kPa) midrange (40 kPa) and maximum (70 kPa) pressures.

The average opening angle measured in this study (40.9 ± 20.2) was lower than previously reported data by Stergiopulos (50±30.7) (Stergiopulos, Vulliémoz, Rachev, Meister, & Greenwald, 2001), Guo (53±28.6) (Guo & Kassab, 2004), and Han (57.2 ± 22.5) (Han & Fung, 1996), for younger pigs (4 year old pigs in this study compared to 3 year old pigs in (Stergiopulos et al., 2001) and young piglets in (Guo & Kassab, 2004) and (Han & Fung, 1996)). This difference may be explained by the effect of aging as the same trend has been reported for mice at early stages of life before puberty (Rachev & Greenwald, 2003). While the importance of opening angle in the arterial wall stress distribution at physiological pressures had been previously shown (Chuong & Fung, 1986), it was verified in this study that the opening angle had a significant effect in supra-physiological pressures as well. To this end, inflation-extension of the overall model was performed by ignoring the residual stress in the artery. The results showed that at 70 kPa, $T_\theta$ and $T_z$ increased at $r_i$ by 38% and 29% and decreased at $r_o$ by 53% and 23%, respectively i.e. the opening angle made the stress distribution more uniform along the wall thickness.

Limitations of this study include ignoring the effects of age, loading rate and inhomogeneity in the constitutive model. It has been reported that arteries become stiffer with age (Greenwald, 2007; Labrosse et al., 2013; Mohan & Melvin, 1982), which can be attributed to a higher collagen content (Ferruzzi, Vorp, & Humphrey, 2011). Porcine aorta, on the other hand, has been considered in the literature as a surrogate for young and healthy human aorta (Bass et al., 2001; Pearson et al., 2008).

While aorta material is rate dependent (Mohan & Melvin, 1982, 1983; Stemper et al., 2007), the longest time constant for a viscoelastic model reported for porcine aorta is 10 s (Hemmasizadeh et al., 2012b). It was therefore assumed that the experiments used in this study with ramp time of 70 s yielded the steady-state elastic response of the tissue. Following the quasilinear viscoelastic (QLV) theory for soft tissues (Y. C. Fung, 1993), the instantaneous elastic response can be obtained from the steady-state response by replacing parameter $c$ in Equation 2.3-a with $c/G_\infty$, where $G_\infty$ is the steady-state normalized relaxation ratio (Laksari, Shafieian, & Darvish, 2012; W. Zhang, Liu, & Kassab, 2007). A recent study on rate dependence of porcine aorta showed 1.5 fold increase in the stiffness from 0.03 to 30 $s^{-1}$ strain rate (Stemper et al., 2007). Therefore, for modeling high-rate applications, the elastic response characterized in the present study should be scaled according to the applied strain rate.

In deriving the material properties, the tissue was assumed to be homogeneous. This assumption was verified earlier for $\theta$, and $z$ directions of the small segments used in this study. In longer segments, for example, it has been shown that for approximately 200 mm distance from upper to lower thoracic regions, the circumferential elastic modulus increases by about 40% (Sokolis, 2007). In the $r$ direction, it has been shown that the outer half is approximately 20% stiffer than the inner half (Hemmasizadeh et al., 2012b). Therefore, under intraluminal pressure loading, it is expected the wall stresses to be higher in the outer half and lower in the inner half of the wall compared to what an average homogenous model would predict. As a result, the stress distribution across the wall thickness is expected to be more uniform. While the material parameters obtained in this study, may not be valid for other regions, it is anticipated that the trends observed in this study to be the same as long as the microstructural architecture is the same.

# CHAPTER 3

# MULTIRATE MECHANICAL BEHAVIOR AND FAILURE PROPERTIES OF AORTIC TISSUE

## Introduction

Although the use of restraint systems has increased in recent years, the overall incidence of blunt aortic injury in car accidents has remained the same (Neschis et al., 2008). By investigating 7,076 car accidents from 1992 to 1999 (Richens & Kotidis, 2003) concluded that airbag and seat belts did not eliminate the risk of injury. This emphasizes the necessity of more comprehensive studies on the underlying mechanisms of traumatic aortic injuries (TAI) and rupture (TAR) in order to improve the effectiveness of automobile passenger safety measures. TAI/TAR in car accidents is caused by a complex state of deformation occurring at high rates. Almost all traumatic ruptures of aorta occur in the longitudinal direction with a transverse tear that usually initiates from intima (Bertrand et al., 2008; Stemper et al., 2007). Although the mechanical behavior of aorta in physiological conditions has been studied before by several research groups, very few studies have investigated the mechanical and failure behavior of aorta in high rate deformations. The goal of this work was to describe the mechanical behavior of aortic tissue near the failure point in a wide range of loading rates.

Collins & Hu (1972) investigated the rate dependence of cylindrical segments of free-end porcine aorta segments by pressurizing the vessel at two different rates corresponding to nominal logarithmic strain rates of 0.005 $s^{-1}$ and 1-3.5 $s^{-1}$. They observed an increase in the longitudinal failure stress with nominal values from 300 kPa to 450 kPa with increasing strain rate although no statistical analysis was presented. They also mentioned that failure strain decreases and stiffness increases with an increase in strain rate but no specific values were reported for these measures.

The failure properties of human aortic tissue were reported by Mohan & Melvin (1982). Uniaxial extensions in both circumferential and longitudinal directions at nominal strain rates of 0.01-0.07 $s^{-1}$ and 80-100 $s^{-1}$ were carried out on samples from descending aorta. They reported an increase in longitudinal and circumferential failure stresses from 1.47 and 1.72 MPa to 3.59 and 5.07 MPa. In contrast to what was reported by (R. Collins & Hu, 1972), no significant difference in failure stretch ratios were observed. (1.47 and 1.53 in longitudinal and circumferential directions in quasi-static loading respectively vs. 1.64 and 1.60 in dynamic loading).

In another article, (Mohan & Melvin, 1983) investigated the failure properties of aortic samples by biaxial bubble inflation experiments at nominal strain rates of 0.01-1 and 20 $s^{-1}$. They reported a consistent rupture of the sample in longitudinal direction, in conformance with data from real car crashes, and reported a significant increase in failure stress from average values of 1.14 MPa in quasi-static to 1.96 MPa in dynamic loading. The corresponding stretch ratios were 1.44 and 1.28 which showed a decreasing trend but it was not statistically significant. These results confirmed their uniaxial extension tests results.

The studies mentioned above did not develop any constitutive model for aortic tissue. Bass and colleagues (Bass et al., 2001) characterized a two-dimensional Fung-type strain energy density function from data obtained by cyclic planar biaxial extension tests on porcine aortic arch samples at two nominal frequencies of 20 and 60 Hz. Their study had the advantage of using the samples from aortic arch which is the most frequent site of TAR; however their model is limited by the number of samples (4 samples), nominal strain rates that have been covered (2 nominal strain rates) and the fact that the strain and stress levels were in the physiological range. They also investigated the rupture properties of aortic tissue by a sudden increase in intraluminal pressure of whole human aortas *in situ* and *ex vivo*. They observed no preferred rupture direction for aorta which is in contrast to experimental data reported before (Mohan & Melvin, 1983) and autopsy observations after car accidents (Bertrand et al., 2008). The reported average failure circumferential stretch ratios at distal and proximal aorta were 1.16 and 1.19 while the longitudinal stretch ratio was 1.13. Failure stress values (0.794 and 0.828 MPa for circumferential and 0.397 and 0.414 MPa for longitudinal direction respectively at distal and proximal aorta) are consistent with the numbers reported by Collins & Hu (1972).

Shah and colleagues (Shah et al., 2006) used planar biaxial experiment to test failure properties of cadaveric samples from ascending aorta, peri-isthmus region and descending aorta at two nominal extension rates of 1 m/s and 5 m/s. The strain rates resulted in the tissue show a wide overlap between the two groups (Lagrangian strain rates of 23-206 $s^{-1}$ for slow speed and 52-230 $s^{-1}$ for high speed) and although the average strain rates found to be significantly different (77.86±43.27 $s^{-1}$ vs. 135.90 ±55.34 $s^{-1}$) no significant difference in mechanical measures were detected. All tissue failures occurred in longitudinal directions similar to real world TAR. Pooling the data from all samples and both extension rates, the average longitudinal and circumferential moduli were found to be 8.87, and 10.57 MPa and failure longitudinal stress and strain were 1.96 MPa and 0.254. Longitudinal stretch tests on whole aorta samples were also carried out with an average strain rate of 11.8 $s^{-1}$ and resulted in average failure engineering stress and Lagrangian strain of 0.75 MPa and 0.221.

In a recent study on failure properties of porcine aorta, Stemper and colleagues (Stemper et al., 2007) used uniaxial extension test to quantify rate dependence and failure properties of the aortic tissue in the longitudinal direction. The samples were tested at four nominal strain rates of 0.06, 0.6, 6 and 30 $s^{-1}$. Statistical analysis showed a significantly lower failure strain at the highest strain rate compared to the 1st and 2nd strain rates groups. On the other hand, failure stress, in general, was observed to increase significantly by strain rate. Similar differences were observed for modulus of elasticity. These results confirm the results of (Collins & Hu, 1972). Specific values of these failure mechanics were not presented, and no constitutive model was characterized based on these data.

The goal of this study was to characterize the rate dependent failure properties and mechanical behavior of porcine aortic tissue for TAI/TAR applications in a wide range of strain rates. The strain rates achieved in this study are an order of magnitude higher than previously published data.

# Materials and Methods

## Test Setup

A multirate uniaxial test setup was designed and built for the purpose of this study (Figure 12). The setup consisted of two support fixtures secured next to a linear impact system (Darvish, 2009). One of the support fixtures was used to support a load cell with high frequency response (25lb, Model 11, Honeywell, Golden Valley, MN) and the other fixture held a pair of shafts which guided the horizontal movement of a crosshead. The two support fixtures were separated to reduce the impact vibration noise in the load cell.

The dynamic crosshead consisted of a plate with two PTFE bearings to allow the free movement over the two guide shafts, and a grip to hold one end of the sample. The other end of the sample was connected the load cell by another grip. The movement was generated by the impact system which consisted of two carriages that could move with nominal speeds of 0.01 to 10 m/s and hit the crosshead (plastic impact using wax) and push the dynamic crosshead forward and cause uniaxial deformation in the sample.

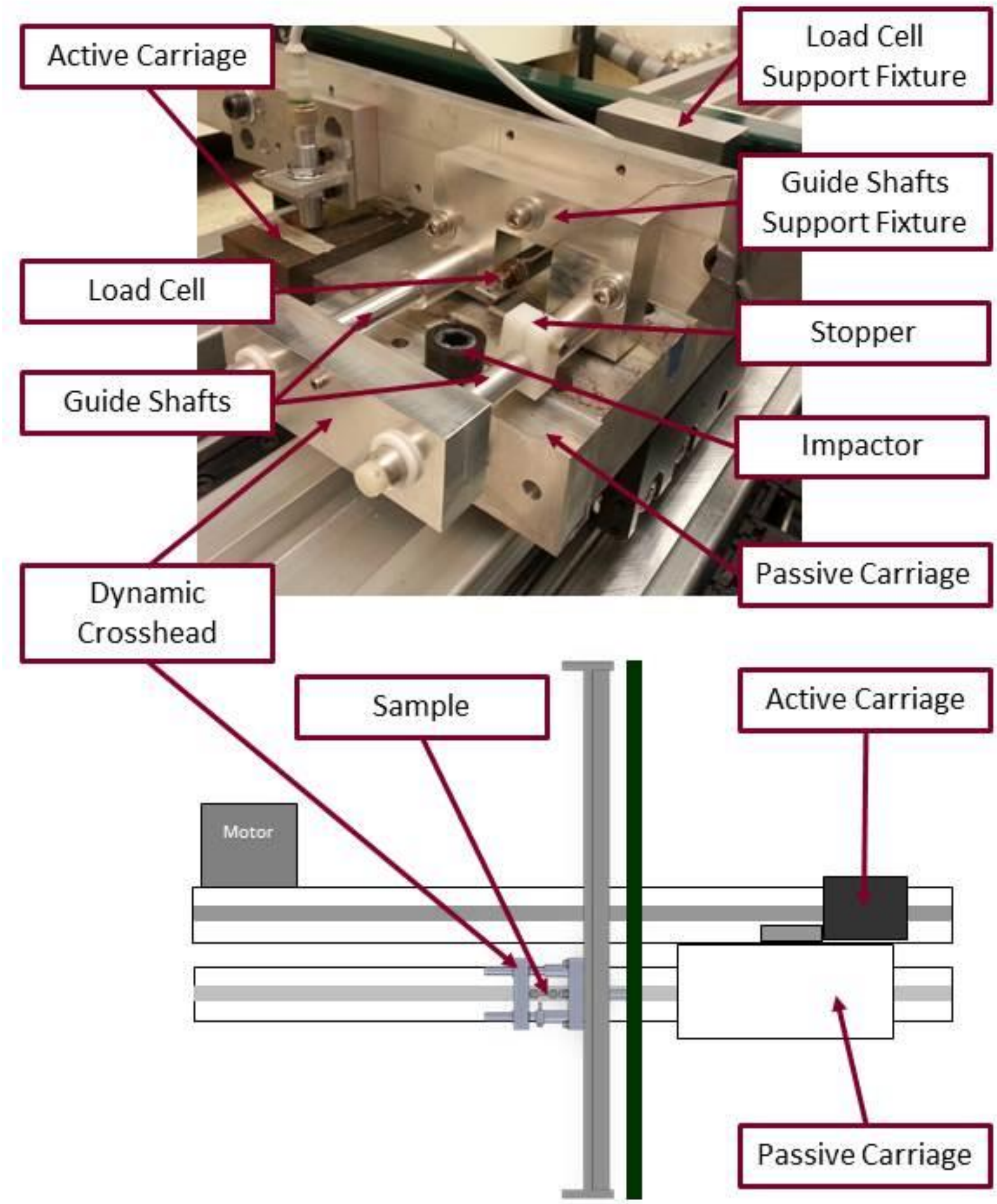
Active Carriage
Load Cell Support Fixture
Guide Shafts Support Fixture
Load Cell
Stopper
Guide Shafts
Impactor
Dynamic Crosshead
Passive Carriage
Sample
Active Carriage
Motor
Passive Carriage

Figure 12– The custom-made multirate uniaxial test system. The sample extension is caused by pushing the dynamic crosshead by the passive carriage. More explanation is given in the text.

The time history of strain rate in the sample depended on the speed of the dynamic cross head. One of the design goals was to decrease the time duration of the acceleration phase of the dynamic crosshead in order to achieve a constant strain rate for most of the extension period. This period was negligible in the low rate tests. However, in high rate tests and in particular at the impact speed of 10 m/s, it was a considerable portion of the loading. Figure 13 shows several frames from the high speed video (Phantom v4.2, Vision Research, Wayne, NJ), pointing to the setup from the side, showing the active carriage and dynamic crosshead at the time of impact. The speed of the dynamic crosshead becomes constant before 2 ms which was before any tear was detected in the samples. In was therefore concluded that the failure of the samples occurred at constant extensive strain rate. For lower rates, a constant strain rate was achieved much earlier than failure. Movement of the dynamic crosshead in the vertical direction was less than 1 mm and the corresponding error in the in-plane strain measurement was determined to be less than 1%.

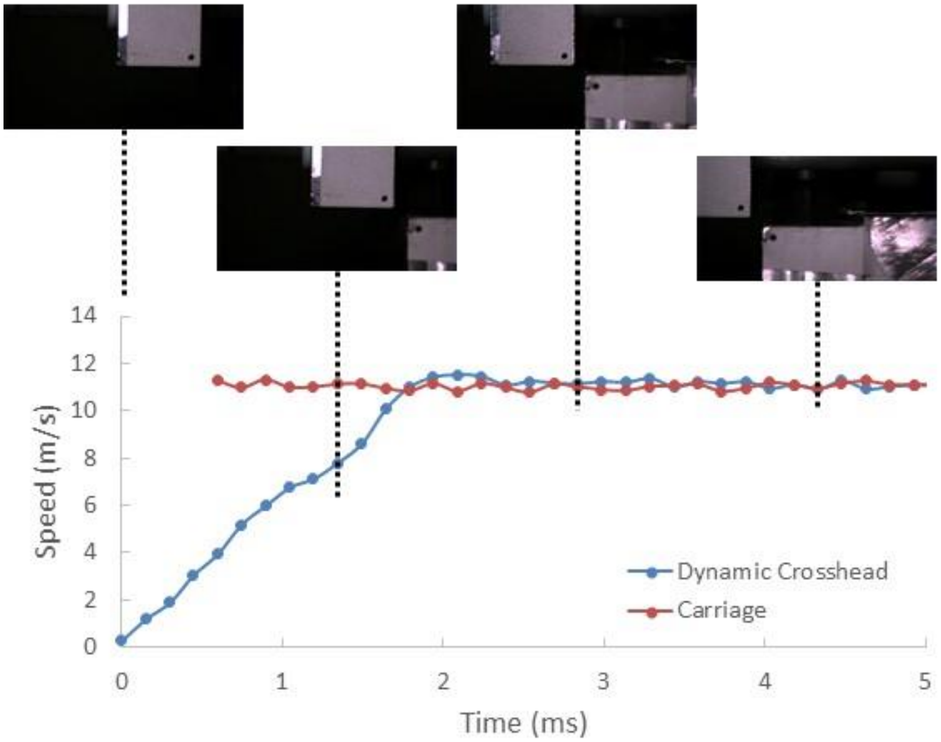

Figure 13– Verification of constant extension speed at the time of failure: The Figure shows the side view videos and the measured horizontal speed of the dynamic crosshead from the time of impact until the end of the course. For 10 m/s constant speed was reached before 2 ms.

## Sample Preparation

The experimental results of 52 samples from 20 porcine aorta specimens are reported here. Fresh porcine aortas were obtained from a local slaughterhouse and transported in ice-cold Phosphate Buffered Saline (PBS) to the laboratory. Adipose and connective tissues were removed from the specimens. Dumbbell shaped samples (with 13 mm length in 5 mm width gage length) were cut out, using a custom-made punch, at the isthmus region in longitudinal (L) (n=26) and circumferential (C) (n=26) directions (Figure 14). The samples location and orientation were chosen such to minimize the effect of inhomogeneity in the longitudinal direction. The location of the proximal circumferential samples was just below the left subclavian artery. The thickness of the samples was measured in the unloaded state by a customized dial gauge indicator. Samples were kept in 4°C PBS until 10 minutes before the test. The experiments were conducted at room temperature. The samples were tested within 12 hours post-mortem.

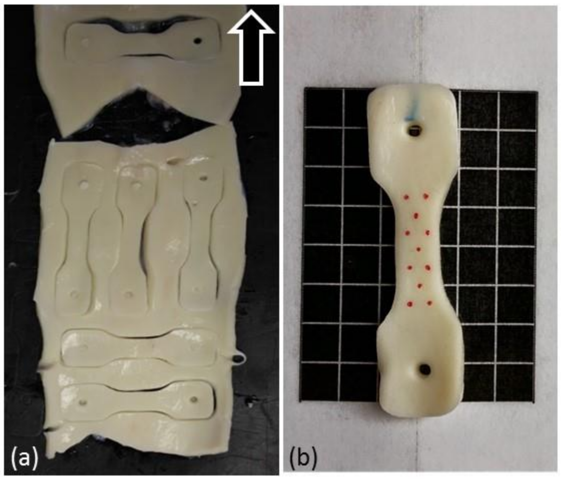

Figure 14- Sample Preparation a) Samples were cutout from aortic istmuth. The arrow shows the longitudinal direction and pointing to the proximal side. b) The sample deformation was analyzed by tracking ink dots as photo targets. The scale grid is 5 mm.

An array of 11 dots was marked on the intimal side of the samples using a Sharpie pen. Samples were preconditioned manually with five cycles to approximately 20% strain (average physiological strain) and then the sample was set manually to its initial (no-load) length by a stopper behind the dynamic crosshead. This no-load length was verified by the fact that the load cell showed a negligible force (less 0.1 N). The experiments were carried out with nominal impact speeds of 0.01 (n=8), 0.1 (n=19), 1 (n=15), and 10 m/s (n=10) that will be referred to Rates 1 to 4 respectively.

The deformation of the sample was recorded by the high-speed camera at 0.5, 1, 5 and 13 kfps for the Rates 1 to 4 respectively. The load cell data was recorded at five times higher rates. An inertia compensation accelerometer (Endevco, Meggitt Sensing Systems, Irvine, CA) was mounted to the load cell support fixture to verify that the load cell body vibrations due to the impact were negligible.

### Calculation of Strain and Stress

The deformation of the sample in the horizontal plane, with axes $x_1$ and $x_2$ (subscripts 1 and 2) corresponding to the direction of extension and perpendicular to that respectively, was calculated by an in-house MATLAB code for a linear triangular element. A set of 12 triangular meshes was constructed with 1x3 resolution (Figure 15). The displacement field in each element, using a Lagrangian approach, was assumed to be a linear function of the initial position as

$$\begin{bmatrix} u_1 \\ u_2 \end{bmatrix} = \begin{bmatrix} a_{10} & a_{11} & a_{12} \\ a_{20} & a_{21} & a_{22} \end{bmatrix} \begin{bmatrix} 1 \\ X_1 \\ X_2 \end{bmatrix} \tag{3.1}$$

where vector $\boldsymbol{u}$ is the displacement vector and $\boldsymbol{X}$ is the initial positions vector of a marker in the initial frame. Constants $a_{ij}$, for each element and at each time step, were calculated by solving Equation 3.1 from known vectors $\boldsymbol{u}$ and $\boldsymbol{X}$ for the three nodes of the element. The two-dimensional deformation gradient $\boldsymbol{F}$ can be written as

$$\boldsymbol{F} = \boldsymbol{I} + \nabla\boldsymbol{u} = \begin{bmatrix} \lambda_1 & a_{12} \\ a_{21} & \lambda_2 \end{bmatrix} \tag{3.2}$$

in which $\lambda_1 = 1 + a_{11}$ and $\lambda_2 = a_{22} + 1$ are the stretch ratios. The smallness of $a_{12}$ and $a_{21}$, compared to $a_{11}$ and $a_{22}$ was verified (less than 5%) and therefore, the deformation was assumed to be uniaxial ($a_{12} = a_{21} = 0$). A sample result of the strain analysis is shown in Figure 15. The linear (engineering) strain measure $\varepsilon$ was defined as $\varepsilon = \lambda_1 - 1$ and strain rate as $\dot{\varepsilon}$.

The first Piola-Kirchoff (1st PK) stress (engineering stress) in the extension direction was calculated by

$$P_1 = \frac{F_1}{wh} \tag{3.3}$$

in which $F_1$ is the recorded force, $h$ is the initial thickness and $w$ is the initial width of the sample. The corresponding Cauchy stress $T_1$ was calculated by

$$T_1 = \lambda_1 P_1 \tag{3.4}$$

For simplicity, subscript 1 is omitted in the subsequent formulas.

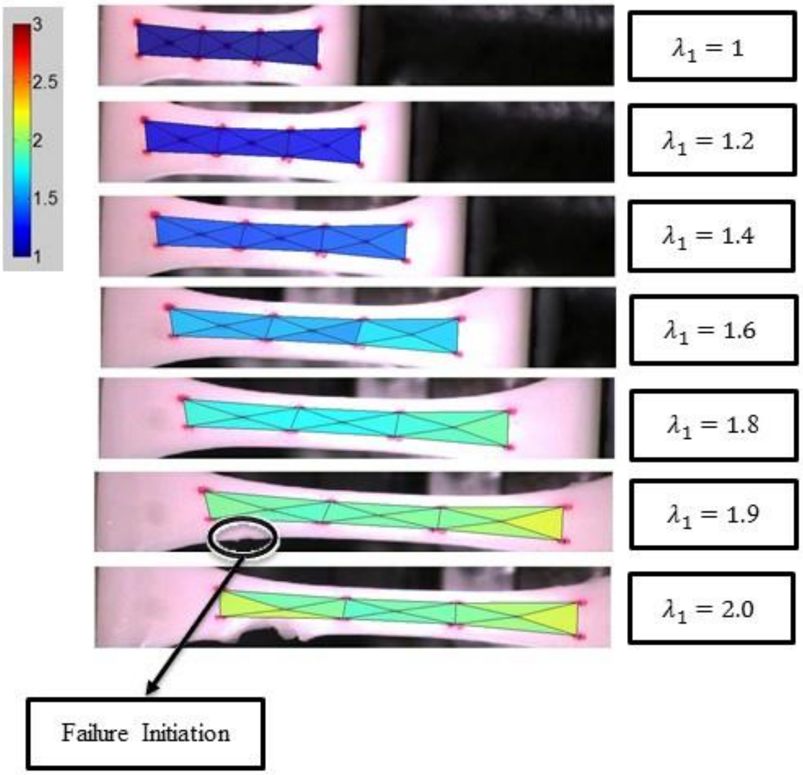
3
2.5
2
1.5
1
$\lambda_1 = 1$
$\lambda_1 = 1.2$
$\lambda_1 = 1.4$
$\lambda_1 = 1.6$
$\lambda_1 = 1.8$
$\lambda_1 = 1.9$
$\lambda_1 = 2.0$
Failure Initiation

Figure 15– Representative results of image analysis and strain calculations. The color bar shows the stretch ratio in the direction of extension ($\lambda_1$). The failure initiation (tear in the intimal side) was determined by examining the images.

## Measures of Material Behavior

Figure 16 shows a typical stress strain-curve. Failure initiation (FI) was defined as the state in which the first intimal tear was observed in the videos. Three distinct regions were identified in $P - \varepsilon$ curves before FI: a linear toe region, a nonlinear transition region, and a linear pre-failure region. To identify these regions a piecewise linear-cubic-linear function in the following form was fitted to the curves by a least square method:

$$P = \begin{cases} a_1\varepsilon, & \varepsilon \leq \varepsilon_{t1} \\ a_2\varepsilon^3 + b_2\varepsilon^2 + c_2\varepsilon + d_2, & \varepsilon_{t1} < \varepsilon < \varepsilon_{t2} \\ a_3\varepsilon + b_2, & \varepsilon \geq \varepsilon_{t2} \end{cases} \tag{3.5}$$

In which $\varepsilon_{t1}$ and $\varepsilon_{t2}$ are the strain corresponding to the first and second transition points and the other constants define the shape of the curves. The coordinates of the transition points in the $P - \varepsilon$ graph together with $a_1$ and $a_2$ were optimized and the other parameters were calculated based on considering a second order continuity ($P$ and its 1st derivative) at the transition points. The pre-failure modulus $M = a_3$ was used for rate dependence analysis.

The strain rate corresponding to the linear pre-failure region, i.e., the slope of a line fitted to the $\varepsilon - t$ curves in this region, was used as the measure of failure strain rate. In summary, the following material parameters were chosen for investigating the effect of the strain rate:

- $\varepsilon_{FI}$ and $T_{FI}$: Strains and Cauchy stresses at FI (where the first tear was observed in videos) in the circumferential and longitudinal directions (referred to as *C* and *L* directions).
- $\varepsilon_{UTS}$ and $T_{UTS}$: Strains and Cauchy stresses at ultimate tensile strength (UTS) in *C* and *L* directions.
- $M$: Pre-failure linear moduli at the linear pre-failure region in *C* and *L* directions.

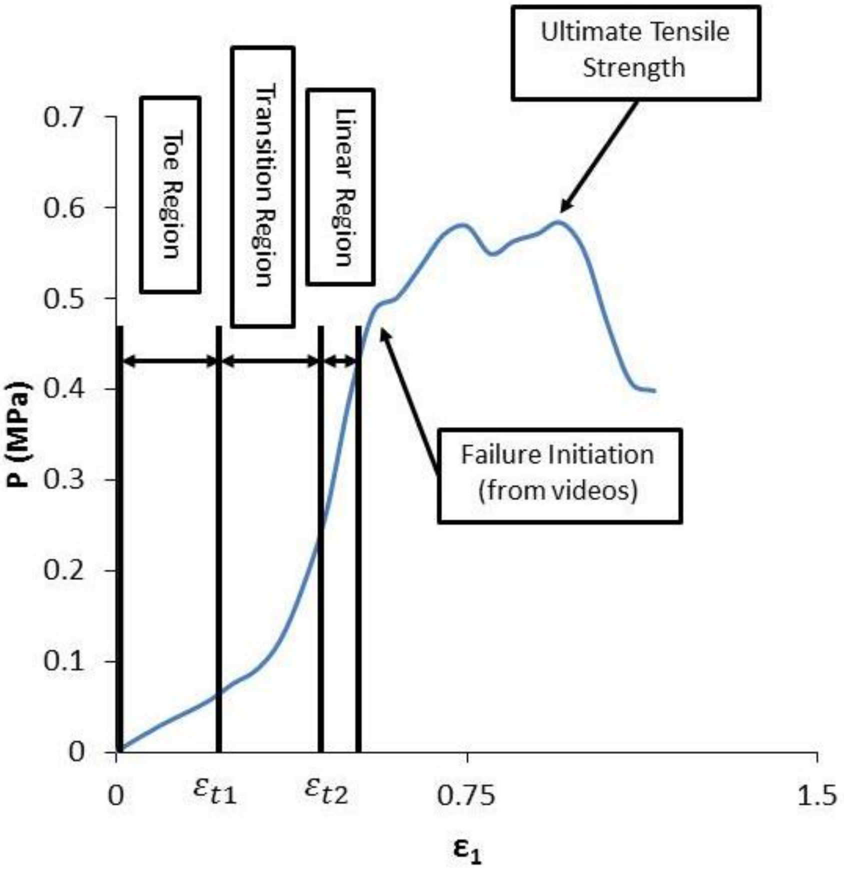

Figure 16– A typical stress-strain curve: Three regions and two transition points were observed before failure: a linear toe region, a nonlinear transition region, and a linear pre-failure region. The failure initiation state (FI), based on the first intimal tear in video images, and the ultimate tensile strength (UTS) were defined based on the peak stress,

### Statistical Analysis

Based on the preliminary results and previously published data, and assuming the measured parameters to be normal, the following statistical hypotheses were tested:

- It was hypothesized that $\varepsilon_{FI}$ and $\varepsilon_{UTS}$ were not rate dependent but were dependent on the test direction. This hypothesis was tested by two-way analysis of variance (ANOVA) with rate and test direction as the factors.
- Dependence of $T_{FI}$ and $T_{UTS}$ on the test direction has been shown before. It was hypothesized that $T_{FI}$ and $T_{UTS}$ were directly related to the strain rate. This hypothesis was tested by a linear regression between $T$ and $\log\dot{\varepsilon}$.
- It is known that the aortic tissue is stiffer in the circumferential direction. It was hypothesized that the tissue is viscoelastic and therefore $M$ was rate dependent. This hypothesis was tested by one-way ANOVA for each direction, with rate as the factor.

Statistical significance was assumed when $p < 0.05$.

## Results

The values reported in this section are the means and standard errors of the means (mean ± SEM). Error bars in the graphs show the SEM. The strain rates corresponding to loading Rates 1 to 4 were found to be $0.32 \pm 0.03, 3.33 \pm 0.19, 31.2 \pm 4.5,$ and $451 \pm 27$ $s^{-1}$. Therefore, four orders of magnitude of strain rates were represented which is significantly wider than previous studies.

### Failure Strains

Figure 17-a shows $\varepsilon_{FI}$ and $\varepsilon_{UTS}$ in $C$ and $L$ directions. Two-way ANOVA showed that rate had no effect on $\varepsilon_{FI}$ $(F(3,44) = 1.24, p = 0.31)$ while test direction had a significant effect $(F(1,44) = 48.6, p < 0.001)$. On the contrary, ANOVA for $\varepsilon_{UTS}$

showed a significant effect of rate ($F(3,44) = 4.53, p = 0.007$) and no effect of direction ($F(1,44) = .04, p = 0.85$). To further investigate the effect of rate on $\varepsilon_{UTS}$, one-way ANOVA was performed for each direction separately. The post-hoc Tukey-Kramer test revealed that only a significant difference existed between Rates 2 and 4 in $L$ direction. Figure 17-b shows the pooled $\varepsilon$ from all rates for *C* and *L* directions at FI and UTS states. While $\varepsilon_{FI}$ was higher for *C* direction, both *C* and *L* directions had statistically equal $\varepsilon_{UTS}$. The difference between $\varepsilon_{FI}$ and $\varepsilon_{UTS}$ was not significant for *C* direction.

Failure mechanisms in the two directions, i.e., strains between FI and UTS states, were found to be different based on high-speed video images. Snapshots from the initial stretch to rupture of representative *C* and *L* samples are shown in Figure 18. Samples in *L* direction ruptured from multiple points and the time duration between FI and UTS was longer compared to *C* samples in which the rupture occurred at one location and propagated

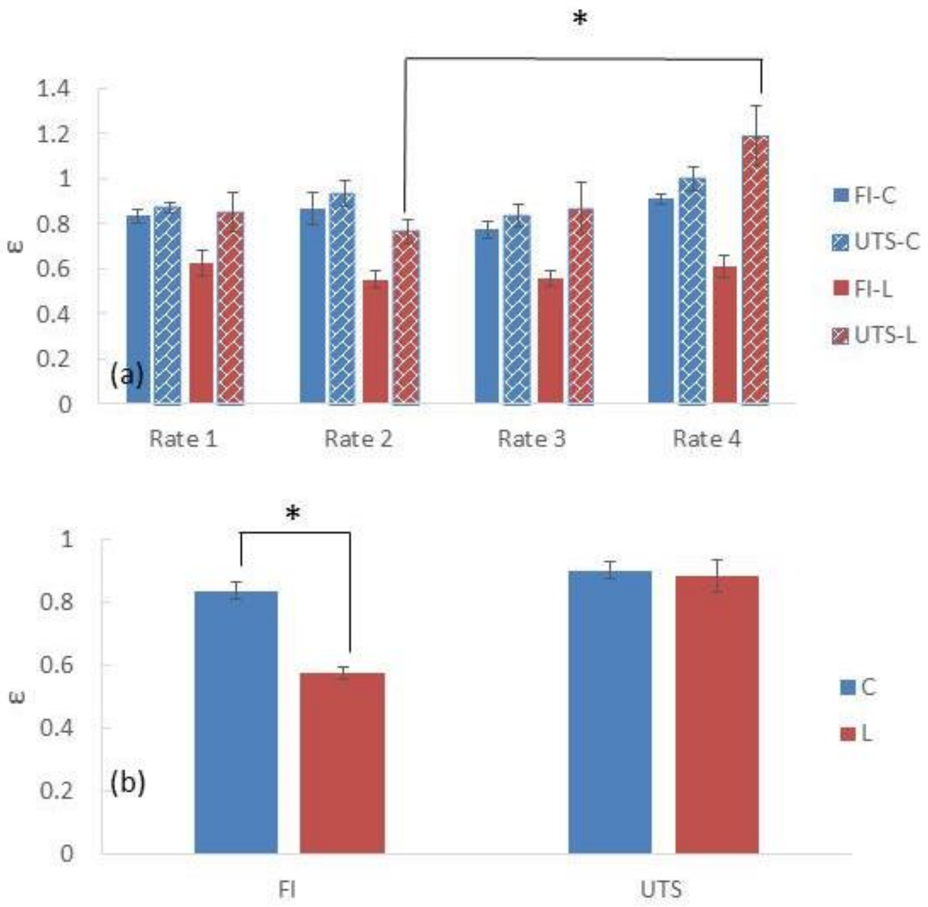

Figure 17– Strain at FI and UTS in *C* and *L* directions a) for fours loading rates and b) on average for all rates. The only significant rate dependence was observed in $\varepsilon_{UTS}$ in the longitudinal direction between Rate 2 and Rate 4 (p=0.007). It was concluded that failure strains are not in general rate dependent. The FI state was significantly different in *C* and *L* directions and it took more strain in *L* direction to reach UTS after FI.

quickly to failure. On average, $\varepsilon_{FI}$ was 0.85±0.03 and 0.58±0.02 for *C* and *L* samples respectively. The pooled value for $\varepsilon_{UTS}$ for both directions was 0.89±0.03.

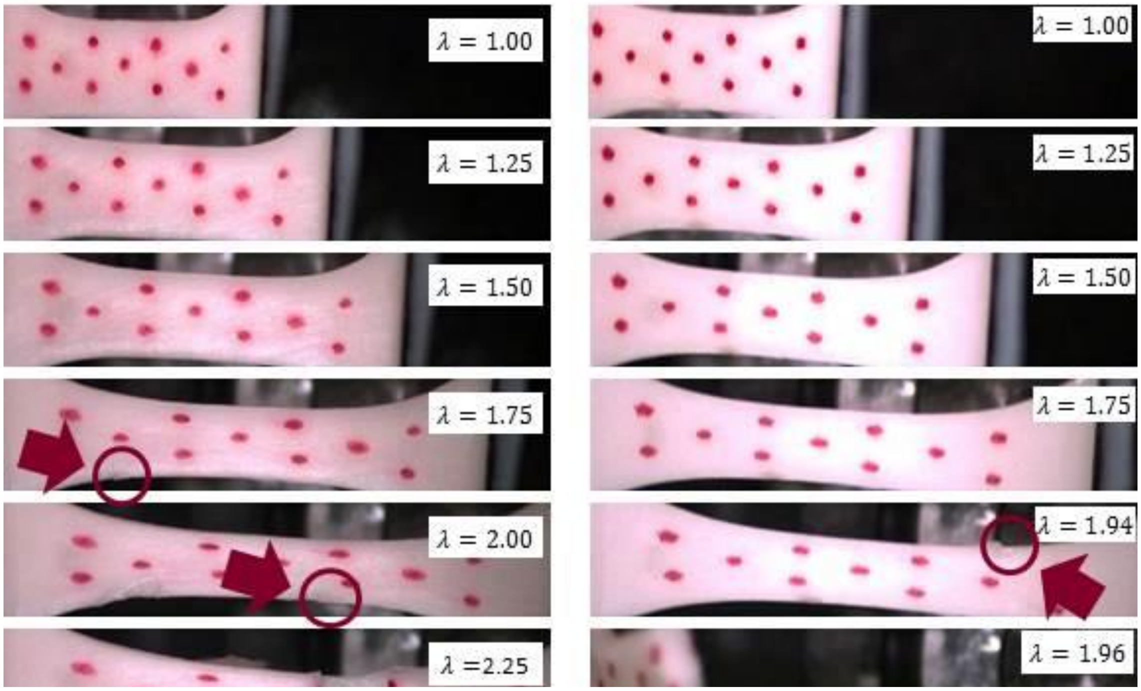

$\lambda = 1.00$
$\lambda = 1.25$
$\lambda = 1.50$
$\lambda = 1.75$
$\lambda = 2.00$
$\lambda = 2.25$
$\lambda = 1.00$
$\lambda = 1.25$
$\lambda = 1.50$
$\lambda = 1.75$
$\lambda = 1.94$
$\lambda = 1.96$

Figure 18– Typical failure process observed in *L* (left) and *C* (right) directions. Failure in *L* direction occurred gradually over a wide range of strains. The failure in *C* direction was abrupt.

### Failure Stresses

A direct relationship with strain rate was observed for both failure stress measures, $T_{FI}$ and $T_{UTS}$. For each direction, a linear regression in the form of $a + b \log \dot{\varepsilon}$ was used to characterize the rate dependence. Figure 19 and

Table 3 summarize the regression results. While the regressions were statistically significant, $R^2$ values were relatively low, which can be attributed to specimen-to-specimen variability. Samples from each pig specimen were tested in only one or two rates. Therefore, the effect of variability due to specimen could not be separated.

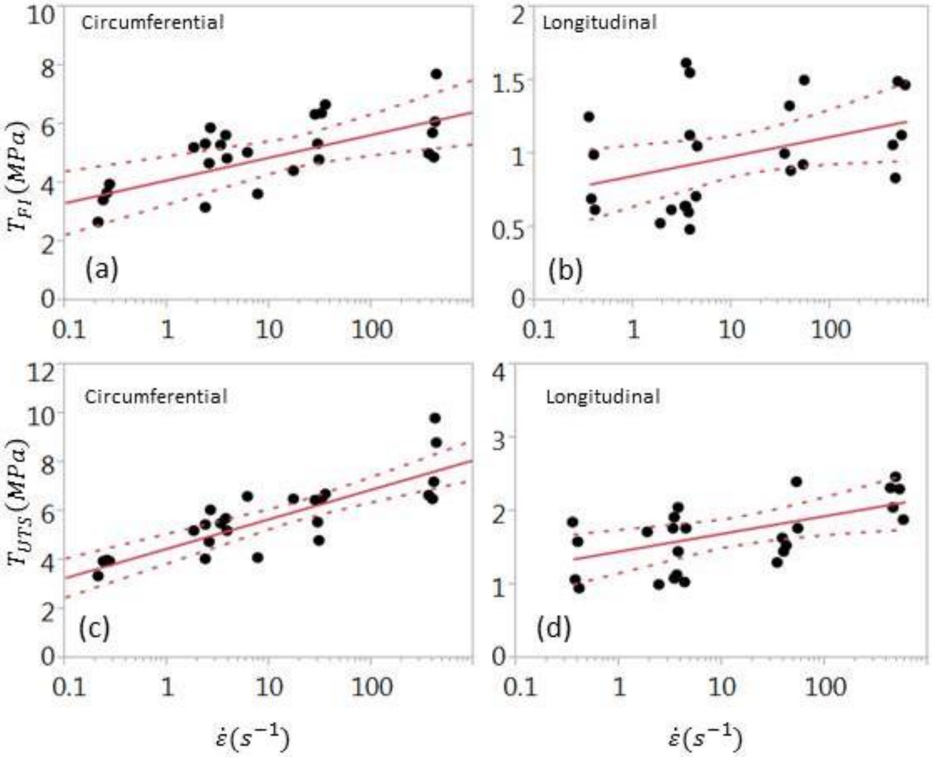

Figure 19– Change of failure stresses with strain rate. Cauchy stress at a) FI in *C*, b) FI in *L*, c) UTS in *C*, and d) UTS in *L* direction versus strain rate. The increasing trend of failure stresses with strain rates were found to be significant. Relatively low $R^2$ values showed that the overall variation in stresses could not be explained only by strain rate

Table 3–Regression results for failure stress measures versus strain rate in both *C* and *L* directions in the form of $T = a + b\ \log\dot{\varepsilon}$

| Stress measure | direction | a ± SE | b ± SE | F statistics | $\boldsymbol{R^2}$ |
|---|---|---|---|---|---|
| $T_{FI}$ | *C* | $4.11 \pm 0.33$ | $0.37 \pm 0.10$ | $F(1,24) = 10.8, p = 0.003$ | 0.31 |
| $T_{UTS}$ | *C* | $4.49 \pm 0.25$ | $0.52 \pm 0.08$ | $F(1,24) = 47.9, p < 0.001$ | 0.67 |
| $T_{FI}$ | *L* | $0.85 \pm 0.09$ | $0.06 \pm 0.03$ | $F(1,24) = 4.29, p = 0.049$ | 0.16 |
| $T_{UTS}$ | *L* | $1.46 \pm 0.13$ | $0.10 \pm 0.04$ | $F(1,24) = 7.09, p = 0.014$ | 0.24 |

### Pre-Failure Linear Modulus

The aortic tissue, as expected, showed a significant anisotropy when values of *M* were compared between *C* and *L* directions ($M = 12.4 \pm 0.8$ and $M = 3.2 \pm 0.3$ for *C* and *L* directions respectively). For *C* direction, $M$ was found to be rate dependent ($F(3,22) = 4.93, p = 0.009$) while in $L$ direction this dependence, although it showed a similar increasing trend with rate, was not statistically significant ($F(3,22) = 0.8, p = 0.51, \beta = 0.8$). Figure 20 summarizes the rate dependence of *M*. Based on the post-hoc Tukey-Kramer test in *C* direction, it was found that a significant increase (approximately 60%) occurred between Rates 2 and 3. It was therefore, concluded that viscoelasticity was more prominent in the *C* direction. The change in *M* can be attributed to relaxation time constants that cause a transition in the time scales that correspond to Rates 2 and 3. These time constants are therefore approximately between 1/30≈0.03 and 1/3≈0.3 s.

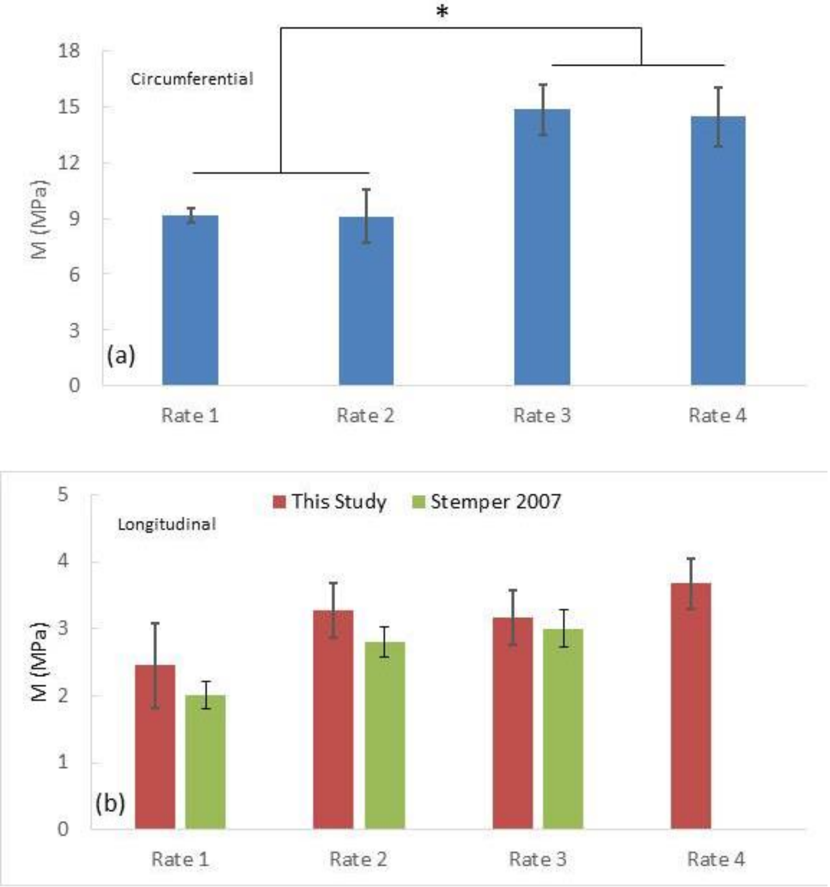

Figure 20- Rate dependence of modulus *M* in a) *C*, and b) *L* directions, Both directions showed an increasing trend with strain rate. The differences were found to be significant when comparing Rate 1 and Rate 2 with Rate 3 and Rate 4 in *C* direction (p=0.009). The results in *L* direction were comparable (p=0.4) with Stemper et al. (2007) results.

## Discussion

The multirate uniaxial test setup was utilized to cover a wide range of strain rates and increase the maximum strain rate ten folds compared to the previous results for porcine aorta (Stemper et al., 2007). Despite some drawbacks of uniaxial extension experiment for biological tissues, e.g. alteration of physiological geometry (Humphrey, 2002) and the assumption of uniform stress through the thickness of tissue (Labrosse et al., 2013), it was chosen for this study since applying the high strain rates beyond 300 $s^{-1}$ was currently not feasible in other test modes including inflation/extension tests and planar biaxial tests. The high strain rates applied in this study made the results better applicable to TAI/TAR applications.

Two states related to aorta failure were distinguished in this study. In addition to the UTS state, which is commonly considered in previous studies, the FI state was also considered. The FI state is important in mechanical modeling of the tissue since a viscoelastic hyperelastic model will no longer work after this state, and a model of partial failure needs to be considered.

The aortic tissue in the isthmus region is considered an elastic artery and primarily consists of elastic lamellae (concentric layers of elastin) and collagen fibers that run primarily in the circumferential direction (Holzapfel, 2006). Based on the results of this study, the failure mechanism of aorta can be partly explained. Collagen fibers are naturally undulated and become straighter as the load is increased. Therefore, in the elastic part of the stress-strain curve, this change in undulation results in a low-stiffness toe region followed by a nonlinear region in which the stiffness dramatically increases. The stretch ratios at FI and UTS were found to be rate independent. This is in agreement with previously published data on the human aorta (Mohan & Melvin, 1982). We also found the stretch ratios at UTS to be statistically equal in $C$ and $L$ directions. This has also been reported previously by (Mohan & Melvin, 1982). These observations suggest that the primary failure mechanism involves a strain-based and rate independent element that is equally contributing to both directions.

Stemper and colleagues (Stemper et al., 2007) experiments are the closest available data in the literature to this study in terms of covering four order of magnitudes of strain rate and testing porcine aortas in uniaxial extension. It should be noted that they tested the samples in the longitudinal direction only. In comparison, their highest three rates are in the same order of magnitude as Rates 1 to 3 of this study. Their lower rate is one order of magnitude lower than Rate 1. They observed that the failure strain was lower at Rate 3. This discrepancy between their results and the results of this study may be attributed to the tissue sample cutout region. They extracted their samples from a longer segment of the descending thoracic aorta (DTA). This may result in a relatively larger variability in their results due to material inhomogeneity. It has been noted that toward the distal end of DTA, the material becomes stiffer (Hemmasizadeh et al. 2014).

The increase of $T_{FI}$ and $T_{UTS}$ with strain rate, as was observed in this study, was in agreement with the results of previous studies (Mohan & Melvin, 1982; Stemper et al., 2007). The increase in $M$ with rate, also in agreement with previous studies, can be a manifest of the viscoelastic behavior of the tissue. In this study, however, the change in $M$ was only significant in the $C$ direction. This implies that the tissue viscoelasticity may be anisotropic, which has not been reported before. Predicting a time constant between 0.03 and 0.3 s is in agreement with previous studies (e.g. Hemmasizadeh et al. 2014)

The aortic tissue is anisotropic as this was demonstrated in the significant difference observed between longitudinal and circumferential maximum stresses (Figure 19). The degree of this anisotropy and the orientation of any preferred directions are debatable. The results of this study showed that the $a_{12}$ and $a_{21}$ terms in Equation (3.2) were less than 5% of $a_{11}$. This means that, with 5% error, directions 1 and 2 used in this study can be considered as the principal axes of an orthotropic material. This finding is consistent with the results of other researchers (Holzapfel & Ogden, 2009; Sacks, 2000).

One of the limitations of this work is that we were looking at the intimal side of the tissue to detect the initiation of failure. Stemper et al. (2007) used two cameras and recorded failure experiments from both sides of the sample. They reported that the initiation of failure always occurred at the intimal side which supports our choice of placing the camera on the intimal side. However, since aortic tissue has multiple layers, any partial failure that may have started from within the layers, e.g., slippage of the layers with respect to each other, could not be detected with our method.

# CHAPTER 4

# MECHANICAL INSTABILITY OF AORTA DUE TO INTRALUMINAL PRESSURE

## Introduction

While traumatic aortic injury (TAI) and rupture (TAR) continue to be a major cause of morbidity and mortality in motor vehicle accidents, their underlying mechanisms are not well identified yet. It has been nevertheless agreed upon that a single factor cannot lead to TAR and it is believed the rupture is the result of a complex state of loadings and deformations. The mechanisms proposed for injury include intraluminal pressure increase, relative movement of aorta with respect to mediastinal structures, direct impact to bony structures, local osseous pinching and water hammer effect (Neschis et al., 2008). As a contributing factor to TAI, we propose the mechanical instability mechanism in which the elevation in stress due to bending of the vessel contributes to the overall state of stress to the injury threshold and increases the risk of injury.

The results of this study might have some clinical implication too, as the deviation of blood vessels from the original configuration into a bent shape has been reported in all regions of the vascular system including cerebral (Moody et al., 1997), retinal (Sasongko et al., 2011), carotid (Togay-Isikay & Kim, 2005), coronary (Li et al., 2011), ulnar (Ferris et al., 2000), radial (Lo et al., 2009), femoral (Wood et al., 2006) and iliac (Carpenter et al., 2001) arteries. Such deviations have also been noted in aorta including abdominal

(Fillinger et al., 2004) and thoracic (Criado et al., 2002) aorta. A bent configuration alters the blood flow in arteries and develops regions of low and high wall shear stress. These regions are susceptible to atherosclerosis and thrombosis in the long term (Chesnutt & Han, 2011; Friedman et al., 1983; Malvè et al., 2014). In addition, this alteration reduces the blood pressure downstream of the bent section and causes a deficiency in blood supply and may cause ischemia (Zegers et al., 2007). Bent arteries can add to the complexity of cardiovascular surgeries such as endovascular repair of abdominal aortic aneurysm, carotid stenting and transradial coronary procedures (Carpenter et al., 2001; Derubertis et al., 2011; Lo et al., 2009; Wolf et al., 2001; Yoo et al., 2005).

Figure 21 gives a schematic diagram of aorta before and after mechanical instability. Part of the arch (after the Isthmus region) and the beginning of descending aorta are relatively free to move compared to other regions that are constrained by the heart, branches, and surrounding connective tissues. The underlying mechanism can be modeled as mechanical instabilities similar to a column under axial loading (Han, 2007, 2008, 2009c; Rachev, 2009). To this end, blood vessel and the fluid inside is considered as a composite beam under compressive force from blood pressure and tensile force from the surrounding tissue at both ends. Several clinical observations are in agreement with this model. For example, hypertension is associated with the prevalence of arterial kinking and tortuosity (Hiroki et al., 2002; Pancera et al., 2000). On the other hand, it has been reported that decreasing the axial tension of an artery by implanting an arterial graft will induce tortuosity *in vivo* (Jackson et al., 2005; J. Zhang, Liu, & Han, 2014).

There have been several studies on the mechanical instability of blood vessels. Misra and colleagues studied the stability of blood vessels using the bifurcation theory and the theory of small deformations superimposed on large deformations. As a numerical example, they used a model of thoracic aorta and plotted the stability regions of a 30 mm segment of the artery for a domain of axial and circumferential stretch ratios (J. C. Misra & Singh, 1985; J. Misra & Choudhury, 1982). They did not relate the stability of the blood vessel to its internal pressure which was reported in another study by Han. He used the classic theory of static buckling of columns and calculated the critical internal pressure that initiates the buckling in the artery  and validated the model against *ex vivo* experimental

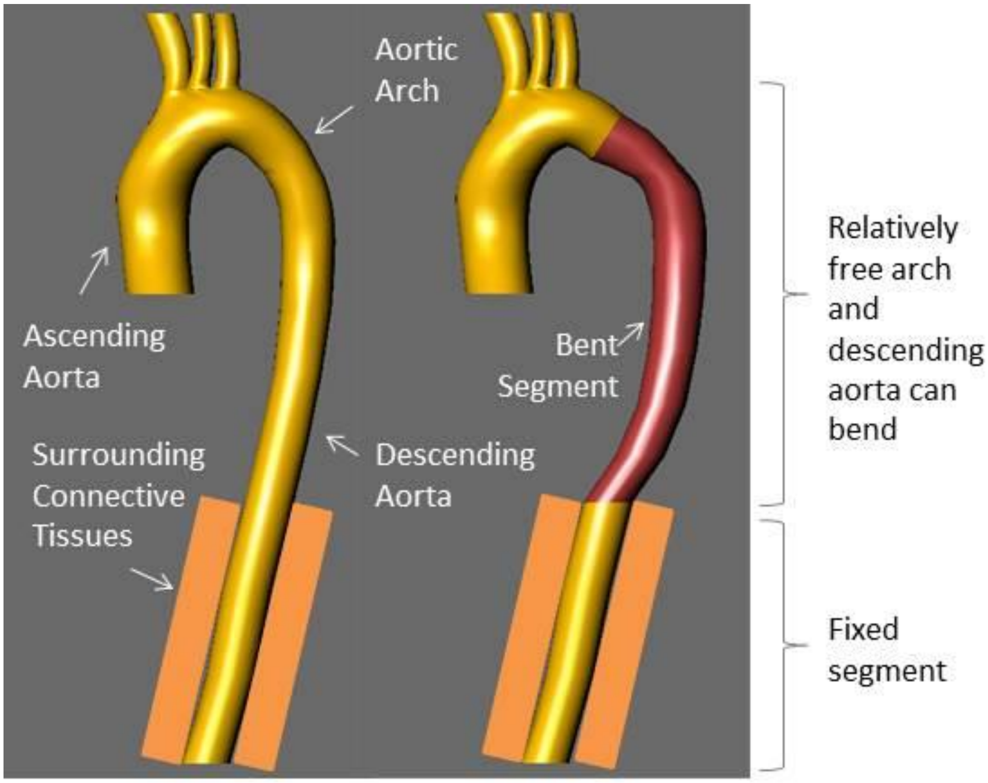
Aortic
Arch
Ascending
Aorta
Surrounding
Connective
Tissues
Descending
Aorta
Bent
Segment
Relatively
free arch
and
descending
aorta can
bend
Fixed
segment

Figure 21– Schematic diagram of aorta before (left) and after (right) mechanical instability. Approximately 100 mm of descending aorta (shaded) is shown with 10 mm deflection at the midsection.

results (Han, 2007, 2008). In another study, the effect of perivascular tissue on buckling of arteries was modeled as linear springs. It was shown that the instability is possible even when the artery is supported by surrounding tissue although it occurs at higher pressures, and the artery may buckle in higher modes (Han, 2009a).

Because blood pressure pulsation creates time-varying load on the blood vessels *in vivo*, the system is dynamic and inherently static buckling theory is not an appropriate model. Rachev implemented the theory of dynamic instabilities to describe the stability behavior of the arteries under pulsatile pressure (Rachev, 2009). In mathematical sense, a dynamic system is (Lyapunov) stable if for all initial conditions close to an equilibrium point, the response of the system remains bounded at any time (Jordan & Smith, 2007). Using parametric resonance for dynamic systems with periodic coefficients (Bolotin, 1964), Rachev showed that arteries may become unstable under pressures lower than the critical pressure for static buckling. For numerical examples, the Fung model for rabbit carotid artery was used (Fung et al., 1979). In order to solve the equation of motion, Rachev assumed that the artery behaves as a beam with pinned-pinned boundary condition (PPBC). The dynamic stability characteristics of an artery for the case of clamped-clamped boundary condition (CCBC) has been reported in only one study by (Liu & Han, 2012) in which there was a discrepancy between the experimental and theoretical results.

In the current study, the theory of dynamic instability is implemented for the case of aorta with PPBC and CCBC. The material properties of porcine thoracic aorta (Chapter 2) were used as a surrogate for young and healthy human aorta. Using an analytical model, the level of stress in the tissue is compared between straight and bent inflated aorta segments and the increase in the risk of injury due to trauma is discussed.

## Methods

Following (Rachev, 2009), we consider a segment of aorta along the longitudinal $z$ axis at a finite deformed state defined by the mean intraluminal pressure $\bar{P}$ and the axial stretch ratio of $\lambda_z$ (Figure 22-a). The dynamic equation of motion of aorta and the intraluminal fluid, as a composite Euler-Bernoulli beam, can be written as:

$$EJ\frac{\partial^4 u}{\partial z^4} + [(\bar{P} + P_a \cos \omega t)A_{lum} - F_z]\frac{\partial^2 u}{\partial z^2} + \left(\rho_w A_w + \rho_f A_{lum}\right)\frac{\partial^2 u}{\partial t^2} = 0 \qquad (4.1)$$

in which $u$ is the transverse displacement of the central axis, $E$ is the wall incremental axial elastic Modulus, $J$ and $A_w$ are the second moment of inertia and cross sectional area of the wall, $P_a$ is the intraluminal pressure amplitude with angular frequency of $\omega$, $A_{lum}$ is the luminal area and $\rho_w$ and $\rho_f$ are the wall and fluid density. $F_z$ is the wall resultant axial force that is obtained by integrating the axial Cauchy stress $T_z$ over $A_w$.

Taking advantage of the theory of small deformations superimposed on large deformations (Baek et al., 2007), we assume that the wall geometry does not change due to blood pressure pulsation and all parameters are functions of $\bar{P}$ and $\lambda_z$ only. In order to find a solution for Equation 4.1, the method of weighted residuals (Ritz-Galerkin) was used. We assume a solution in the form of eigenfunction expansion:

$$y(z,\tau) = \sum_{n=1}^{N} f_n(\tau)\,\phi_n(z) \tag{4.2}$$

where $\phi_n(z)$ is a set of orthogonal eigenfunctions corresponding to eigenvalues $\gamma_n$ and satisfy the boundary conditions of the problem. By substituting Equation 4.2 in Equation 4.1, multiplying by $\phi_m$ and integrating from 0 to $l$, the stretched length of the aorta, we arrive at a set of ordinary differential equations for $f_n(t)$ which can be written in the matrix form as (Paidoussis & Issid, 1974)

$$\frac{d^2\boldsymbol{f}}{dt^2} + \frac{1}{\rho_w A_w + \rho_f A_{lum}} \{EJ\boldsymbol{\Lambda} + [(\bar{P} + P_a \cos\omega t)A_{lum} - F_z]\boldsymbol{C}\}\boldsymbol{f} = 0 \tag{4.3}$$

in which $\boldsymbol{f} = [f_1 \quad f_2 \quad ...]^T$, $\boldsymbol{\Lambda}$ is a diagonal matrix with $\Lambda_{nn} = {\gamma_n}^4$, and $\boldsymbol{C}$ is a matrix with elements $C_{mn} = \int_0^l (\phi_m \partial^2 \phi_n / \partial z^2) dz$.

**Case of pinned-pinned boundary condition (PPBC)**

For the case of PPBC

$$u(0) = 0, \qquad u(l) = 0, \qquad \left.\frac{\partial^2 u}{\partial z^2}\right|_{z=0} = 0, \qquad \left.\frac{\partial^2 u}{\partial z^2}\right|_{z=l} = 0 \tag{4.4}$$

we used

$$\phi_n(z) = \sin(\gamma_n z), \qquad \gamma_n = \frac{n\pi}{l}, \qquad n = 1, 2, 3 \,... \tag{4.5}$$

where n is the mode number (Figure 22-b). For this condition, matrix $\boldsymbol{C}$ becomes a diagonal matrix with $C_{nn} = -{\gamma_n}^2$ and the set of differential Equations 4.3 become decoupled. With some simplifications and introducing the dimensionless time $\tau = \omega t$, the Mathieu equation as presented in (Rachev, 2009) is obtained

$$\frac{d^2 f_n(\tau)}{d\tilde{t}^2} + [\delta_n - \varepsilon_n \cos\tau]\, f_n(\tilde{t}) = 0, \qquad n = 1, 2, \ldots$$

$${\omega_{n0}}^2 = \frac{E\,J}{\rho_w\, A_w + \rho_f\, A_{lum}} \frac{n^4\pi^4}{l^4}$$

$$\delta_n = \frac{{\omega_{n0}}^2}{\omega^2}\left[1 - \frac{l^2}{n^2\pi^2}\frac{\bar{P}\,A_{lum} - F_z}{E\,J}\right] \tag{(4.6)}$$

$$\varepsilon_n = \frac{{\omega_{n0}}^2}{\omega^2}\left[\frac{l^2}{n^2\pi^2}\frac{P_a\,A_{lum}}{E\,J}\right]$$

where $\omega_{n0}$ is the natural frequency of the aorta with the fluid inside and $\delta_n$ and $\varepsilon_n$ are dimensionless parameters that define the stability behavior of the Mathieu equation and are mainly representative of the mean pressure and pressure amplitude respectively.

### Case of clamped-clamped boundary condition (CCBC)

For this case, the boundary conditions are:

$$u(0) = 0, \qquad u(l) = 0, \qquad \left.\frac{\partial u}{\partial z}\right|_{z=0} = 0, \qquad \left.\frac{\partial u}{\partial z}\right|_{z=l} = 0 \tag{4.7}$$

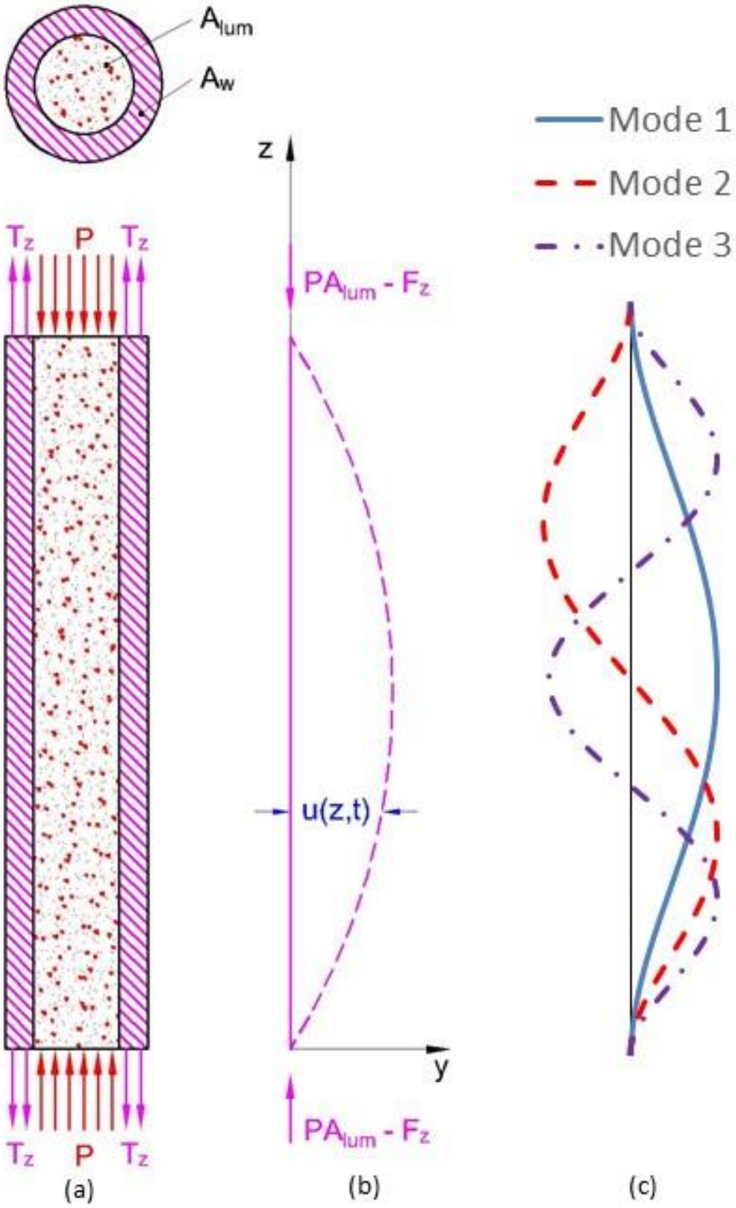
A_lum
A_w
T_z
P
T_z
T_z
P
T_z
(a)
z
PA_lum - F_z
u(z,t)
y
PA_lum - F_z
(b)
Mode 1
Mode 2
Mode 3
(c)

Figure 22– a) free body diagram of aortic segment. The aortic wall and intraluminal fluid is considered a composite beam. b) Configuration before and the first mode after loss of stability for pinned-pinned boundary condition. c) Three first mode shapes of clamped-clamped boundary condition used in this study.

To satisfy this boundary condition, the following eigenfunctions were chosen (Scott, 2001)

$$\phi_n(z) = \sigma_n[\sin(\gamma_n z) - \sinh(\gamma_n z)] + \cos(\gamma_n z) - \cosh(\gamma_n z)$$
$$\sigma_n = \frac{-\cos(\gamma_n l) + \cosh(\gamma_n l)}{\sin(\gamma_n l) - \sinh(\gamma_n l)}, \qquad \gamma_n = \frac{N_n}{l}, \qquad n = 1, 2, 3, \ldots \tag{4.8}$$

in which $N_n$ are the roots of $\cos x \cosh x = 1$ (Figure 22-c). For these eigenfunctions, $\boldsymbol{C}$ is not diagonal and we have (Paidoussis & Issid, 1974)

$$C_{mn} = \begin{cases} \gamma_m \sigma_m (2 - \gamma_m \sigma_m), & m = n \\ \dfrac{4{\gamma_m}^2{\gamma_n}^2}{{\gamma_m}^4 - {\gamma_n}^4} (\gamma_m \sigma_m - \gamma_n \sigma_n)((-1)^{m+n} + 1), & n \neq m \end{cases} \tag{4.9}$$

In analogy to Equation 4.6, we at a set of coupled Mathieu equations with parameters $\delta$ and $\varepsilon$ in the form of dimensionless matrices

$$\frac{d^2\boldsymbol{f}}{d\tau^2} + (\boldsymbol{\delta} + \boldsymbol{\varepsilon} \cos\tau)\boldsymbol{f} = 0$$
$$\boldsymbol{\delta} = \frac{1}{\omega^2} \frac{1}{\rho_w A_w + \rho_f A_{lum}} [EJ\boldsymbol{\Lambda} + (\bar{P} A_{lum} - F_z)\boldsymbol{C}\,] \tag{4.10}$$
$$\boldsymbol{\varepsilon} = \frac{1}{\omega^2} \frac{1}{\rho_w A_w + \rho_f A_{lum}} P_a A_{lum} \boldsymbol{C}$$

**Stability Analysis**

In order to find the stability regions of Mathieu equation, we used Bolotin's method of parametric resonance which states that the boundaries of stable and unstable region occur at solutions with periods of $2\pi$ and $4\pi$ (Bolotin, 1964; Jordan & Smith, 2007). These boundaries were found by assuming solutions in the form of

$$\boldsymbol{f}_{2\pi} = \sum_{-\infty}^{\infty} \boldsymbol{a}_k \exp(ik\tau), \quad \boldsymbol{f}_{4\pi} = \sum_{-\infty}^{\infty} \boldsymbol{b}_k \exp\left(\frac{1}{2} ik\tau\right) \qquad (4.11)$$

in which $\boldsymbol{a}_k$ and $\boldsymbol{b}_k$ are vectors of the coefficients for solutions with periods of $2\pi$ and $4\pi$ respectively. The Mathieu equations were simplified to a system of homogenous linear equations for $\boldsymbol{a}_k$ and $\boldsymbol{b}_k$ with the coefficient matrix being dependent on the geometry and loading parameters. The borders between the stable and unstable regions were determined numerically by setting the determinant of the coefficient matrix to zero. The upper and lower limits of the summations in Equations 4.11 were considered to be $-20$ and $20$ and it was verified that after about $k = \pm 15$ no significant change in the solution occurred.

For evaluation of the coefficient matrix, for a given mean intraluminal pressure and axial stretch ratio in the range of $\bar{P} = 0..70\ kPa$ (based on the estimated blood pressure during car accidents (Bass et al., 2001)) and $\lambda_z = 1.21..1.23$ ($\lambda_z = 1.22$ for equilibrium at physiological pressure), the geometric parameters $(A_w, A_{lum}, J)$ and $F_z$ were evaluated by considering the hyperelastic solution of the inflation-extension problem. Additionally, the incremental axial elastic Modulus $E$, as in (Rachev, 2009), was calculated by applying 1% axial strain superimposed on $\lambda_z$. Material densities were assumed to be $\rho_w = 1000 kg/m^3$ and $\rho_f = 1000\ kg/m^3$ . The pressure amplitude and frequency were varied in the range of $P_a = 0..5\ kPa$ and $f = \omega/2\pi = 0..5$ Hz.

Regarding the number of modes $(n)$ for Equations 6, since the modes are decoupled, the first mode $(n = 1)$ was the only physically relevant one to be considered (Rachev, 2009). The stability regions for this case were represented by a Strutt diagram with $\delta_n$ and $\varepsilon_n$ as the horizontal and vertical axes respectively. Using this diagram, any configuration of the aortic segment for a given $\lambda_Z$ and $\bar{P}$, can be represented by a point on the diagram and its stability be verified. The stability of aorta about a physiological reference point (PRP), given in Table 1, was investigated by changing $\bar{P}, P_a, f, L,$ and $\lambda_z$, independently.

For Equation 10, by increasing the mode numbers from 1, it was observed that after the third mode, the changes in the stability behavior were negligible and $n = 3$ was chosen for further stability analysis. In this case, stability was studied by comparing four diagrams including $P_a$, $f$, $L$, and $\lambda_z$ versus $\bar{P}$. For comparison, the same plots were also generated for the PPBC case.

Table 4– Average geometry, material parameters and physiological reference point used in this study for stability analysis. The physiological reference point is based on average *in vivo* values in the human aorta. . The initial length represents a segment of descending aorta between the arch and the first intercostal artery.

<table>
<tr><td colspan="7">Average Geometry</td></tr>
<tr><td colspan="2">Inner Radius (mm)</td><td colspan="3">Wall thickness (mm)</td><td colspan="2">Opening angle (deg)</td></tr>
<tr><td colspan="2">11.17</td><td colspan="3">2.44</td><td colspan="2">40.8</td></tr>
<tr><td colspan="7">Material Parameters</td></tr>
<tr><td>C (kPa)</td><td>$c_1$</td><td>$c_2$</td><td>$c_3$</td><td>$c_4$</td><td>$c_5$</td><td>$c_6$</td></tr>
<tr><td>61.35</td><td>0.6218</td><td>1.5277</td><td>1.0222</td><td>0.2103</td><td>0.1207</td><td>0.2971</td></tr>
<tr><td colspan="7">Physiological Reference Point</td></tr>
<tr><td>Mean</td><td>Pressure</td><td>Frequency (Hz)</td><td colspan="2">Initial</td><td colspan="2">Axial Stretch</td></tr>
<tr><td>13.3</td><td>2.7</td><td>1.3</td><td colspan="2">100</td><td colspan="2">1.22</td></tr>
</table>

## Results

The Strutt diagram for PPBC is shown in Figure 23 with gray areas representing the stable region. It can be seen that as a point moves in the $(\delta, \varepsilon)$ space to the left and top of the diagram, the probability of being in an unstable region is higher. The effects of variations in each parameter $\bar{P}, P_a, f, L,$ and $\lambda_z$, by keeping the others constant, are shown with two points that were above and below the PRP. It was noted that the PRP was in the stable region but close to its boundary. This made the segment prone to instability with relatively small changes in geometry and loading parameters. Increasing $\bar{P}$ and decreasing $\lambda_z$, moved the system toward the unstable region almost parallel to the $\delta$ axis. In contrast, increase in $P_a$, moved the system to the unstable region parallel to the $\varepsilon$ axis. Increase in $L$ and $f$ moved the system along oblique paths toward lower $\delta$ and $\varepsilon$ passing through multiple narrow stable/unstable regions. While longer $L$ eventually makes the system unstable, with higher $f$, the system could still be stable.

Since the equations for CCBC are coupled, unique dimensionless parameters cannot be defined to study the stability of the segment using a Strutt diagram. In order to demonstrate the stability regions, several graphs were generated (Figure 24) in which two parameters were varied while the others were kept constant at the PRP values. For the purpose of comparison, the corresponding graphs for PPBC are also shown. The left and right columns correspond to PPBC and CCBC respectively while rows correspond to $P_a, f, L$ or $\lambda_z$ in the vertical axis and $\bar{P}$ in the horizontal axis. As expected, the PRP, marked with a red cross, is farther away from the border with CCBC compared to PPBC, i.e., the aortic segment is more stable. Based on these graphs, the segment with PPBC could become unstable due to a small increase in $\bar{P}$ to 14 kPa. In contrast, the instability for the case of CCBC occurred at $\bar{P} \cong 40$ kPa and variations of the other parameters ($P_a, f, L$ or $\lambda_z$) about the PRP would not make the system unstable. For segments shorter than 90 mm, an increase in $\bar{P}$ up to 70 kPa did not induce instability (Figure 24-f). The critical mean static pressure, when $P_a = 0$ (Figure 24-a and Figure 24-b), was 18 and 47 kPa for PPBC and CCBC respectively.

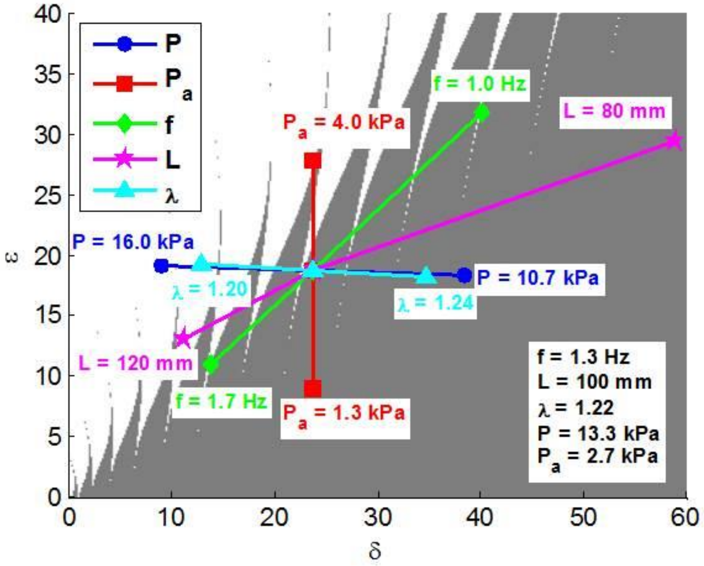

Figure 23 – Strutt diagram: Change of $\delta$ and $\varepsilon$ with mean blood pressure $\bar{P}$, pressure amplitude$P_a$, pulsation frequency $f$, initial length $L$ and axial stretch ratio $\lambda$.

To demonstrate how dynamic loading would result in a lower critical pressure, the stability of PRP ($P_a = 2.7$ kPa) and static loading ($P_a = 0$) as a result of increasing $\bar{P}$ were considered. The critical mean pressure decreased from 18 and 47 kPa to 14 and 40 kPa for PPBC and CCBC respectively. It should be noted that in the case of dynamic loading, $\bar{P} + P_a$ is still less than static critical pressure. This result showed the arteries under dynamic loading may lose their stability at pressures lower than static critical pressure.

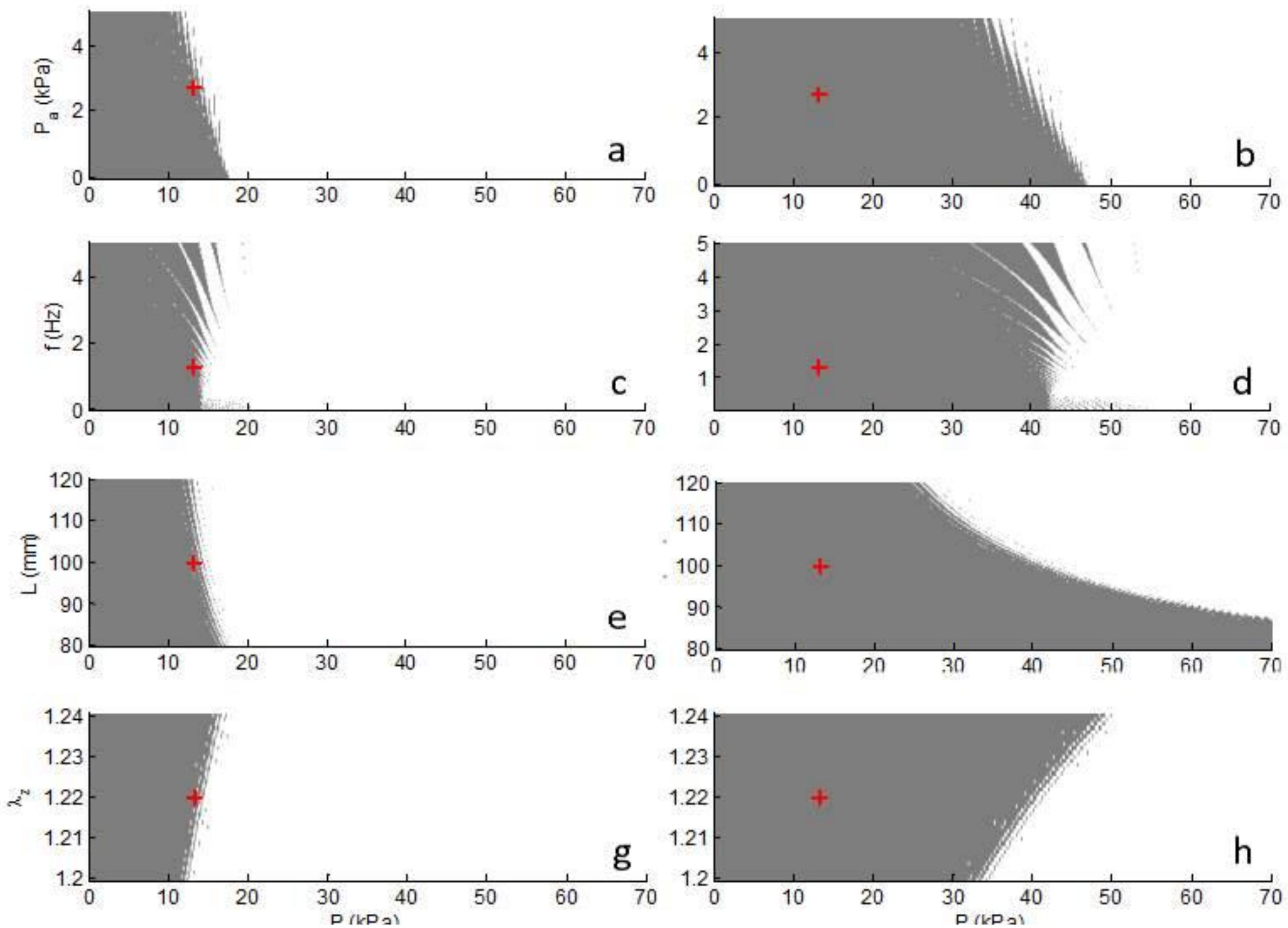

Figure 24– Stability region (gray area) for PPBC (left column) and CCBC (right column) plotted with mean pressure as the horizontal axis. The vertical axes are: a & b) pressure amplitude, c & d) blood pulsation frequency, e & f) initial segment length, and g & h) axial stretch ratio. The physiological reference point, as explained in the text, is shown with the red cross.

## Discussion

In order to demonstrate the stability behavior of the PPBC by use of the Strutt diagram, $L, \lambda, \bar{P}, P_a$ and $f$ were changed in the vicinity of PRP. The selected ranges were based on the clinical data as explained below. The American Heart Association recommends a blood pressure range of 120/80 mmHg as the optimal blood pressure (Chobanian et al., 2003). These values correspond to 100 mmHg (13.3 kPa) mean pressure and 20 mmHg (2.7 kPa) pressure amplitude (PRP state). $\bar{P}$ was varied between 80 and 120 mmHg (10.7 and 16 kPa) that correspond approximately to the beginning of hypotensive and hypertensive blood pressures respectively. Similarly, $P_a$ was changed between 1.3 and 4.0 kPa to reach the hypotensive and hypertensive limits. Healthy heart beat for adults at rest is considered to be between 60 and 100 beats per minute (bpm) and values below or beyond that are considered bradycardia and tachycardia (American Heart Association Guidelines, 2005). These limit values and the mean value of 80 bpm were chosen to determine the range of $f$ (1.3 $\pm$ 0.3 Hz). The assumed segment lengths ($L = 100 \pm 20$ mm) correspond to an estimation of the length of aorta, which is relatively free to move; between the arch and the tethered part of the descending aorta (Richens et al., 2002; Shimizu et al., 2005; Symbas, 1977). The PRP value reported in the diagram for $\lambda_z$ is 1.22 which is obtained from our inflation experiments at $\bar{P} = 13.3\ kPa$. The range of $\lambda_z$ was determined by the difference between this value and the in-situ axial stretch ratio of 1.2 reported for human aorta (Holzapfel et al., 2007).

TAR in experimental studies on cadavers occur at a lower rate compared to real world accidents (Hardy et al., 2008; Viano, 2011) which might be due to the altered configuration of the aorta in the chest cavity such as increase in axial stretch ratio as a result of dropping of the diaphragm. Aortic pressure inside the aorta during car accidents can reach to an average of 70 kPa (Bass et al., 2001; Hardy et al., 2008) which, as shown in this study, can induce mechanical instabilities. We have also shown that the state of instability is very sensitive to the axial stretch ratio and the vessel becomes more stable with an increased tension. This suggests that one of the reasons for unsuccessful replication of TAR in cadaver tests might be that the aorta is more mechanically stable.

Although the critical pressures for CCBC are in supra-physiological range, we should note that these pressures are possible in traumatic scenarios such as car accidents as mentioned above. The mechanical instabilities of aorta during an accident, accompany an increase in tissue stress and strain, which as stated earlier, can be a contributing factor to injury and rupture. To illustrate this point, changes in stress and strain in the tissue due to bending were evaluated for the two cases of PPBC and CCBC (Figure 25). For this purpose, the critical pressures were determined to be $18$ and $47\ kPa$ respectively for PPBC and CCBC (corresponding to $P_a = 0$). In calculating the stretch ratios in the bent configuration, we used the kinematic equations of bending and superimposed the calculated strains on the axial stretch ratio of PRP (1.22). The tissue incremental axial elastic Modulus was also calculated for the case of the axial extension of a cylindrical segment under constant pressure and was used to find the level of stress. A 20 mm deflection at the midpoint of the aortic segment showed approximately a 4 fold increase in stress. Although the maximum stress levels are lower than the failure initiation level of 800 kPa (Stemper et al., 2007), this increase shows that mechanical instabilities can be a significant contributing factor in increasing the stress to the injury and failure levels.

It was shown that the type of boundary condition played an important role in the vessel stability behavior. With PPBC the PRP is prone to instability while with CCBC the vessel is more stable and instabilities are possible only in supra-physiological pressures. While the mechanical nature of perivascular tissue and how aorta is supported in the body is not completely known (Rachev, 2009; Taylor & Humphrey, 2009), it is believed that one simple boundary condition may not be sufficient and that the boundary at one end may change from a pinned condition at small deformations to a clamped conditions at larger deformations. Therefore, we expect the stability region in real aorta to be between the regions obtained for PPBC and CCBC, i.e. the vessel is more stable than PPBC and more prone to instabilities compared to CCBC.

To demonstrate how dynamic loading would result in a lower critical pressure, the stability of PRP ($P_a = 2.7$ kPa) and static loading ($P_a = 0$) as a result of increasing $\bar{P}$ were considered. The critical mean pressure decreased from 18 and 47 kPa to 14 and 40 kPa for PPBC and CCBC respectively. It should be noted that in the case of dynamic loading, $\bar{P} + P_a$ is still less than static critical pressure. This result showed the arteries under dynamic loading may lose their stability at pressures lower than static critical pressure.

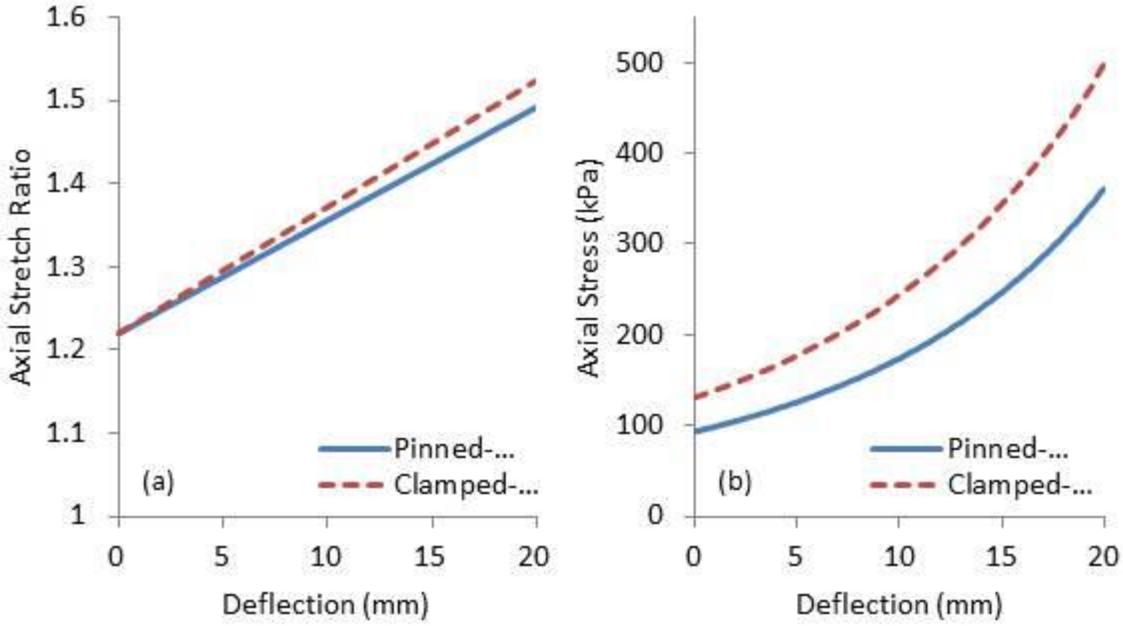

Figure 25 – Change in axial stretch ratio and average axial stress in a 100 mm segment of aorta after deflection. Pinned-pinned and clamped-clamped cases were studied at their corresponding static buckling pressure of 18 and 47 kPa respectively.

The material model used for the simulations in this study, is derived from quasi-static inflation-extension experiments and therefore may be inaccurate for high rate applications such as car accidents. Assuming that the rate dependence of aorta can be modeled by a quasi-linear viscoelastic model, for higher rate the material will behave as a stiffer material. In order to obtain a more accurate estimate of the instantaneous elastic response, parameter $c$ in the current model can be scaled up by the amount of relaxation of the tissue (Fung, 1993). Based another study by our group on porcine aorta, it was assumed that $c = 170.42\ \mathrm{kPa}$ (Hemmasizadeh at al., 2012a). In the first 100 ms of loading, that corresponds to the time range of car accidents, this value reduces by about 30% to 119.29 kPa. It was found that this range of $c$ predominantly changed δ and the change in ε was negligible. Higher values of $c$ resulted in higher values of δ and critical pressures. The instantaneous critical pressure was found to be 44.6 and 123.4 kPa for PPBC and CCBC respectively which were reduced to 21.7 and 61.8 kPa within the first 100 ms. Therefore, under the average peak pressure of 70 kPa that occurs in car accidents, our model predicts that aorta would become mechanically unstable.

As a limitation of this study, the material behavior of the aortic tissue was simulated by a phenomenological constitutive model. Recent advancements in multi-scale models for arteries such as fiber-reinforced models (Gasser, Ogden, & Holzapfel, 2006) and mixture models (Humphrey & Rajagopal, 2003) can be incorporated to study the role of arterial tissue fibers in the stability of blood vessels. Moreover, in the radial direction, the aortic wall consisted of three layers and in the axial direction its stiffness changes for about 20% in a 100 mm segment (Sokolis, 2007). Understanding the effect of inhomogeneity on the stability of aorta was beyond the scope of this study and would require further investigation.

# CHAPTER 5

# CONCLUDING REMARKS

While the use of restraint systems has increased in recent years, the overall incidence of TAI/TAR in car accidents has remained the same and airbags and seatbelts did not eliminate the risk of injury. This emphasizes the necessity of more comprehensive studies on the underlying mechanisms of aortic injuries in order to improve the effectiveness of the safety systems. The results presented in this dissertation provide a step forward in our understanding of the mechanical and failure behavior of aorta and the mechanisms that lead to TAI/TAR.

In this study, the inflation-extension test method was extended to supra-physiological intraluminal pressures (70 kPa) that occur in aorta during car accidents. Using a fixed-free boundary condition, sample buckling was avoided. With this boundary condition, it was found that $\lambda_\theta(r_o)$ was slightly smaller than $\lambda_z$ which indicated an orthotropic material behavior and that the tissue was stiffer in the $\theta$ direction. The nonlinear rising trend of $\lambda_\theta$ from outer toward inner wall was significantly increased at higher pressures. The increase in $\lambda_\theta$ in the pressure range of 13 kPa to 70 kPa was 13% at the outer wall and 22% at the inner wall while in this pressure range, $\lambda_z$ increased 20%.

It was shown that an orthotropic Fung-type SEDF that was previously used in the physiological inflation-extension tests, could satisfactorily describe the material behavior of the segments from 0 to 70 kPa. A significant nonlinearity in the material behavior was observed as in this pressure range, stresses $T_\theta(r_i)$ and $T_z(r_i)$ were increased 16 and 18 times respectively for less 3 fold increase in strains. A novel and computationally efficient method was implemented to ensure the convexity of the SEDF. The applicability of the overall constitutive model in multi-axial loading conditions was verified in several loading paths in the $\lambda_z - \lambda_\theta$ space.

The deformation of aorta in car accidents occur at high rates and therefore, it was necessary to characterize the rate dependence of the mechanical and failure properties of the tissue. Obtaining failure properties of the tissue from inflation-extension experiments was not practical due to the failure of sutures at branches during pressurization. With a multirate uniaxial test setup that was developed for this study, aorta samples were tested in circumferential and longitudinal directions at strain rates up to 400 $s^{-1}$ which is an order of magnitude higher than previously published data. Two distinct states of failure initiation (FI) and ultimate tensile strength (UTS) were identified in both directions. Explicit direct relationships were derived between FI and UTS stresses and strain rate. On the other hand, FI and UTS strains were rate independent and therefore strain was proposed as the main mechanism of failure. The average strain at the ultimate tensile strength from both direction and at all rates was 0.89±0.03. Tissue pre-failure linear moduli showed an average of 60% increase over the range of strain rates.

Using the constitutive model that has been developed in this study, the mechanical instability of aorta was studied. Since arteries are under dynamic loading, their mechanical instabilities need to be analyzed by dynamic methods. It was shown that aorta may become unstable in pressures lower than what is predicted by the static buckling theory. It was shown that the type of boundary condition had a significant effect on the stability behavior.

For example, the critical pressure for CCBC was approximately three times higher than PPBC. The values of critical pressures remained below the average peak intraluminal pressures in car accidents, and based on that, mechanical instability was proposed as a contributing factor to TAI/TAR.

Both inflation-extension and uniaxial experiments results showed a prominent anisotropy in which the circumferential direction was about four times stiffer than the longitudinal direction. This anisotropy can be attributed to the direction of collagen fibers which are dominantly aligned in the circumferential direction (Holzapfel, 2000). The aortic tissue also showed a higher failure stress and failure strain in the circumferential direction which explains why most of the aortic ruptures in car accidents occur in the longitudinal direction (Richens & Kotidis, 2003).

Injuries of aorta initiate from the intimal layer and propagate toward the media and the adventitia (Neschis et al., 2008). This mechanism could be explained partly by the results of this study. Based on the failures observed in the uniaxial experiments, it was concluded that the failure initiation occurred on the intimal side. A similar observation has been reported by others (Stemper et al., 2007) who recorded videos of tissue loading from both the intimal and the adventitial sides. Therefore, it could be concluded that the intimal layer had lower failure strains/stresses compared to the other two layers. Moreover, based on the inflation extension experiments, strains and stresses in the aortic wall were higher in the inner wall region, which could contribute to the initiation of failure from intima.

## Suggestions for future research projects

- The multirate uniaxial experimental data can be utilized for characterization of a viscoelastic model of aorta. The constitutive model that has been developed in this study can be considered the steady state response of the tissue. A viscoelastic model can be characterized to describe all the results of uniaxial extension experiments. Initial work toward this end showed that viscoelasticity is also anisotropic, which makes the model characterization a challenge.
- Determination of the tissue mechanical and failure properties can be extended to the properties of its constituents, i.e., collagen fibers and elastin, to gain more insight into the mechanisms of tissue deformation and failure. This can be achieved by dissolving elastin or collagen in the specimens. While some preliminary work has been done in this regard, this area of research is still in its infancy (M. J. Collins, Eberth, Wilson, & Humphrey, 2012).
- Utilizing advanced tissue imaging techniques in conjunction with mechanical testing can shed light on the failure mechanisms at micro-structural level. For example, a confocal microscope can be utilized for visualization of collagen fibers using fluorescent markers such as CNA35-OG488 (Rezakhaniha et al., 2012).
- The current study on the mechanical instability of aorta shows that buckling can be a contributing factor in TAI. Further studies on the effect of

surrounding tissue are necessary to model the stability behavior of aorta *in vivo*. Transient loading, as it occurs in car accidents, may be implemented in the buckling formulations to obtain better estimates of the critical pressures.

# BIBLIOGRAPHY

American Heart Association Guidelines for Cardiopulmonary Resuscitation and Emergency Cardiovascular Care: Part 7.3: Management of Symptomatic Bradycardia and Tachycardia. (2005). In *Circulation* (Vol. 112, pp. IV–67–IV–77). doi:10.1161/CIRCULATIONAHA.105.166558

Azizzadeh, A., Valdes, J., Miller, C. C., Nguyen, L. L., Estrera, A. L., Charlton-Ouw, K., … Safi, H. J. (2011). The utility of intravascular ultrasound compared to angiography in the diagnosis of blunt traumatic aortic injury. *Journal of Vascular Surgery*, *53*(3), 608–14. doi:10.1016/j.jvs.2010.09.059

Baek, S., Gleason, R. L., Rajagopal, K. R., & Humphrey, J. D. (2007). Theory of small on large: Potential utility in computations of fluid-solid interactions in arteries. *Computer Methods in Applied Mechanics and Engineering*, *196*(31-32), 3070–3078. doi:10.1016/j.cma.2006.06.018

Bass, C., Darvish, K., Bush, B., Crandall, J. R., Srinivasan, S. C. M., Tribble, C., … Wang, C. (2001). Material properties for modeling traumatic aortic rupture. *SAE Paper 2001-220006*, *45*(November). Retrieved from http://papers.sae.org/2001-22-0006/

Bertrand, S., Cuny, S., Petit, P., Trosseille, X., Page, Y., Guillemot, H., & Drazetic, P. (2008). Traumatic rupture of thoracic aorta in real-world motor vehicle crashes. *Traffic Injury Prevention*, *9*(2), 153–161. doi:10.1080/15389580701775777

Bolotin, V. V. (1964). *The Dynamic Stability of Elastic Systems* (1st ed.). Holden-Day.

Carpenter, J. P., Baum, R. a, Barker, C. F., Golden, M. a, Mitchell, M. E., Velazquez, O. C., & Fairman, R. M. (2001). Impact of exclusion criteria on patient selection for endovascular abdominal aortic aneurysm repair. *Journal of Vascular Surgery*, *34*(6), 1050–1054. doi:10.1067/mva.2001.120037

Castaneda-zunlga, W. R., Vlodaver, Z., Tadavarthy, M., Edwards, J. E., Zollikofer, C., & Amplatz, K. (1980). The mechanism of balloon angioplasty. *Radiology*, *135*(3), 565–571.

Chesnutt, J. K. W., & Han, H. C. (2011). Tortuosity triggers platelet activation and thrombus formation in microvessels. *Journal of Biomechanical Engineering*, *133*(12), 121004. doi:10.1115/1.4005478

Chobanian, A. V., Bakris, G. L., Black, H. R., Cushman, W. C., Green, L. a., Izzo, J. L., … Roccella, E. J. (2003). Seventh report of the Joint National Committee on Prevention, Detection, Evaluation, and Treatment of High Blood Pressure. *Hypertension*, *42*, 1206–1252. doi:10.1161/01.HYP.0000107251.49515.c2

Chuong, C. J., & Fung, Y. C. (1983). Three-dimensional stress distribution in arteries. *Journal of Biomechanical Engineering*, *105*(3), 268–274. Retrieved from http://www.ncbi.nlm.nih.gov/pubmed/6632830

Chuong, C. J., & Fung, Y. C. (1986). On residual stresses in arteries. *Journal of Biomechanical Engineering*. Retrieved from http://link.aip.org/link/?JBENDY/108/189/1

Collins, M. J., Eberth, J. F., Wilson, E., & Humphrey, J. D. (2012). Acute mechanical effects of elastase on the infrarenal mouse aorta: implications for models of aneurysms. *Journal of Biomechanics*, *45*(4), 660–5. doi:10.1016/j.jbiomech.2011.12.013

Collins, R., & Hu, W. (1972). Dynamic deformation experiments on aortic tissue. *Journal of Biomechanics*, *5*, 333–337. Retrieved from http://www.sciencedirect.com/science/article/pii/0021929072900620

Criado, F. J., Clark, N. S., & Barnatan, M. F. (2002). Stent graft repair in the aortic arch and descending thoracic aorta: a 4-year experience. *Journal of Vascular Surgery : Official Publication, the Society for Vascular Surgery [and] International Society for Cardiovascular Surgery, North American Chapter*, *36*(6), 1121–1128. doi:10.1067/mva.2002.129649

Derubertis, B. G., Hynecek, R. L., Kent, K. C., & Faries, P. L. (2011). Carotid tortuosity in patients with prior cervical radiation: increased technical challenge during carotid stenting. *Vascular and Endovascular Surgery*, *45*(7), 619–26. doi:10.1177/1538574411408745

Federico, S., Grillo, A., Giaquinta, G., & Herzog, W. (2007). Convex Fung-type potentials for biological tissues. *Meccanica*, *43*(3), 279–288. doi:10.1007/s11012-007-9090-6

Ferris, B. L., Taylor, L. M., Oyama, K., McLafferty, R. B., Edwards, J. M., Moneta, G. L., & Porter, J. M. (2000). Hypothenar hammer syndrome: proposed etiology. *Journal of Vascular Surgery*, *31*(1 Pt 1), 104–13. Retrieved from http://www.ncbi.nlm.nih.gov/pubmed/10642713

Ferruzzi, J., Vorp, D. a, & Humphrey, J. D. (2011). On constitutive descriptors of the biaxial mechanical behaviour of human abdominal aorta and aneurysms. *Journal of* *the Royal Society, Interface / the Royal Society, 8*(56), 435–50. doi:10.1098/rsif.2010.0299

Fillinger, M. F., Racusin, J., Baker, R. K., Cronenwett, J. L., Teutelink, A., Schermerhorn, M. L., … Rzucidlo, E. M. (2004). Anatomic characteristics of ruptured abdominal aortic aneurysm on conventional CT scans: Implications for rupture risk. *Journal of Vascular Surgery : Official Publication, the Society for Vascular Surgery [and] International Society for Cardiovascular Surgery, North American Chapter, 39*(6), 1243–52. doi:10.1016/j.jvs.2004.02.025

Friedman, M. H., Deters, O. J., Mark, F. F., Bargeron, C. B., & Hutchins, G. M. (1983). Arterial geometry affects hemodynamics A potential risk factor for atherosclerosis. *Atherosclerosis, 46*(2), 225–231. doi:10.1016/0021-9150(83)90113-2

Fung, Y. C. (1993). *Biomechanics: Mechanical Properties of Living Tissues* (2nd ed.). NewYork: Springer.

Fung, Y. C., Fronek, K., & Patitucci, P. (1979). Pseudoelasticity of arteries and of its mathematical expression. *American Journal of Physiology-Heart and Circulatory Physiology, 237*(5), H620–H631. Retrieved from http://ajpheart.physiology.org/content/ajpheart/237/5/H620.full.pdf

Fung, Y., Fronek, K., & Patitucci, P. (1979). Pseudoelasticity of arteries and the choice of its mathematical expression. *American Journal of Physiology-Heart and Circulatory Physiology, 237*(5), H620.

García, A., Peña, E., Laborda, A., Lostalé, F., De Gregorio, M. A., Doblaré, M., & Martínez, M. A. (2011). Experimental study and constitutive modelling of the passive mechanical properties of the porcine carotid artery and its relation to histological analysis: Implications in animal cardiovascular device trials. *Medical Engineering & Physics, 33*(6), 665–76. doi:10.1016/j.medengphy.2011.01.016

Gasser, T. C., Ogden, R. W., & Holzapfel, G. A. (2006). Hyperelastic modelling of arterial layers with distributed collagen fibre orientations. *Journal of the Royal Society, Interface / the Royal Society, 3*(6), 15–35. doi:10.1098/rsif.2005.0073

Greenwald, S. E. (2007). Ageing of the conduit arteries. *Journal of Pathology*. doi:10.1002/path.2101

Gundiah, N., Matthews, P. B., Karimi, R., Azadani, A., Guccione, J., Guy, T. S., … Tseng, E. E. (2008). Significant material property differences between the porcine ascending aorta and aortic sinuses. *The Journal of Heart Valve Disease, 17*(6), 606–613. Retrieved from http://www.ncbi.nlm.nih.gov/pubmed/19137790

Guo, X., & Kassab, G. S. (2004). Distribution of stress and strain along the porcine aorta and coronary arterial tree. *American Journal of Physiology. Heart and Circulatory Physiology*, *286*(6), H2361–8. doi:10.1152/ajpheart.01079.2003

Han, H. C. (2007). A biomechanical model of artery buckling. *Journal of Biomechanics*, *40*(16), 3672–8. doi:10.1016/j.jbiomech.2007.06.018

Han, H. C. (2008). Nonlinear buckling of blood vessels: a theoretical study. *Journal of Biomechanics*, *41*(12), 2708–13. doi:10.1016/j.jbiomech.2008.06.012

Han, H. C. (2009a). Blood vessel buckling within soft surrounding tissue generates tortuosity. *Journal of Biomechanics*, *42*(16), 2797–801. doi:10.1016/j.jbiomech.2009.07.033

Han, H. C. (2009b). The mechanical buckling of curved arteries. *Molecular & Cellular Biomechanics : MCB*, *6*(2), 93–9. Retrieved from http://www.ncbi.nlm.nih.gov/pubmed/19496257

Han, H. C. (2009c). The theoretical foundation for artery buckling under internal pressure. *Journal of Biomechanical Engineering*, *131*(12), 124501. doi:10.1115/1.4000080

Han, H. C., & Fung, Y. C. (1996). Direct measurement of transverse residual strains in aorta. *The American Journal of Physiology*, *270*(2 Pt 2), H750–9. Retrieved from http://www.ncbi.nlm.nih.gov/pubmed/8779853

Hardy, W. N., Shah, C. S., Mason, M. J., Kopacz, J. M., Yang, K. H., King, A. I., … Digges, K. H. (2008). Mechanisms of traumatic rupture of the aorta and associated peri-isthmic motion and deformation. *Stapp Car Crash Journal*, *52*(November), 233–265. Retrieved from http://www.ncbi.nlm.nih.gov/pubmed/19085165

Hedrick, T. (2008). Software techniques for two-and three-dimensional kinematic measurements of biological and biomimetic systems. *Bioinspiration & Biomimetics*, *3*(3), 034001. doi:10.1088/1748-3182/3/3/034001

Hemmasizadeh, A., Darvish, K., & Autieri, M. (2012a). Characterization of changes to the mechanical properties of arteries due to cold storage using nanoindentation tests. *Annals of Biomedical Engineering*, *40*(7), 1434–42. doi:10.1007/s10439-011-0506-z

Hemmasizadeh, A., Darvish, K., & Autieri, M. (2012b). Multilayer material properties of aorta determined from nanoindentation tests. *Annals of Biomedical Engineering*, *40*(7), 1434–42. doi:10.1007/s10439-011-0506-z

Hiroki, M., Miyashita, K., & Oda, M. (2002). Tortuosity of the white matter medullary arterioles is related to the severity of hypertension. *Cerebrovascular Diseases*, *13*, 242–250. doi:10.1159/000057850

Holzapfel, G. A. (2000). *Nonlinear Solid Mechanics: A Continuum Approach for Engineering*. Chichester: Wiley. Retrieved from http://tocs.ulb.tu-darmstadt.de/182986683.pdf

Holzapfel, G. A. (2006). Determination of material models for arterial walls from uniaxial extension tests and histological structure. *Journal of Theoretical Biology*, *238*(2), 290–302. doi:10.1016/j.jtbi.2005.05.006

Holzapfel, G. A., & Gasser, T. C. (2007). Computational stress-deformation analysis of arterial walls including high-pressure response. *International Journal of Cardiology*, *116*(1), 78–85. doi:10.1016/j.ijcard.2006.03.033

Holzapfel, G. A., Gasser, T., & Ogden, R. (2000). A new constitutive framework for arterial wall mechanics and a comparative study of material models. *Journal of Elasticity and the Physical Science of Solids*, 1–48. Retrieved from http://link.springer.com/article/10.1023/A:1010835316564

Holzapfel, G. A., & Ogden, R. (2010). Constitutive modelling of arteries. *Proceedings of the Royal Society A: Mathematical, Physical and Engineering Sciences*, *466*(2118), 1551–1597. Retrieved from http://rspa.royalsocietypublishing.org/content/466/2118/1551.short

Holzapfel, G. A., & Ogden, R. W. (2008). On planar biaxial tests for anisotropic nonlinearly elastic solids. A continuum mechanical framework. *Mathematics and Mechanics of Solids*, *14*(5), 474–489. doi:10.1177/1081286507084411

Holzapfel, G. A., & Ogden, R. W. (2009). Constitutive modelling of passive myocardium: a structurally based framework for material characterization. *Philosophical Transactions. Series A, Mathematical, Physical, and Engineering Sciences*, *367*(1902), 3445–75. doi:10.1098/rsta.2009.0091

Holzapfel, G. A., Sommer, G., Auer, M., Regitnig, P., & Ogden, R. W. (2007). Layer-specific 3D residual deformations of human aortas with non-atherosclerotic intimal thickening. *Annals of Biomedical Engineering*, *35*(4), 530–545. doi:10.1007/s10439-006-9252-z

Holzapfel, G. A., Stadler, M., & Gasser, T. C. (2005). Changes in the mechanical environment of stenotic arteries during interaction with stents: computational assessment of parametric stent designs. *Journal of Biomechanical Engineering*, *127*(1), 166–180. doi:10.1115/1.1835362

Holzapfel, G. A., Stadler, M., & Schulze-Bauer, C. a. J. (2002). A layer-specific three-dimensional model for the simulation of balloon angioplasty using magnetic resonance imaging and mechanical testing. *Annals of Biomedical Engineering*, *30*(6), 753–767. doi:10.1114/1.1492812

Humphrey, J. D. (2002). *Cardiovascular solid mechanics: cells, tissues, and organs* (1st ed.). Springer. Retrieved from http://books.google.com/books?hl=en&lr=&id=DBglTvXRtGcC&oi=fnd&pg=PR7&dq=Cardiovascular+solid+mechanics:+cells,+tissues,+and+organs&ots=bzub1OeALH&sig=H3AoDYM_OdZ4GNg6_7M5tT9tRes

Humphrey, J. D., Kang, T., Sakarda, P., & Anjanappa, M. (1993). Computer-aided vascular experimentation: a new electromechanical test system. *Annals of Biomedical Engineering*, *21*(1), 33–43. Retrieved from http://www.ncbi.nlm.nih.gov/pubmed/8434818

Humphrey, J. D., & Rajagopal, K. R. (2003). A constrained mixture model for arterial adaptations to a sustained step change in blood flow. *Biomechanics and Modeling in Mechanobiology*, *2*(2), 109–26. doi:10.1007/s10237-003-0033-4

Jackson, Z. S., Dajnowiec, D., Gotlieb, A. I., & Langille, B. L. (2005). Partial off-loading of longitudinal tension induces arterial tortuosity. *Arteriosclerosis, Thrombosis, and Vascular Biology*, *25*(5), 957–62. doi:10.1161/01.ATV.0000161277.46464.11

Jordan, D., & Smith, P. (2007). *Nonlinear Ordinary Differential Equations: An Introduction for Scientists and Engineers* (4th ed.). Oxford University Press.

Kim, J., & Baek, S. (2011). Circumferential variations of mechanical behavior of the porcine thoracic aorta during the inflation test. *Journal of Biomechanics*, *44*(10), 1941–1947. doi:10.1016/j.jbiomech.2011.04.022

Labrosse, M. R., Beller, C. J., Mesana, T., & Veinot, J. P. (2009). Mechanical behavior of human aortas: Experiments, material constants and 3-D finite element modeling including residual stress. *Journal of Biomechanics*, *42*(8), 996–1004. doi:10.1016/j.jbiomech.2009.02.009

Labrosse, M. R., Gerson, E. R., Veinot, J. P., & Beller, C. J. (2013). Mechanical characterization of human aortas from pressurization testing and a paradigm shift for circumferential residual stress. *Journal of the Mechanical Behavior of Biomedical Materials*, *17*, 44–55. doi:10.1016/j.jmbbm.2012.08.004

Laksari, K., Shafieian, M., & Darvish, K. (2012). Constitutive model for brain tissue under finite compression. *Journal of Biomechanics*, *45*(4), 642–646. doi:10.1016/j.jbiomech.2011.12.023

Lee, W. A., Matsumura, J. S., Mitchell, R. S., Farber, M. a, Greenberg, R. K., Azizzadeh, A., … Fairman, R. M. (2011). Endovascular repair of traumatic thoracic aortic injury: clinical practice guidelines of the Society for Vascular Surgery. *Journal of Vascular Surgery*, *53*(1), 187–92. doi:10.1016/j.jvs.2010.08.027

Li, Y., Shen, C., Ji, Y., Feng, Y., Ma, G., & Liu, N. (2011). Clinical implication of coronary tortuosity in patients with coronary artery disease. *PloS One*, *6*(8), e24232. doi:10.1371/journal.pone.0024232

Lillie, M. A., Armstrong, T. E., Gérard, S. G., Shadwick, R. E., & Gosline, J. M. (2012). Contribution of elastin and collagen to the inflation response of the pig thoracic aorta: assessing elastin's role in mechanical homeostasis. *Journal of Biomechanics*, *45*(12), 2133–41. doi:10.1016/j.jbiomech.2012.05.034

Lillie, M. A., Shadwick, R. E., & Gosline, J. M. (2010). Mechanical anisotropy of inflated elastic tissue from the pig aorta. *Journal of Biomechanics*, *43*(11), 2070–2078. doi:10.1016/j.jbiomech.2010.04.014

Liu, Q., & Han, H. C. (2012). Mechanical buckling of artery under pulsatile pressure. *Journal of Biomechanics*, *45*(7), 1192–1198. doi:10.1016/j.jbiomech.2012.01.035

Lo, T. S., Nolan, J., Fountzopoulos, E., Behan, M., Butler, R., Hetherington, S. L., … Hildick-Smith, D. (2009). Radial artery anomaly and its influence on transradial coronary procedural outcome. *Heart (British Cardiac Society)*, *95*(5), 410–5. doi:10.1136/hrt.2008.150474

Malvè, M., Gharib, a. M., Yazdani, S. K., Finet, G., Martínez, M. a., Pettigrew, R., & Ohayon, J. (2014). Tortuosity of Coronary Bifurcation as a Potential Local Risk Factor for Atherosclerosis: CFD Steady State Study Based on *in vivo* Dynamic CT Measurements. *Annals of Biomedical Engineering*, *43*(1), 82–93. doi:10.1007/s10439-014-1056-y

Marra, S. P., Kennedy, F. E., Kinkaid, J. N., & Fillinger, M. F. (2006). Elastic and rupture properties of porcine aortic tissue measured using inflation testing. *Cardiovascular Engineering (Dordrecht, Netherlands)*, *6*(4), 123–131. doi:10.1007/s10558-006-9021-5

Matsumoto, T., Goto, T., Furukawa, T., & Sato, M. (2004). Residual stress and strain in the lamellar unit of the porcine aorta: experiment and analysis. *Journal of Biomechanics*, *37*(6), 807–815. doi:10.1016/j.jbiomech.2003.08.014

Misra, J. C., & Singh, S. I. (1985). A model for studying the stability of thoracic aorta. *Mathematical Modelling*, *6*(4), 295–306. doi:10.1016/0270-0255(85)90031-4

Misra, J., & Choudhury, K. (1982). A study on the stability of blood vessels. *Rheologica Acta*, *346*, 340–346. Retrieved from http://link.springer.com/article/10.1007/BF01515722

Mohan, D., & Melvin, J. (1982). Failure properties of passive human aortic tissue. I—uniaxial tension tests. *Journal of Biomechanics*, *15*(11), 887–893. Retrieved from http://www.sciencedirect.com/science/article/pii/0021929082900550

Mohan, D., & Melvin, J. (1983). Failure properties of passive human aortic tissue. II—biaxial tension tests. *Journal of Biomechanics*, *16*(1), 31–44. Retrieved from http://www.sciencedirect.com/science/article/pii/0021929083900441

Moody, D. M., Brown, W. R., Challa, V. R., Ghazi-Birry, H. S., & Reboussin, D. M. (1997). Cerebral Microvascular Alterations in Aging, Leukoaraiosis, and Alzheimer's Diseasea. *Annals of the New York Academy of Sciences*, *826*(1), 103–116.

Neschis, D. G., Scalea, T. M., Flinn, W. R., & Griffith, B. P. (2008). Blunt aortic injury. *The New England Journal of Medicine*, *359*(16), 1708–16. doi:10.1056/NEJMra0706159

Paidoussis, M., & Issid, N. (1974). Dynamic stability of pipes conveying fluid. *Journal of Sound and Vibration*, *33*, 267–294. Retrieved from http://www.sciencedirect.com/science/article/pii/S0022460X74800027

Pancera, P., Ribul, M., Presciuttini, B., & Lechi, a. (2000). Prevalence of carotid artery kinking in 590 consecutive subjects evaluated by Echocolordoppler. Is there a correlation with arterial hypertension? *Journal of Internal Medicine*, *248*, 7–12. doi:10.1046/j.1365-2796.2000.00611.x

Pearson, R., Philips, N., Hancock, R., Hashim, S., Field, M., Richens, D., & McNally, D. (2008). Regional wall mechanics and blunt traumatic aortic rupture at the isthmus. *European Journal of Cardio-Thoracic Surgery : Official Journal of the European Association for Cardio-Thoracic Surgery*, *34*(3), 616–622. doi:10.1016/j.ejcts.2008.03.069

Prendergast, P. J., Lally, C., Daly, S., Reid, a. J., Lee, T. C., Quinn, D., & Dolan, F. (2003). Analysis of prolapse in cardiovascular stents: a constitutive equation for vascular tissue and finite-element modelling. *Journal of Biomechanical Engineering*, *125*(5), 692–699. doi:10.1115/1.1613674

Rachev, A. (2009). A theoretical study of mechanical stability of arteries. *Journal of Biomechanical Engineering*, *131*(5), 051006. doi:10.1115/1.3078188

Rachev, A., & Greenwald, S. . (2003). Residual strains in conduit arteries. *Journal of Biomechanics, 36*(5), 661–670. doi:10.1016/S0021-9290(02)00444-X

Rastgar Agah, M., Laksari, K., & Darvish, K. (2012). Investigating the hyperelasticity of porcine aorta under sub-failure loading. In *2012 38th Annual Northeast Bioengineering Conference (NEBEC)* (pp. 432–433). IEEE. doi:10.1109/NEBC.2012.6206926

Rastgar Agah, M., Laksari, K., Darvish, K., & Rachev, A. (2012). Buckling of Porcine Aorta Under Static and Dynamic Loading. In *ASME 2012 Summer Bioengineering Conference* (pp. 287–288). Fajardo: American Society of Mechanical Engineers. Retrieved from http://proceedings.asmedigitalcollection.asme.org/data/Conferences/ASMEP/75484/287_1.pdf

Rezakhaniha, R., Agianniotis, A., Schrauwen, J. T. C., Griffa, A., Sage, D., Bouten, C. V. C., … Stergiopulos, N. (2012). Experimental investigation of collagen waviness and orientation in the arterial adventitia using confocal laser scanning microscopy. *Biomechanics and Modeling in Mechanobiology, 11*(3-4), 461–73. doi:10.1007/s10237-011-0325-z

Richens, D., Field, M., Neale, M., & Oakley, C. (2002). The mechanism of injury in blunt traumatic rupture of the aorta. *European Journal of Cardio-Thoracic Surgery : Official Journal of the European Association for Cardio-Thoracic Surgery, 21*(2), 288–93. Retrieved from http://www.ncbi.nlm.nih.gov/pubmed/11825737

Richens, D., & Kotidis, K. (2003). Rupture of the aorta following road traffic accidents in the United Kingdom 1992–1999. The results of the co-operative crash injury study. *European Journal of …, 23*, 143–148. doi:10.1016/S1

Rogers, C., Tseng, D. Y., Squire, J. C., & Edelman, E. R. (1999). Balloon-artery interactions during stent placement : A finite element analysis approach to pressure, compliance, and stent design as contributors to vascular injury. *Circulation Research, 84*(4), 378–383. doi:10.1161/01.RES.84.4.378

Sacks, M. (2000). Biaxial mechanical evaluation of planar biological materials. *Journal of Elasticity and the Physical Science of Solids*, 199–246. Retrieved from http://link.springer.com/article/10.1023/A:1010917028671

Sasongko, M. B., Wong, T. Y., Nguyen, T. T., Cheung, C. Y., Shaw, J. E., & Wang, J. J. (2011). Retinal vascular tortuosity in persons with diabetes and diabetic retinopathy. *Diabetologia, 54*(9), 2409–16. doi:10.1007/s00125-011-2200-y

Schulze-Bauer, C. A., Mörth, C., & Holzapfel, G. A. (2003). Passive biaxial mechanical response of aged human iliac arteries. *Journal of Biomechanical Engineering*, *125*(3), 395–406. doi:10.1115/1.1574331

Scott, R. A. (2001). Beams. In S. G. Braun (Ed.), *Encyclopedia of Vibration* (pp. 137–143). Elsevier. doi:10.1006/rwvb.2001.0128

Shah, C., Hardy, W., Mason, M., & Yang, K. (2006). Dynamic biaxial tissue properties of the human cadaver aorta, *50*(November), 217–246. Retrieved from http://papers.sae.org/2006-22-0010/

Shimizu, S., Tanaka, R., Kan, S., Suzuki, S., Kurata, A., & Fujii, K. (2005). Origins of the segmental arteries in the aorta: An anatomic study for selective catheterization with spinal arteriography. *American Journal of Neuroradiology*, *26*(April), 922–928.

Sokolis, D. P. (2007). Passive mechanical properties and structure of the aorta: segmental analysis. *Acta Physiologica*, *190*(4), 277–289. doi:10.1111/j.1748-1716.2006.01661.x

Sommer, G., Regitnig, P., Költringer, L., & Holzapfel, G. A. (2010). Biaxial mechanical properties of intact and layer-dissected human carotid arteries at physiological and supraphysiological loadings. *American Journal of Physiology. Heart and Circulatory Physiology*, *298*(3), H898–912. doi:10.1152/ajpheart.00378.2009

Stemper, B. D., Yoganandan, N., & Pintar, F. A. (2007). Mechanics of arterial subfailure with increasing loading rate. *Journal of Biomechanics*, *40*(8), 1806–1812. doi:10.1016/j.jbiomech.2006.07.005

Stergiopulos, N., Vulliémoz, S., Rachev, A., Meister, J. J., & Greenwald, S. E. (2001). Assessing the homogeneity of the elastic properties and composition of the pig aortic media. *Journal of Vascular Research*, *38*(3), 237–46. doi:51052

Symbas, P. N. (1977). Fundamentals of clinical cardiology Great vessels injury, *93*(4), 518–522.

Taylor, C. a., & Humphrey, J. D. (2009). Open problems in computational vascular biomechanics: Hemodynamics and arterial wall mechanics. *Computer Methods in Applied Mechanics and Engineering*, *198*(45-46), 3514–3523. doi:10.1016/j.cma.2009.02.004

Togay-Isikay, C., & Kim, J. (2005). Carotid artery tortuosity, kinking, coiling: stroke risk factor, marker, or curiosity? *Acta Neurologica Belgica*, 68–72. Retrieved from http://www.actaneurologica.be/acta/download/2005-2/03-Togay et al.pdf?origin=publication_detail

Trefethen, L. N., & David B. (1997). *Numerical linear algebra*. Philadelphia: SIAM: Society for Industrial and Applied Mathematics.

Viano, D. C. (2011). Chest impact experiments aimed at producing aortic rupture. *Clinical Anatomy (New York, N.Y.), 24*(3), 339–349. doi:10.1002/ca.21110

Vorp, D. A., Rajagopal, K. R., Smolinski, P. J., & Borovetz, H. S. (1995). Identification of elastic properties of homogeneous, orthotropic vascular segments in distension. *Journal of Biomechanics, 28*(5), 501–512. Retrieved from http://www.ncbi.nlm.nih.gov/pubmed/7775487

Wolf, Y. G., Tillich, M., Lee, W. a, Rubin, G. D., Fogarty, T. J., & Zarins, C. K. (2001). Impact of aortoiliac tortuosity on endovascular repair of abdominal aortic aneurysms: evaluation of 3D computer-based assessment. *Journal of Vascular Surgery, 34*(4), 594–9. doi:10.1067/mva.2001.118586

Wood, N. B., Zhao, S. Z., Zambanini, a, Jackson, M., Gedroyc, W., Thom, S. a, … Xu, X. Y. (2006). Curvature and tortuosity of the superficial femoral artery: a possible risk factor for peripheral arterial disease. *Journal of Applied Physiology (Bethesda, Md. : 1985), 101*(5), 1412–8. doi:10.1152/japplphysiol.00051.2006

Yoo, B.-S., Yoon, J., Ko, J.-Y., Kim, J.-Y., Lee, S.-H., Hwang, S.-O., & Choe, K.-H. (2005). Anatomical consideration of the radial artery for transradial coronary procedures: arterial diameter, branching anomaly and vessel tortuosity. *International Journal of Cardiology, 101*(3), 421–7. doi:10.1016/j.ijcard.2004.03.061

Zegers, E. S., Meursing, B. T. J., Zegers, E. B., & Oude Ophuis, a J. M. (2007). Coronary tortuosity: a long and winding road. *Netherlands Heart Journal : Monthly Journal of the Netherlands Society of Cardiology and the Netherlands Heart Foundation, 15*(5), 191–5. Retrieved from http://www.pubmedcentral.nih.gov/articlerender.fcgi?artid=1877966&tool=pmcentrez&rendertype=abstract

Zhang, J., Liu, Q., & Han, H. C. (2014). An *in vivo* rat model of artery buckling for studying wall remodeling. *Annals of Biomedical Engineering, 42*(8), 1658–67. doi:10.1007/s10439-014-1017-5

Zhang, W., Liu, Y., & Kassab, G. (2007). Viscoelasticity reduces the dynamic stresses and strains in the vessel wall: implications for vessel fatigue. *American Journal of Physiology-Heart and Circulatory Physiology, 46202,* 2355–2360. doi:10.1152/ajpheart.00423.2007.

# APPENDIX A. DERIVATION OF INFLATION-EXTENSION EQUATIONS

Aortic tissue is assumed to behave as an orthotropic hyperelastic material that can be modeled by a Fung-type strain energy density function(Fung et al, 1979) as shown below:

$$W = \frac{1}{2}c(e^{Q} - 1) \qquad Q = \boldsymbol{E}^{T}\boldsymbol{C}\boldsymbol{E} \tag{A.1}$$

in which

$$\boldsymbol{E} = \begin{bmatrix} E_r \\ E_\theta \\ E_z \end{bmatrix}, \qquad \boldsymbol{C} = \begin{bmatrix} c_1 & c_4 & c_5 \\ c_4 & c_2 & c_6 \\ c_5 & c_6 & c_3 \end{bmatrix} \tag{A.2}$$

In this equation $c_1$ to $c_6$ and $c$ are material parameters to be found by optimization. Assuming aortic segments to be incompressible thick wall cylinders, the principal strains are $E_r$, $E_\theta$ and $E_z$, representing the radial, circumferential and axial components of the Lagrangian strain tensor respectively. These components are related to stretch ratios by

$$E_i = \frac{1}{2}\left({\lambda_i}^2 - 1\right), \qquad i = r, \theta, z \tag{A.3}$$

Deformation of artery from an stress-free configuration $(R, \Theta, Z)$ to inflated configuration $(r, \theta, z)$ can be explained by stretch ratios in principal directions as

$$\lambda_r = \frac{\partial r}{\partial R}, \qquad \lambda_\theta = \frac{r}{R}\frac{\partial \theta}{\partial \Theta}, \qquad \lambda_z = \frac{z}{Z} \tag{A.4}$$

As a consequence of the incompressibility assumption stretch ratios are related by $\lambda_r\lambda_\theta\lambda_z = 1$ and radial stretch ratio can be calculated from two circumferential and longitudinal stretch ratios. Non-zero Components of Cauchy stress tensor then can be derived from strain energy density function as

$$T_r = {\lambda_r}^2 \frac{\partial W}{\partial r} + H, \qquad T_\theta = {\lambda_\theta}^2 \frac{\partial W}{\partial r} + H, \qquad T_z = {\lambda_z}^2 \frac{\partial W}{\partial z} + H \tag{A.5}$$

in which $H$ is the Lagrange multiplier that is necessary because of incompressibility assumption. For statically pressurized vessel and ignoring the effect of body forces the equation of equilibrium is derived:

$$div\,\boldsymbol{T} = 0 \tag{A.6}$$

where ***T*** is Cauchy stress tensor and *div* denotes the Eulerian (spatial) divergence operator. In the absence of shear components of stress in radial direction we have

$$\frac{dT_r}{dr} + \frac{T_r - T_\theta}{r} = 0 \tag{A.7}$$

By plugging in the components of Cauchy stress from Equation A.5 in Equation A.7 and integrating from internal radius $r_i$ to an arbitrary radius between inner and outer radii ($r_i \leq r \leq r_o$) and applying the boundary condition at internal radius ($T_r(r_i) = -p$) we have

$$T_r = \int_{r_i}^{r} \left( {\lambda_\theta}^2 \frac{\partial W}{\partial E_\theta} - {\lambda_r}^2 \frac{\partial W}{\partial E_r} \right) \frac{dr}{r} - p \tag{A.8}$$

where $p$ is the internal pressure of aorta. Assuming the outer surface of the aorta to be traction-free ($T_r(r_o) = 0$), we arrive at the following equation that explains the relation between internal pressure and deformation of aorta.

$$p = \int_{r_i}^{r_o} \left( {\lambda_\theta}^2 \frac{\partial W}{\partial E_\theta} - {\lambda_r}^2 \frac{\partial W}{\partial E_r} \right) \frac{dr}{r} \tag{A.9}$$

This equation allows calculation of the Lagrange multiplier as $H = T_r - {\lambda_r}^2 \frac{\partial W}{\partial r}$, which can be used to find the longitudinal component of Cauchy stress from Equation A.5

$$T_z = T_r + {\lambda_z}^2 \frac{\partial W}{\partial E_z} - {\lambda_r}^2 \frac{\partial W}{\partial E_r} \tag{A.10}$$

Static equilibrium in the longitudinal direction requires that the tensile force in the aortic wall at an arbitrary cross section of aorta be equal to the compressive force exerted by the fluid in the lumen:

$$F_Z = 2\pi \int_{r_i}^{r_o} T_z \, r \, dr = p \, A_{lum} \tag{A.12}$$

in which $A_{lum}$ is the lumen area. The material parameters can be calculated by simultaneous optimization of Equations A.9 and A.12 to the experimental measurements.

# APPENDIX B. DERIVATION OF UNIAXIAL EXTENSION EQUATIONS

Assuming an orthotropic material (with 3 axes of isotropy $\boldsymbol{e}_1, \boldsymbol{e}_2, \boldsymbol{e}_3$) under extension along one of its principal directions, the deformation gradient can be written as

$$\boldsymbol{F} = \begin{bmatrix} \lambda_1 & 0 & 0 \\ 0 & \lambda_2 & 0 \\ 0 & 0 & \lambda_3 \end{bmatrix} \tag{B.1}$$

in which $\lambda_i$'s are the principal stretch ratios. Taking the material to be incompressible, the determinant of deformation gradient should be one, i.e. $J = \det(F) = 1$. Lagrangian strain can be calculated by

$$E = \frac{1}{2}(\boldsymbol{F}^T\boldsymbol{F} - \boldsymbol{I}) \rightarrow\ E_i = \frac{1}{2}\left({\lambda_i}^2 - 1\right), \qquad i = r, \theta, z \tag{B.2}$$

Knowing the strain energy density function of the tissue in the form of $W(E)$ and enforcing the incompressibity condition through a Lagrange multiplier $H$ we have

$$W^* = W(\boldsymbol{E}) - H(J - 1) \tag{B.3}$$

The second Piola-Kirchhoff stress can be calculated as $\boldsymbol{S} = \frac{\partial W}{\partial \boldsymbol{E}}$ with nonzero components of

$$S_i = \frac{\partial W}{\partial E_i} - H\frac{\partial J}{\partial E_i}, \qquad i = 1,2,3 \tag{B.4}$$

The derivative of $J$ can be calculated by chain rule and we have

$$\boldsymbol{S} = \begin{bmatrix} \frac{\partial W}{\partial E_1} - H\frac{\lambda_2\lambda_3}{\lambda_1} & 0 & 0 \\ 0 & \frac{\partial W}{\partial E_2} - H\frac{\lambda_1\lambda_3}{\lambda_2} & 0 \\ 0 & 0 & \frac{\partial W}{\partial E_3} - H\frac{\lambda_1\lambda_2}{\lambda_3} \end{bmatrix} \tag{B.5}$$

The Cauchy stress can be derived from second Piola-Kirchhoff stress through $\boldsymbol{T} = \frac{1}{J}\boldsymbol{FSF}^T$ with the following nonzero components

$$T_i = {\lambda_i}^2 \frac{\partial W}{\partial E_i} - H, \qquad i = 1,2,3 \tag{B.6}$$

Since the state of strain in the problem is not a function of position, equation of equilibrium in the absence of body forces reveals that $H$ is also not a function of position and depends only on the state of strain. Consequently, the state of stress is also independent of position.

Without loss of generality the extension can be assumed to be along the $\boldsymbol{e}_3$ direction. Since the surface of the sample in $e_1$ and $e_2$ directions are traction free it can be concluded that the components of Cauchy stress in these directions are zero everywhere and

$$T_1 = T_2 = 0 \rightarrow\ H = {\lambda_1}^2 \frac{\partial W}{\partial E_1} = {\lambda_2}^2 \frac{\partial W}{\partial E_2} \tag{B.7}$$

The above equation gives a relation between the three components of strain and together with the incompressibility equation forms a system of two equations with two unknowns $(\lambda_1, \lambda_2)$ that can be solved numerically for a known $\lambda_3$, i.e. the state of deformation is determined. Moreover by plugging the Lagrange multiplier form Equation B.7 into the third component of Equation B.6, stress in the $\boldsymbol{e}_3$ direction can be calculated.

# APPENDIX C. UNIAXIAL EXPERIMENTAL DATA

Table C.1 – Sample specifications and test parameters

| Sample ID | Test Dir. | Test Speed (m/s) | Specimen # | Sample Thickness (mm) | Gauge length Width | Data Acquisition Rate | Camera fps |
|---|---|---|---|---|---|---|---|
| 001mps_S41C2 | C | 0.001 | 41 | 2.4 | 5.2 | 500 | 100 |
| 001mps_S41L2 | L | 0.001 | 41 | 3.1 | 5.7 | 500 | 100 |
| 001mps_S42C1 | C | 0.001 | 42 | 2.5 | 5.7 | 500 | 100 |
| 001mps_S42L1 | L | 0.001 | 42 | 2.6 | 5.7 | 500 | 100 |
| 001mps_S44C3 | C | 0.001 | 44 | 2.1 | 5.6 | 500 | 100 |
| 001mps_S44L3 | L | 0.001 | 44 | 2.3 | 5.7 | 500 | 100 |
| 001mps_S45C1 | C | 0.001 | 45 | 2.6 | 5.4 | 500 | 100 |
| 001mps_S45L3 | L | 0.001 | 45 | 2.2 | 5.9 | 500 | 100 |
| 01mps_S16L3 | L | 0.01 | 16 | 2.6 | 5.3 | 2000 | 1000 |
| 01mps_S17L1 | L | 0.01 | 17 | 2.8 | 5.2 | 2000 | 1000 |
| 01mps_S24C2 | C | 0.01 | 24 | 1.9 | 5.1 | 10000 | 1000 |
| 01mps_S24L2 | L | 0.01 | 24 | 2.4 | 5.2 | 10000 | 1000 |
| 01mps_S28L3 | L | 0.01 | 28 | 1.8 | 5.6 | 10000 | 1000 |
| 01mps_S29C3 | C | 0.01 | 29 | 2.0 | 5.3 | 10000 | 1000 |
| 01mps_S29L3 | L | 0.01 | 29 | 1.9 | 5.7 | 10000 | 1000 |
| 01mps_S30C1 | C | 0.01 | 30 | 2.3 | 5.8 | 10000 | 1000 |
| 01mps_S30L1 | L | 0.01 | 30 | 2.5 | 5.6 | 10000 | 1000 |
| 01mps_S41C1 | C | 0.01 | 41 | 2.3 | 5.1 | 5000 | 1000 |
| 01mps_S41L1 | L | 0.01 | 41 | 2.8 | 5.4 | 5000 | 1000 |
| 01mps_S42C2 | C | 0.01 | 42 | 2.8 | 5.4 | 5000 | 1000 |
| 01mps_S42L3 | L | 0.01 | 42 | 2.5 | 5.7 | 5000 | 1000 |
| 01mps_S43C3 | C | 0.01 | 43 | 2.3 | 5.3 | 5000 | 1000 |
| 01mps_S43L3 | L | 0.01 | 43 | 2.3 | 5.6 | 5000 | 1000 |
| 01mps_S44C1 | C | 0.01 | 44 | 2.1 | 5.6 | 5000 | 1000 |
| 01mps_S44L1 | L | 0.01 | 44 | 2.3 | 5.9 | 5000 | 1000 |
| 01mps_S45C2 | C | 0.01 | 45 | 2.2 | 5.3 | 5000 | 1000 |
| 01mps_S45L2 | L | 0.01 | 45 | 2.7 | 6.1 | 5000 | 1000 |
| 1mps_S14C2 | C | 1 | 14 | 2.3 | 5.2 | 20000 | 10000 |
| 1mps_S14L1 | L | 1 | 14 | 3.0 | 5.1 | 20000 | 10000 |
| 1mps_S22C2 | C | 1 | 22 | 1.9 | 5.3 | 20000 | 13029 |

| | | | | | | | |
|---|---|---|---|---|---|---|---|
| 1mps_S22L2 | L | 1 | 22 | 2.1 | 5.7 | 20000 | 13029 |
| 1mps_S26C2 | C | 1 | 26 | 2.2 | 5.3 | 130290 | 13029 |
| 1mps_S28C1 | C | 1 | 28 | 2.0 | 5.6 | 130290 | 13029 |
| 1mps_S28L1 | L | 1 | 28 | 2.0 | 5.5 | 130290 | 13029 |
| 1mps_S36C2 | C | 1 | 36 | 2.1 | 5.4 | 25000 | 5000 |
| 1mps_S37C1 | C | 1 | 37 | 2.4 | 5.2 | 25000 | 5000 |
| 1mps_S37L2 | L | 1 | 37 | 2.6 | 6.0 | 25000 | 5000 |
| 1mps_S38C1 | C | 1 | 38 | 2.6 | 5.6 | 25000 | 5000 |
| 1mps_S38L1 | L | 1 | 38 | 2.4 | 5.8 | 25000 | 5000 |
| 1mps_S39C2 | C | 1 | 39 | 2.7 | 5.4 | 25000 | 5000 |
| 1mps_S39L2 | L | 1 | 39 | 3.3 | 6.1 | 25000 | 5000 |
| 1mps_S40C1 | C | 1 | 40 | 2.8 | 4.9 | 25000 | 5000 |
| 10mps_S36C4 | C | 10 | 36 | 2.1 | 5.4 | 65145 | 13029 |
| 10mps_S36L1 | L | 10 | 36 | 2.4 | 5.6 | 65145 | 13029 |
| 10mps_S37C2 | C | 10 | 37 | 2.1 | 5.4 | 65145 | 13029 |
| 10mps_S37L3 | L | 10 | 37 | 2.4 | 5.4 | 65145 | 13029 |
| 10mps_S38C3 | C | 10 | 38 | 2.3 | 5.3 | 65145 | 13029 |
| 10mps_S38L3 | L | 10 | 38 | 2.6 | 6.0 | 65145 | 13029 |
| 10mps_S39C1 | C | 10 | 39 | 2.8 | 5.8 | 65145 | 13029 |
| 10mps_S39L1 | L | 10 | 39 | 2.8 | 5.9 | 65145 | 13029 |
| 10mps_S40C2 | C | 10 | 40 | 2.8 | 5.7 | 65145 | 13029 |
| 10mps_S40L3 | L | 10 | 40 | 2.6 | 6.1 | 65145 | 13029 |

**Cauchy stress versus stretch ratio curves obtained for all samples.**

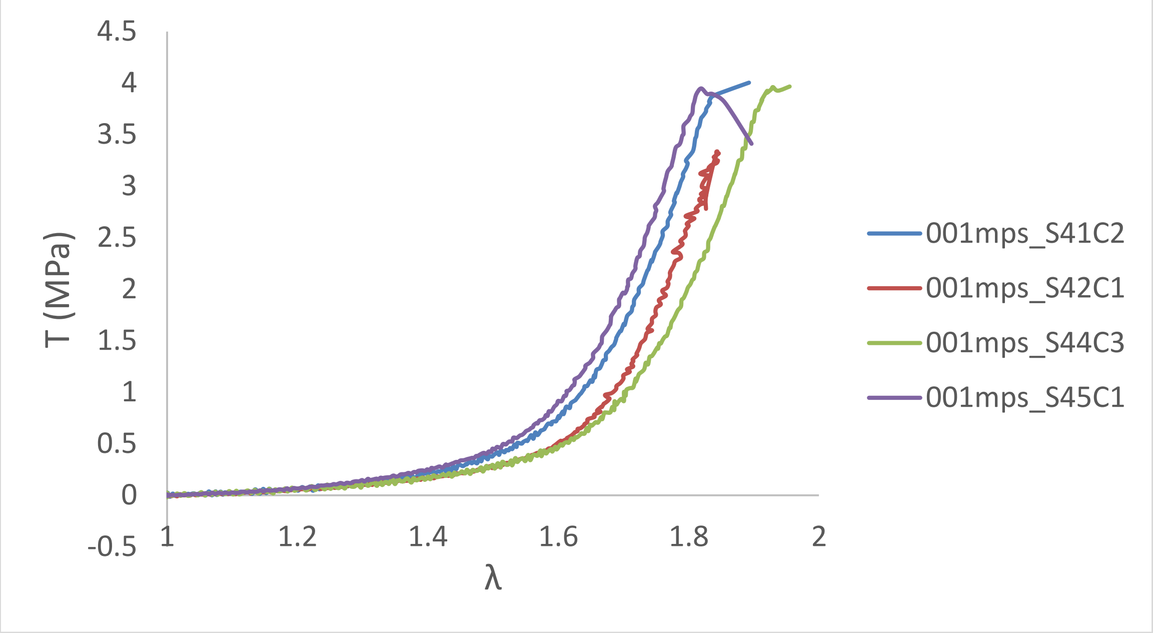

Figure 26 - Cauchy stress vs stretch ratio in C direction at Rate 1

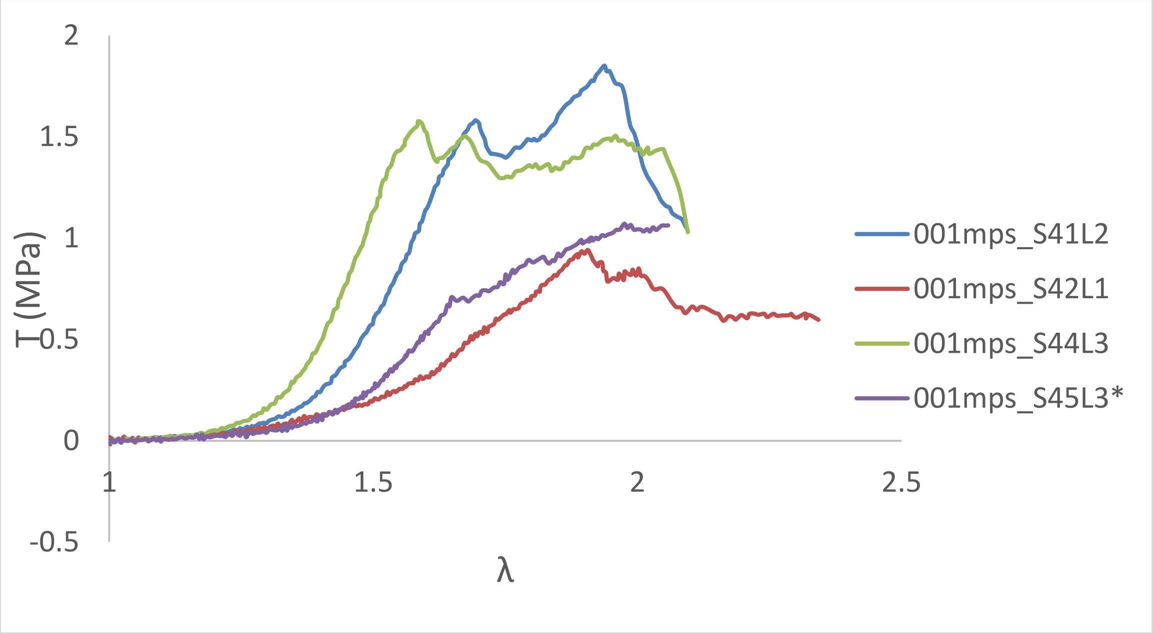

Figure 27 - Cauchy stress vs stretch ratio in L direction at Rate 1

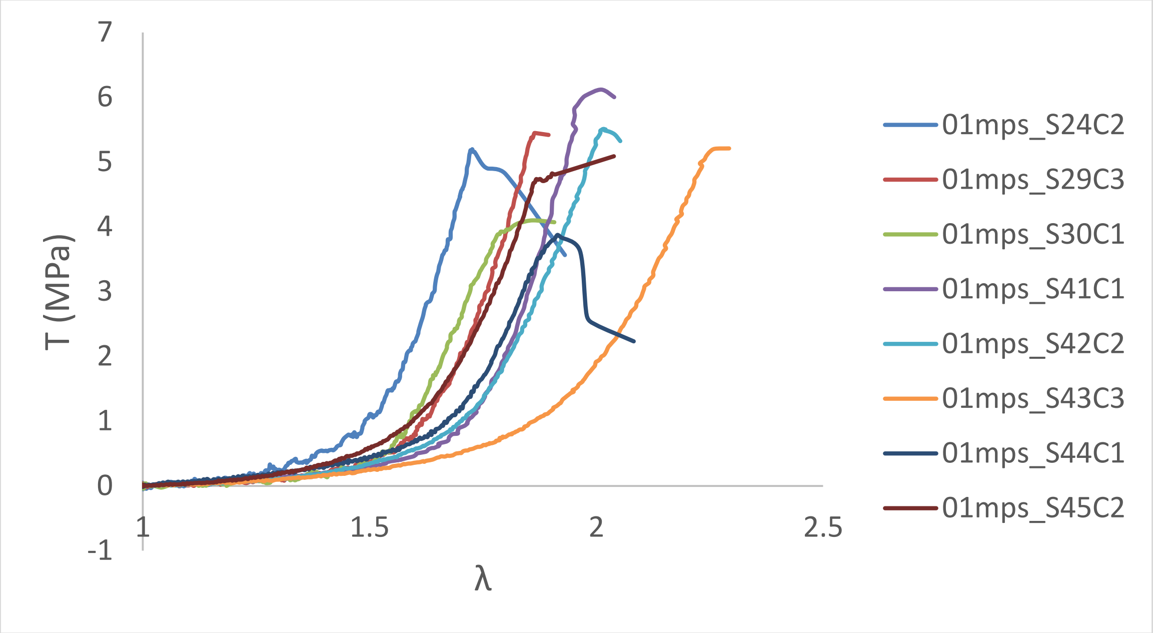

Figure 28 - Cauchy stress vs stretch ratio in C direction at Rate 2

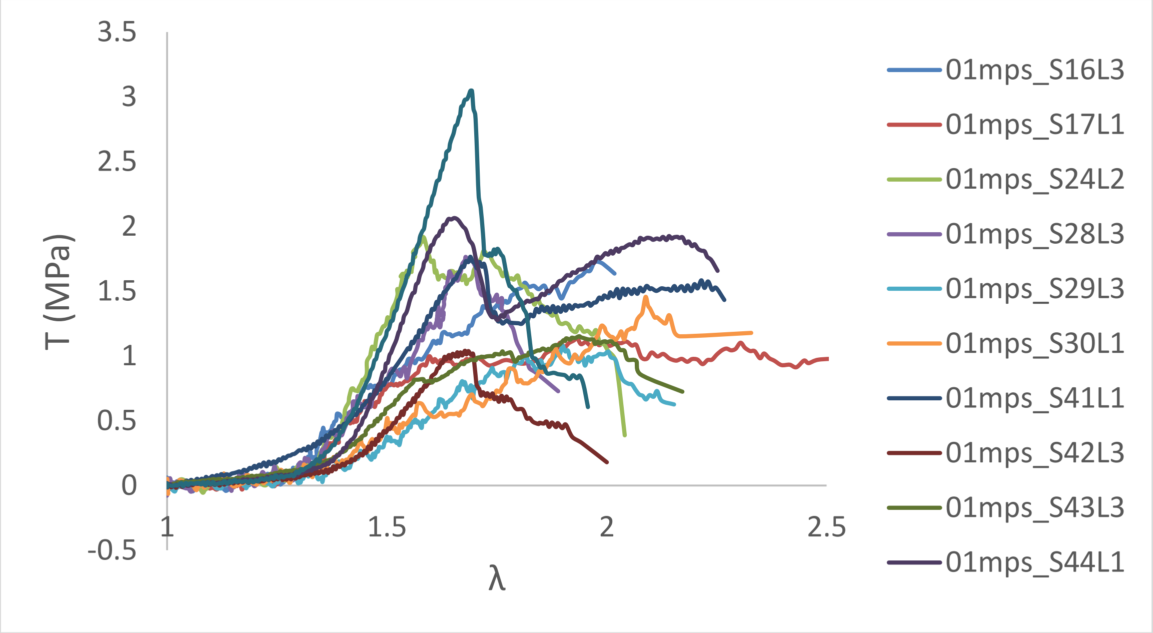

Figure 29 - Cauchy stress vs stretch ratio in L direction at Rate 2

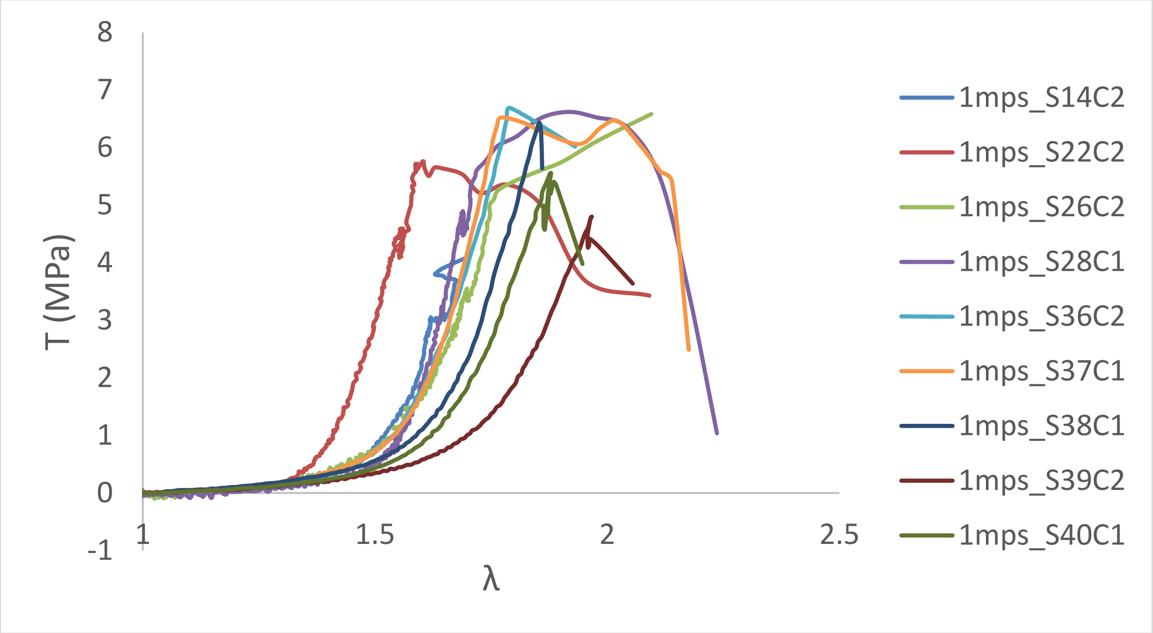

Figure 30 - Cauchy stress vs stretch ratio in C direction at Rate 3

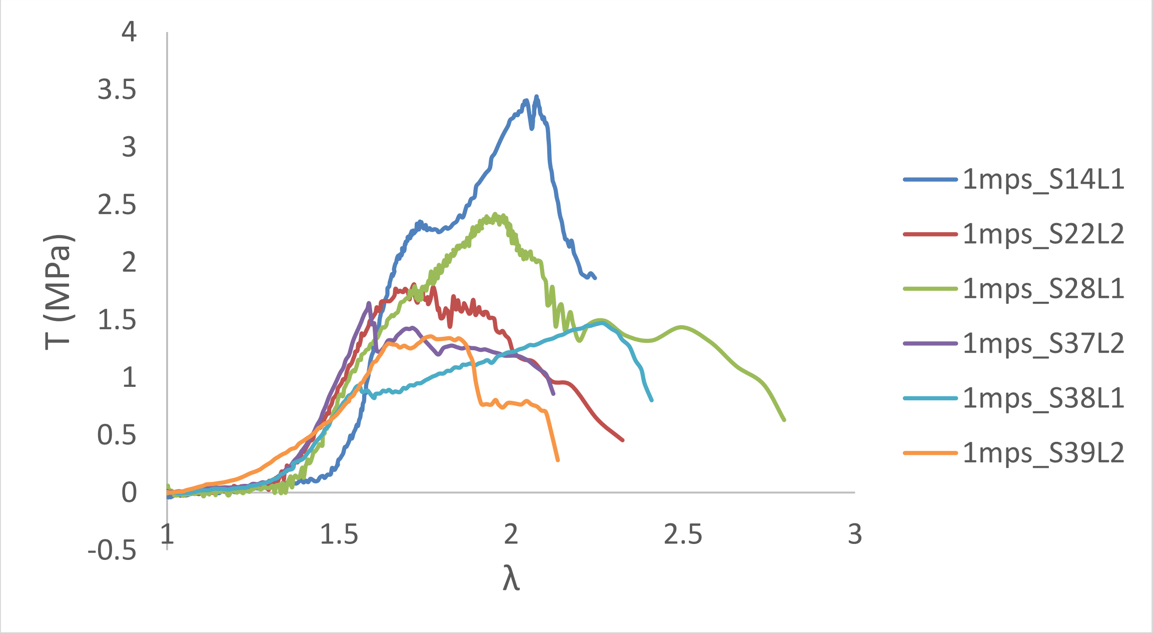

Figure 31 - Cauchy stress vs stretch ratio in L direction at Rate 3

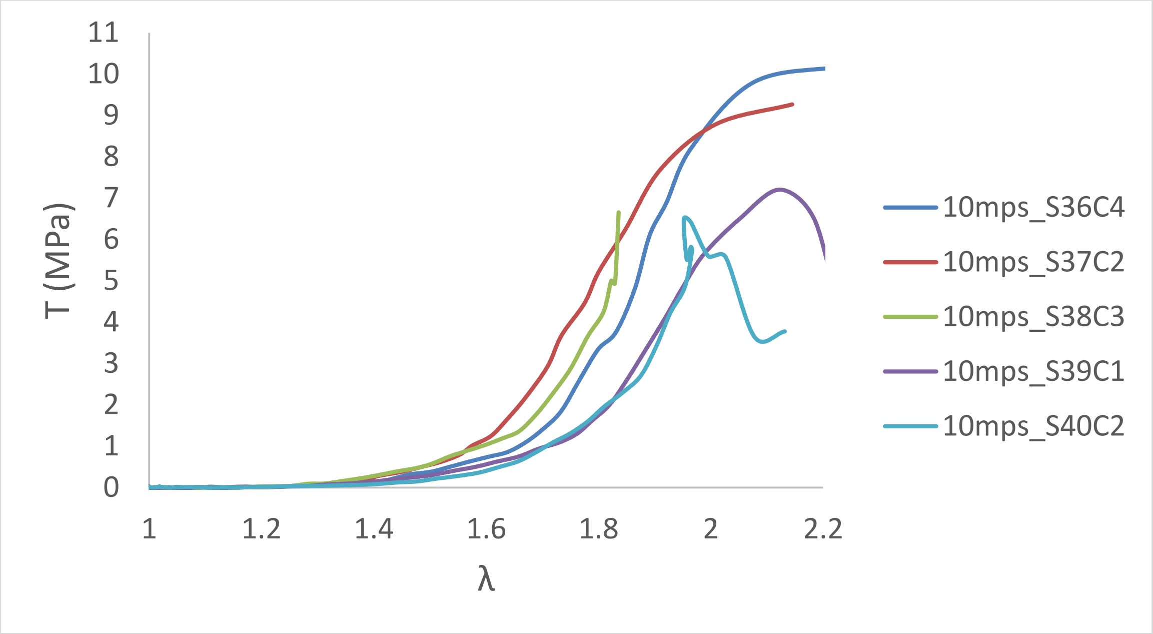

Figure 32 - Cauchy stress vs stretch ratio in C direction at Rate 4

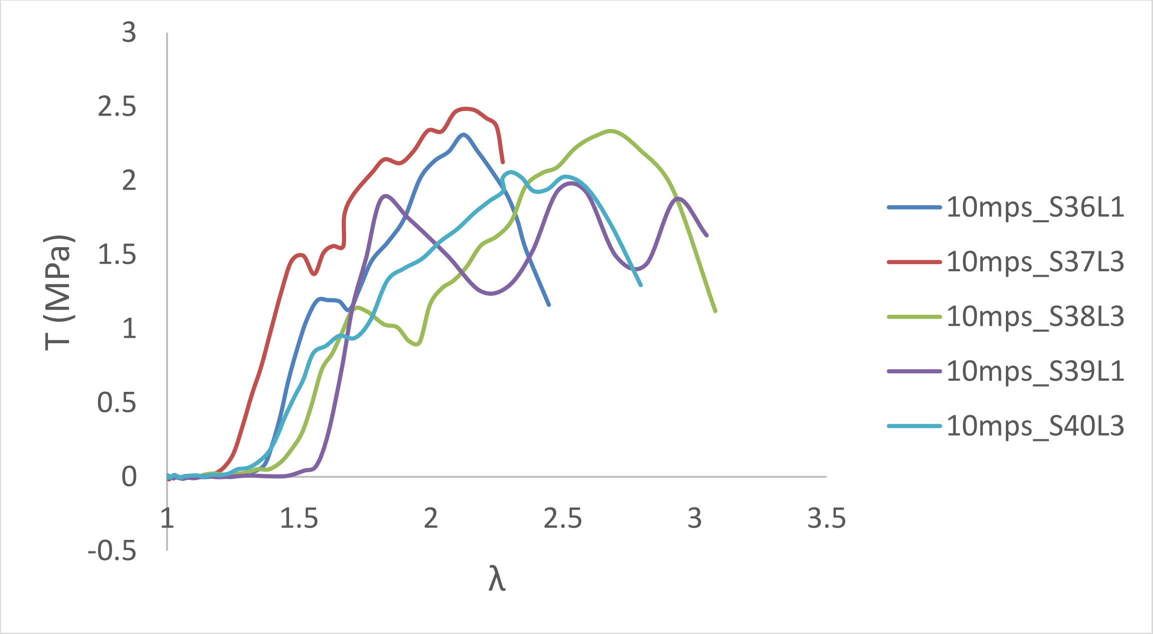

Figure 33 - Cauchy stress vs stretch ratio in L direction at Rate 4